

**SPIE.** FIELD  
GUIDE

Field Guide to

# **Infrared Systems, Detectors, and FPAs**

Third Edition

***Arnold Daniels***

**SPIE Terms of Use:** This SPIE eBook is DRM-free for your convenience. You may install this eBook on any device you own, but not post it publicly or transmit it to others. SPIE eBooks are for personal use only. For details, see the SPIE [Terms of Use](#). To order a print version, [visit SPIE](#).

**SPIE.**

Field Guide to  
**Infrared  
Systems,  
Detectors,  
and FPAs**  
Third Edition

Arnold Daniels

SPIE Field Guides  
Volume FG40

John E. Greivenkamp, Series Editor

**SPIE PRESS**  
Bellingham, Washington USA

## Library of Congress Cataloging-in-Publication Data

Names: Daniels, Arnold, author.

Title: Field guide to infrared systems, detectors, and FPAs / Arnold Daniels.

Other titles: Infrared systems, detectors, and FPAs | SPIE field guides.

Description: Third edition. | Bellingham, Washington, USA : SPIE Press, [2018] | Series: The field guide series | Includes bibliographical references and index.

Identifiers: LCCN 2017060172 | ISBN 9781510618640 (spiral ; alk. paper) | ISBN 1510618643 (spiral ; alk. paper) | ISBN 9781510618657 (PDF) | ISBN 1510618651 (PDF) | ISBN 9781510618664 (ePub) | ISBN 151061866X (ePub) | ISBN 9781510618671 (Kindle/Mobi) | ISBN 1510618678 (Kindle/Mobi)

Subjects: LCSH: Infrared technology--Handbooks, manuals, etc. | Optical detectors--Handbooks, manuals, etc. | Focal planes--Handbooks, manuals, etc.

Classification: LCC TA1570 .D36 2018 | DDC 621.36/2--dc23

LC record available at <https://lcn.loc.gov/2017060172>

Published by

SPIE

P.O. Box 10

Bellingham, Washington 98227-0010 USA

Phone: 360.676.3290

Fax: 360.647.1445

Email: [Books@spie.org](mailto:Books@spie.org)

Web: [www.spie.org](http://www.spie.org)

Copyright © 2018 Society of Photo-Optical Instrumentation Engineers (SPIE)

All rights reserved. No part of this publication may be reproduced or distributed in any form or by any means without written permission of the publisher.

The content of this book reflects the thought of the author. Every effort has been made to publish reliable and accurate information herein, but the publisher is not responsible for the validity of the information or for any outcomes resulting from reliance thereon.

Printed in the United States of America.

First printing.

For updates to this book, visit <http://spie.org> and type "FG40" in the search field.

# **SPIE.**



## Introduction to the Series

---

Welcome to the *SPIE Field Guides*—a series of publications written directly for the practicing engineer or scientist. Many textbooks and professional reference books cover optical principles and techniques in depth. The aim of the *SPIE Field Guides* is to distill this information, providing readers with a handy desk or briefcase reference that provides basic, essential information about optical principles, techniques, or phenomena, including definitions and descriptions, key equations, illustrations, application examples, design considerations, and additional resources. A significant effort will be made to provide a consistent notation and style between volumes in the series.

Each *SPIE Field Guide* addresses a major field of optical science and technology. The concept of these *Field Guides* is a format-intensive presentation based on figures and equations supplemented by concise explanations. In most cases, this modular approach places a single topic on a page, and provides full coverage of that topic on that page. Highlights, insights, and rules of thumb are displayed in sidebars to the main text. The appendices at the end of each *Field Guide* provide additional information such as related material outside the main scope of the volume, key mathematical relationships, and alternative methods. While complete in their coverage, the concise presentation may not be appropriate for those new to the field.

The *SPIE Field Guides* are intended to be living documents. The modular page-based presentation format allows them to be updated and expanded. We are interested in your suggestions for new *Field Guide* topics as well as what material should be added to an individual volume to make these *Field Guides* more useful to you. Please contact us at [fieldguides@SPIE.org](mailto:fieldguides@SPIE.org).

John E. Greivenkamp, *Series Editor*  
College of Optical Sciences  
The University of Arizona

## The Field Guide Series

---

Keep information at your fingertips with the *SPIE Field Guides*:

- Adaptive Optics*, Second Edition, Robert K. Tyson and Benjamin W. Frazier
- Astronomical Instrumentation*, Christoph U. Keller, Ramon Navarro, and Bernhard R. Brandl
- Atmospheric Optics*, Second Edition, Larry C. Andrews
- Binoculars and Scopes*, Paul R. Yoder, Jr. and Daniel Vukobratovich
- Crystal Growth*, Ashok K. Batra and Mohan D. Aggarwal
- Diffraction Optics*, Yakov G. Soskind
- Digital Micro-Optics*, Bernard Kress
- Displacement Measuring Interferometry*, Jonathan D. Ellis
- Fiber Optic Sensors*, William Spillman, Jr. and Eric Udd
- Geometrical Optics*, John E. Greivenkamp
- Holography*, Pierre-Alexandre Blanche
- Illumination*, Angelo Arecchi, Tahar Messadi, and R. John Koschel
- Image Processing*, Khan M. Iftikharuddin and Abdul Awwal
- Infrared Optics, Materials, and Radiometry*, Arnold Daniels
- Interferometric Optical Testing*, Eric P. Goodwin and James C. Wyant
- Laser Pulse Generation*, Rüdiger Paschotta
- Lasers*, Rüdiger Paschotta
- Lens Design*, Julie Bentley and Craig Olson
- Lidar*, Paul McManamon
- Linear Systems in Optics*, J. Scott Tyo and Andrey S. Alenin
- Microscopy*, Tomasz S. Tkaczyk
- Molded Optics*, Alan Symmons and Michael Schaub
- Nonlinear Optics*, Peter E. Powers
- Optical Fabrication*, Ray Williamson
- Optical Fiber Technology*, Rüdiger Paschotta
- Optical Lithography*, Chris A. Mack
- Optical Thin Films*, Ronald R. Willey
- Optomechanical Design and Analysis*, Katie Schwertz and James H. Burge
- Physical Optics*, Daniel G. Smith
- Polarization*, Edward Collett
- Probability, Random Processes, and Random Data Analysis*, Larry C. Andrews and Ronald L. Phillips
- Radiometry*, Barbara G. Grant
- Special Functions for Engineers*, Larry C. Andrews
- Spectroscopy*, David W. Ball
- Terahertz Sources, Detectors, and Optics*, Cr  idhe M. O'Sullivan and J. Anthony Murphy
- Visual and Ophthalmic Optics*, Jim Schwiegerling

## Field Guide to Infrared Systems, Detectors, and FPAs, Third Edition

---

The amount of new material that was added to the second edition of the *Field Guide to Infrared Systems, Detectors, and FPAs* (2010) was rather extensive. As a result, this third edition is accompanied by a “companion” publication, the *Field Guide to Infrared Optics, Materials, and Radiometry*.

These Field Guides cover a broad range of technical topics necessary to understand the principles of modern infrared technology. They combine numerous engineering disciplines that are essential for the development of infrared systems. The mathematical equations and physical concepts in these Field Guides are in sequence. Therefore, although these publications are sold separately, it is highly recommended that readers acquire the two books as a set.

This third edition of the *Field Guide to Infrared Systems, Detectors, and FPAs*, is devoted to fundamental background issues for optical detection processes. It compares the characteristics of cooled and uncooled detectors with an emphasis on spectral and blackbody responsivity, and detectivity, as well as the noise mechanisms related to optical detection. This edition introduces the concepts of barrier infrared detector technologies and encompasses the capabilities and challenges of third-generation infrared focal plane arrays as well as the advantages of using dual-band technology.

With this acquired background, the last chapter considers the systems design aspects of infrared imagers. Figures of merit such as MTF, NETD, and MRTD of staring arrays are examined for the performance metrics of thermal sensitivity and spatial resolution of thermal imaging systems. The parameter  $\lambda(F/\#)/d$ , motion MTF, and atmospheric MTF are included in this third edition. It also includes an overview of the targeting task performance (TTP) metric.

I would like to acknowledge and express my gratitude to my professor and mentor Dr. Glenn Boreman for his

## **Field Guide to Infrared Systems, Detectors, and FPAs, Third Edition**

---

guidance, experience, and friendship. The knowledge that he passed on to me during my graduate studies at CREOL ultimately contributed to the creation of this book.

I extend my sincere appreciation to Dr. Mel Friedman, NVESD, who took on the onerous task of improving and clarifying the TTP metric concepts and its contents. I would also like to thank Mr. Thomas Haberfelde for his efforts in reviewing the drafts of the manuscripts as well as Alexander Daniels and Dara Burrows for their skillful editing assistance.

Above all, I voice a special note of gratitude to my kids Becky and Alex, and my wife Rosa for their love and support.

Lastly, I would particularly like to thank you, the reader, for selecting these books and taking the time to explore the topics related to this motivating and exciting field. I trust that the contents of these Field Guides will prove interesting and useful to engineers and scientists working in one of the various infrared fields.

These Field Guides are dedicated to the memory of my father and brothers.

**Arnold Daniels**  
September 2018

## Table of Contents

|  |           |
|--|-----------|
| <b>Glossary of Symbols</b>   | <b>x</b>  |
| <b>Introduction</b>  | <b>1</b>  |
| History of Infrared Detectors and Systems                                  | 1         |
| Detector IRFPA Roadmap   | 2         |
| <b>Performance Parameters for Optical Detectors</b>                        | <b>3</b>  |
| Infrared Detectors   | 3         |
| Primary Sources of Detector Noise  | 4         |
| Noise Power Spectral Density   | 5         |
| White Noise  | 6         |
| Noise-Equivalent Bandwidth ( $NE\Delta f$ )                                | 7         |
| Shot Noise   | 9         |
| Signal-to-Noise Ratio: Detector and BLIP Limits                            | 10        |
| Generation–Recombination Noise   | 11        |
| Johnson Noise  | 12        |
| $1/f$ Noise and Temperature Noise  | 13        |
| Detector Responsivity  | 14        |
| Spectral Responsivity  | 16        |
| Blackbody Responsivity   | 17        |
| Noise-Equivalent Power   | 19        |
| Specific or Normalized Detectivity   | 20        |
| Photovoltaic Detectors or Photodiodes                                      | 21        |
| Sources of Noise in PV Detectors   | 22        |
| Expressions for $D_{PV,BLIP}^*$ , $D_{PV,BLIP}^{**}$ , and $D_{PV,JOLI}^*$ | 23        |
| Photoconductive Detectors  | 24        |
| Sources of Noise in PC Detectors   | 25        |
| <b>Infrared Semiconductor and Detector Technologies</b>                    | <b>26</b> |
| Infrared Semiconductor Material Groups                                     | 26        |
| Third-Generation Infrared Imagers: Requirements                            | 27        |
| Third-Generation Infrared Imagers: Challenges                              | 28        |
| Indium Antimonite (InSb) Photodiodes                                       | 30        |
| InSb Dual-Band Integrated Dewar Cooler Assembly                            | 31        |
| Concept of Barrier Infrared Photodetectors                                 | 32        |
| MWIR nBn Photodetector   | 33        |

## Table of Contents

|  |           |
|--|-----------|
| Mercury Cadmium Telluride (HgCdTe)             | 35        |
| Photodetectors                                 |           |
| Control of the Alloy Composition               | 36        |
| HgCdTe Photodiodes and FPAs                    | 37        |
| Double-Layer Heterostructure Junction          | 38        |
| Photodiodes                                    |           |
| Dual-Band HgCdTe FPAs                          | 39        |
| High-Density Vertically Integrated Photodiodes | 40        |
| Uncooled HgCdTe Photodiodes                    | 42        |
| Quantum Well Infrared Photodetectors           | 44        |
| Types of QWIPs                                 | 47        |
| Superlattices                                  | 49        |
| Multispectral QWIPs                            | 50        |
| Light Couplers                                 | 52        |
| Type II Strained-Layer Superlattices           | 55        |
| Dual-Band IRFPA Technology: Advantages         | 57        |
| 3D Read-Out Integrated Circuits                | 58        |
| Adaptive FPAs                                  | 59        |
| Pyroelectric Detectors                         | 61        |
| Pyroelectric Detectors: Mathematical Approach  | 63        |
| Microbolometers                                | 66        |
| Microbolometers: Mathematical Approach         | 69        |
| Infrared Dynamic Scene Simulators              | 72        |
| Thermoelectric Detectors                       | 73        |
| Carbon Nanotubes for Infrared Applications     | 74        |
| <b>Infrared Systems</b>                        | <b>75</b> |
| Raster Scan Format: Single Detector            | 75        |
| Multiple-Detector Scan Formats: Serial Scene   | 77        |
| Dissection                                     |           |
| Multiple-Detector Scan Formats: Parallel Scene | 78        |
| Dissection                                     |           |
| Staring Systems                                | 79        |
| Search Systems and the Range Equation          | 80        |
| Noise-Equivalent Irradiance                    | 83        |
| Performance Specification: Thermal Imaging     | 84        |
| Systems  |           |
| Modulation Transfer Function (MTF)             | 85        |
| Optics MTF: Calculations                       | 89        |

## Table of Contents

|  |            |
|--|------------|
| Detector MTF: Calculations   | 91         |
| Parameter $\lambda(F/\#)/d$  | 92         |
| Motion MTF: Calculations   | 93         |
| Atmospheric MTF: Calculations  | 94         |
| MTF Measurement Setup and Sampling Effects   | 95         |
| MTF Measurement Techniques: Point Spread<br>Function and Line Spread Function      | 96         |
| MTF Measurement Techniques: Edge Spread<br>Function and Contrast Transfer Function | 97         |
| MTF Measurement Techniques: Noise-like<br>Targets                                  | 99         |
| MTF Measurement Techniques: Interferometry   | 101        |
| Noise-Equivalent Temperature Difference (NETD)                                     | 102        |
| NETD of Microbolometers  | 103        |
| NETD Measurement Technique   | 104        |
| Minimum Resolvable Temperature Difference<br>(MRTD)                                | 105        |
| MRTD: Calculation  | 106        |
| MRTD Measurement Technique   | 107        |
| MRTD Measurement: Automatic Test   | 108        |
| Johnson Metric Methodology   | 109        |
| Johnson Criteria Flaws   | 111        |
| Targeting Task Performance (TTP) Metric<br>Methodology                             | 112        |
| Human Vision: Distribution of Retinal<br>Photoreceptors                            | 113        |
| Human Vision: Response and Sensitivity   | 114        |
| Contrast Threshold Function (CTF)  | 115        |
| Target Acquisition Performance   | 120        |
| Probability of Targeting Task Performance  | 124        |
| N50-to-V50 Conversion (Example)  | 126        |
| Acquisition Level Definitions  | 127        |
| TTP Summary  | 128        |
| <b>Equation Summary</b>  | <b>129</b> |
| <b>Bibliography</b>  | <b>139</b> |
| <b>Index</b>   | <b>147</b> |

## Glossary of Symbols

---

|                           |   |
|---------------------------|---|
| $\alpha$                  | Size of airborne particles                                    |
| $A$                       | Area  |
| $A_d$                     | Detector area   |
| $A_{\text{obj}}$          | Area of an object   |
| $A_{\text{opt}}$          | Area of an optical component                                  |
| $A_s$                     | Area of a source  |
| $B$                       | 3-db bandwidth  |
| B-B                       | Bound-to-bound  |
| B-C                       | Bound-to-continuum  |
| B-QB                      | Bound-to-quasi-bound  |
| BLIP                      | Background-limited infrared photodetector                     |
| $c$                       | Speed of light in vacuum                                      |
| $C_d$                     | Detector capacitance  |
| $C_{\text{th}}$           | Thermal capacitance   |
| $C_n^2$                   | Refractive index structure constant                           |
| CQWIP                     | Corrugated quantum-well infrared photodetector                |
| CTE                       | Coefficient of thermal expansion                              |
| CTF                       | Contrast transfer function                                    |
| $\text{CTF}_{\text{eye}}$ | Contrast threshold function of the eye                        |
| $\text{CTF}_n$            | Contrast threshold function in the presence of external noise |
| $\text{CTF}_{\text{sys}}$ | Contrast threshold function of a system                       |
| $d$                       | Detector size   |
| $d_{\text{diff}}$         | Diameter of a diffraction-limited spot                        |
| $d_h$                     | Detector size in the horizontal direction                     |
| $d_v$                     | Detector size in the vertical direction                       |
| $D$                       | Electrical displacement                                       |
| $D^*$                     | Normalized detectivity of a detector                          |
| $D_{\text{BF}}^*$         | Background fluctuation D-star                                 |
| $D_{\text{BLIP}}^*$       | D-star under BLIP conditions                                  |
| $D_{\text{TF}}^*$         | Temperature fluctuation D-star                                |
| $D^{**}$                  | Angle-normalized detectivity                                  |
| $D_{\text{in}}$           | Input diameter  |
| $D_{\text{lens}}$         | Lens diameter   |
| $D_{\text{opt}}$          | Optics diameter   |
| $D_{\text{out}}$          | Output diameter   |
| e                         | Energy-based unit subscript                                   |



## Glossary of Symbols

---

|                            |  |
|----------------------------|--|
| $E_{\text{bkg}}$           | Background irradiance                            |
| $E_{\text{source}}$        | Source irradiance                                |
| ESF                        | Edge spread function                             |
| $\mathcal{E}$              | Energy of a photon                               |
| $\mathcal{E}_{\text{gap}}$ | Energy gap of a semiconductor material           |
| $f$                        | Focal length                                     |
| $f_0$                      | Center frequency of an electrical filter         |
| $f_{\text{eff}}$           | Effective focal length                           |
| $f(x,y)$                   | Object function                                  |
| $F$                        | Finesse  |
| $F(\xi,\eta)$              | Object spectrum                                  |
| FOR                        | Field of regard                                  |
| FOV                        | Full-angle field of view                         |
| FPA                        | Focal plane array                                |
| $F/\#$                     | F-number   |
| $g(x,y)$                   | Image function                                   |
| $G$                        | Gain of a photoconductive detector               |
| $G(\xi,\eta)$              | Image spectrum                                   |
| $h$                        | Planck's constant                                |
| $h_{\text{img}}$           | Image height                                     |
| $h_{\text{obj}}$           | Object height                                    |
| $h(x,y)$                   | Impulse response                                 |
| $H$                        | Heat capacity                                    |
| $H(\xi,\eta)$              | Transfer function                                |
| HIFOV                      | Horizontal instantaneous field of view           |
| HFOV                       | Horizontal field of view                         |
| $i$                        | Electrical current                               |
| $\bar{i}$                  | Mean current                                     |
| $i_{\text{avg}}$           | Average electrical current                       |
| $i_{\text{bkg}}$           | Background rms current                           |
| $i_{\text{dark}}$          | Dark current                                     |
| $i_j$                      | rms Johnson noise current                        |
| $i_{1/f}$                  | rms 1/f-noise current                            |
| $i_{\text{nG/R}}$          | Generation–recombination (G/R) noise rms current |
| $i_{\text{noise}}$         | Noise current                                    |
| $i_o$                      | Dark current                                     |
| $i_{\text{oc}}$            | Open circuit current                             |
| $i_{\text{pa}}$            | Preamplifier noise rms current                   |

## Glossary of Symbols

---

|                              |  |
|------------------------------|--|
| $i_{\text{ph}}$              | Photogenerated current   |
| $i_{\text{rms}}$             | rms current  |
| $i_{\text{sc}}$              | Short circuit current  |
| $i_{\text{shot}}$            | Shot noise rms current   |
| $i_{\text{sig}}$             | Signal current   |
| IC                           | Integrated circuit   |
| IRFPA                        | Infrared focal plane array   |
| $j$                          | imaginary number   |
| $J$                          | Current density  |
| $k$                          | Boltzmann's constant   |
| $\mathcal{K}(\xi_f)$         | Spatial-frequency-dependant MRTD proportionality factor                  |
| $l_{\text{w}}$               | Width of a well  |
| $L$                          | Atmospheric path length  |
| $L$                          | Radiance   |
| $L_{\text{bkg}}$             | Background radiance  |
| $L_{\text{e}}$               | Radiance in energy units   |
| $L_{\text{p}}$               | Radiance in photon units   |
| $L_{\text{v}}$               | Visual luminance   |
| $L_{\lambda}$                | Spectral radiance  |
| LPE                          | Liquid phase epitaxy   |
| LSF                          | Line spread function   |
| LWIR                         | Longwave infrared  |
| $m_{\text{e}}^*$             | Effective mass of an electron  |
| $M$                          | Exitance   |
| $M_{\text{e}}$               | Exitance in energy units   |
| $M_{\text{meas}}$            | Measured exitance  |
| $M_{\text{obj}}$             | Exitance of an object  |
| $M_{\text{p}}$               | Exitance in photon units   |
| $M_{\lambda}$                | Spectral exitance  |
| MRTD                         | Minimum resolvable temperature difference                                |
| MTF                          | Modulation transfer function   |
| $\text{MTF}_{\text{aer}}$    | Aerosol MTF  |
| $\text{MTF}_{\text{d}}$      | Detector MTF   |
| $\text{MTF}_{\text{linear}}$ | Linear-motion MTF  |
| $\text{MTF}_{\text{post}}$   | Post-sampled MTF (display, digital processing, and the eye-brain filter) |
| $\text{MTF}_{\text{pre}}$    | Pre-sampled MTF (optics detector, and line-of-sight jitter),             |

## Glossary of Symbols

---

|                            |  |
|----------------------------|--|
| $MTF_{\text{random}}$      | Random-motion MTF                                |
| $MTF_{\text{sin}}$         | Sinusoidal-motion MTF                            |
| $MTF_{\text{sys}}$         | System's MTF                                     |
| $MTF_{\text{tur}}$         | Turbulence MTF                                   |
| MWIR                       | Midwave infrared                                 |
| $\mathcal{M}$              | Magnification                                    |
| $\mathcal{M}_{\text{ang}}$ | Angular magnification                            |
| $n$                        | Refractive index                                 |
| $n_{\text{cycles}}$        | Number of cycles needed to discriminate a target |
| $n_d$                      | Number of detectors                              |
| $n_e$                      | Number of photogenerated electrons               |
| $n_{\text{lines}}$         | Number of lines                                  |
| NEI                        | Noise-equivalent irradiance                      |
| NEP                        | Noise-equivalent power                           |
| NETD                       | Noise-equivalent temperature difference          |
| $NETD_{\text{BF}}$         | Background fluctuation NETD                      |
| $NETD_{\text{BLIP}}$       | NETD under BLIP conditions                       |
| $NETD_{\text{TF}}$         | Temperature fluctuation NETD                     |
| $NE\Delta f$               | Noise-equivalent bandwidth                       |
| OTF                        | Optical transfer function                        |
| $p$                        | Photon-based unit subscript                      |
| $\rho$                     | Pyroelectric coefficient                         |
| $p$                        | Momentum of an electron                          |
| $P$                        | Magnitude of internal polarization               |
| $P_{\text{avg}}$           | Average power                                    |
| $P_{\text{chance}}$        | Probability of chance                            |
| $P_{\text{measured}}$      | Field-measured probability                       |
| $P_{\text{observer}}$      | Observer's probability                           |
| PSD                        | Power spectral density                           |
| PSF                        | Point spread function                            |
| PV                         | Photovoltaic (or photodiode)                     |
| $r_o$                      | Fried coherence length                           |
| $R$                        | Resistance                                       |
| $R_d$                      | Detector resistance                              |
| $R_{\text{eq}}$            | Equivalent resistance                            |
| $R_{\text{in}}$            | Input resistance                                 |
| $R_L$                      | Load resistance                                  |
| $R_{\text{out}}$           | Output resistance                                |
| $R_{\text{th}}$            | Thermal resistance                               |

## Glossary of Symbols

---

|                        |   |
|------------------------|---|
| RIIC                   | Read-in integrated circuit                  |
| ROIC                   | Read-out integrated circuit                 |
| RSS                    | Root sum square                             |
| $\mathcal{R}$          | Responsivity                                |
| $\mathcal{R}_i$        | Current responsivity                        |
| $\mathcal{R}_v$        | Voltage responsivity                        |
| $\mathcal{R}(T)$       | Blackbody responsivity                      |
| $\mathcal{R}(\lambda)$ | Spectral responsivity                       |
| SCN <sub>tmp</sub>     | Scene contrast temperature                  |
| SL                     | Superlattice                                |
| SNR                    | Signal-to-noise ratio                       |
| SR                     | Strehl-intensity ratio                      |
| SRR <sub>out</sub>     | Out-of-band spurious response ratio         |
| $t$                    | Time  |
| $T$                    | Temperature                                 |
| $T_{\text{bkg}}$       | Background temperature                      |
| $T_c$                  | Curie temperature                           |
| $T_d$                  | Detector temperature                        |
| $T_{\text{load}}$      | Load temperature                            |
| $T_{\text{source}}$    | Source temperature                          |
| $T_{\text{target}}$    | Target temperature                          |
| TRC                    | Thermal resistance coefficient              |
| VFOV                   | Vertical field of view                      |
| VIFOV                  | Vertical instantaneous field of view        |
| $x$                    | Alloy composition or molar fraction ratio   |
| $\alpha$               | Coefficient of absorption                   |
| $\alpha$               | Thermal resistance coefficient              |
| $\Delta f$             | Electronic frequency bandwidth              |
| $\Delta t$             | Time interval                               |
| $\Delta T$             | Temperature difference                      |
| $\Delta \lambda$       | Wavelength interval                         |
| $\varepsilon$          | Emissivity                                  |
| $\eta$                 | Spatial frequency in the vertical direction |
| $\eta$                 | Quantum efficiency                          |
| $\eta_{\text{scan}}$   | Scan efficiency                             |
| $\theta$               | Angle variable                              |
| $\theta_{\text{max}}$  | Maximum angle subtense                      |
| $\Theta$               | Seebeck coefficient                         |

## Glossary of Symbols

---

|                             |  |
|-----------------------------|--|
| $\lambda$                   | Subscript indicating a spectral radiometric quantity |
| $\lambda$                   | Wavelength   |
| $\lambda_{\text{cutoff}}$   | Cutoff wavelength                                    |
| $\lambda_{\text{cuton}}$    | Cuton wavelength                                     |
| $\lambda_{\text{max}}$      | Maximum wavelength                                   |
| $\lambda_{\text{max-cont}}$ | Maximum-contrast wavelength                          |
| $\lambda_o$                 | Fixed wavelength                                     |
| $\lambda_{\text{peak}}$     | Peak wavelength                                      |
| $\Lambda$                   | de Broglie wavelength                                |
| $\mu$                       | Vertical sample frequency                            |
| $\nu$                       | Optical frequency                                    |
| $\xi$                       | Spatial frequency in the horizontal direction        |
| $\xi_{\text{cutoff}}$       | Spatial cutoff frequency                             |
| $\xi_{\text{cuton}}$        | Spatial cuton frequency                              |
| $\xi_J$                     | Johnson spatial frequency                            |
| $\rho$                      | Electric charge                                      |
| $\rho$                      | Reflectance  |
| $\sigma$                    | Standard deviation                                   |
| $\sigma$                    | Atmospheric extinction coefficient                   |
| $\sigma^2$                  | Variance   |
| $\sigma_a$                  | Random amplitude of the jitter                       |
| $\sigma_e$                  | Stefan–Boltzmann constant in energy units            |
| $\sigma_{\text{eye}}$       | rms visual noise expressed at a display              |
| $\sigma_n$                  | rms noise filtered by a display                      |
| $\sigma_p$                  | Stefan–Boltzmann constant in photon units            |
| $\tau$                      | Transmittance  |
| $\tau_{\text{atm}}$         | Atmospheric transmittance                            |
| $\tau_{\text{dwell}}$       | Dwell time   |
| $\tau_{\text{external}}$    | External transmittance                               |
| $\tau_{\text{frame}}$       | Frame time   |
| $\tau_{\text{int}}$         | Integration time                                     |
| $\tau_{\text{internal}}$    | Internal transmittance                               |
| $\tau_{\text{line}}$        | Line time  |
| $\tau_{\text{opt}}$         | Optical transmittance                                |
| $\tau_{\text{peak}}$        | Peak transmittance                                   |
| $\tau_{\text{RC}}$          | Electrical time constant                             |
| $\tau_{\text{th}}$          | Thermal time constant                                |

## Glossary of Symbols

---

|                       |                             |
|-----------------------|-----------------------------|
| $v$                   | Horizontal sample frequency |
| $\bar{v}$             | Mean voltage                |
| $v_{\text{det}}$      | Detector voltage            |
| $v_{\text{in}}$       | Input voltage               |
| $v_j$                 | Johnson noise rms voltage   |
| $v_n$                 | rms noise voltage           |
| $v_{\text{oc}}$       | Open-circuit voltage        |
| $v_{\text{out}}$      | Output voltage              |
| $v_{\text{sc}}$       | Short-circuit voltage       |
| $v_s$                 | Shot-noise rms voltage      |
| $v_{\text{scan}}$     | Scan velocity               |
| $v_{\text{sig}}$      | Signal voltage              |
| $\phi$                | Flux                        |
| $\phi_{\text{abs}}$   | Absorbed flux               |
| $\phi_{\text{bkg}}$   | Background flux             |
| $\phi_d$              | Detector flux               |
| $\phi_e$              | Radiant flux in watts       |
| $\phi_{\text{img}}$   | Flux incident on an image   |
| $\phi_{\text{inc}}$   | Incident flux               |
| $\phi_{\text{obj}}$   | Flux radiated by an object  |
| $\phi_p$              | Photon flux                 |
| $\phi_{\text{sig}}$   | Signal flux                 |
| $\phi_{\text{trans}}$ | Transmitted flux            |
| $\phi_\lambda$        | Spectral flux               |
| $\psi$                | Eigenfunction               |
| $\omega$              | Angular frequency           |
| $\Omega$              | Solid angle                 |
| $\Omega_{\text{bkg}}$ | Background solid angle      |
| $\Omega_d$            | Detector solid angle        |
| $\Omega_{\text{opt}}$ | Optical solid angle         |
| $\Omega_s$            | Source solid angle          |

## History of Infrared Detectors and Systems

---

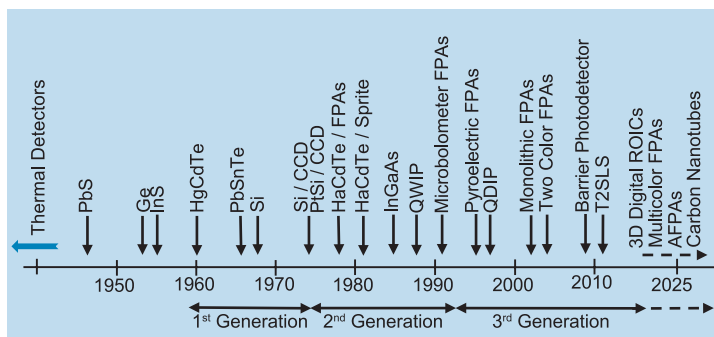
**Infrared imaging systems** trace their origins to the year 1800 when John Frederik William Herschel's experiments on refraction of invisible rays using a prism and a monochromator discovered infrared radiation, which Herschel called "calorific rays."

The initial infrared **radiation detection systems** were based on thermometers, thermocouples, and bolometers. In 1821, Thomas Johann Seebeck discovered the thermoelectric effect, and soon thereafter, in 1829, Leopoldo Nobili created the first thermocouple. Then in 1835, together with Macedonio Melloni, Nobili constructed a thermopile capable of sensing a person 10 m away. Samuel Pierpont Langley invented the first bolometer/thermistor in 1878. This radiant-heat detector was sensitive to differences in temperature of one hundred-thousandth of a degree Celsius, which enabled the study of the solar irradiance far into the infrared spectrum.

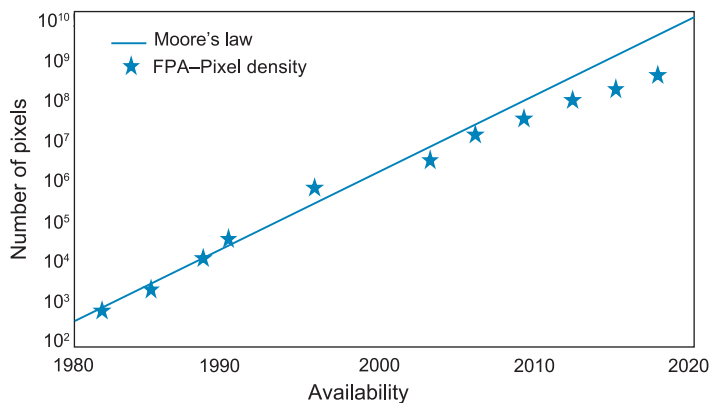
The development of modern **infrared detectors** became possible after John Bardeen and William Shockley invented the transistor in 1947. Thereafter, InSb, HgCdTe, and Si photon detectors were developed. Texas Instruments developed the first forward-looking infrared system in 1963, with production in 1966, and in 1969, the charge-coupled device (CCD) was developed by AT&T Bell Labs. Photon infrared technology combined with molecular beam epitaxy and photolithographic processes revolutionized the semiconductor industry, thus enabling the design and fabrication of complex focal plane arrays.

Three generations of systems may be considered for the foremost military and civilian applications. The first-generation systems were scanning systems limited to single and sparsely populated linear array elements. These devices did not include multiplexing functions in the focal plane. Monolithic and hybrid detector FPA technology with multiplexing read-out circuitry in the focal plane belong to the second-generation systems. Third-generation FPAs are being actively developed and contain several orders of magnitude more pixel elements than the second-generation, as well as many other superior on-chip features.

## Detector IRFPA Roadmap



Since 1980, the size of **infrared focal plane arrays (IRFPAs)** has been increasing at an exponential rate following Moore's law, with the number of pixel elements doubling nearly every  $1\frac{1}{2}$  years. Essentially, the FPA technology has been increasing at the same rate as random-access memory integrated circuits (RAMICs), but lag in size by approximately 10 years. The pixel density of IRFPAs will keep increasing with time but perhaps below Moore's curve. Most high-volume commercial applications can be utterly satisfied with the current array formats. Market forces that demanded larger FPAs in the past have loosened their grip now that the megapixel barrier has been broken. Military projects will continue to demand larger arrays.





## Infrared Detectors

---

Infrared detectors are transducers that sample the incident radiation and produce an electrical signal proportional to the total flux incident on the detector surface. There are two main classes of infrared detectors: **thermal** and **photon detectors**. Both types respond to absorbed photons, but each type uses different response mechanisms, which lead to variations in speed, spectral responsivity, and sensitivity. Thermal detectors depend on the changes in the electrical or mechanical properties of the sensing materials (e.g., resistance, capacitance, voltage, mechanical displacement) that result from temperature changes caused by the heating effect of the incident radiation. The change in these electrical properties with input flux level is measured by an external electrical circuit. The thermal effects do not depend on the photonic nature of the incident infrared radiation; they have no inherent long-wavelength cutoff. Their sensitivity limitation is due to thermal flux and/or the spectral properties of the protective window in front of them. The response rate of a thermal detector is slow due to the time required for the device to heat up after the incident flux has been absorbed. Examples of different classes of thermal detectors are **bolometers**, **pyroelectric detectors**, **thermopiles**, **Golay cells**, and **superconductors**.

The two basic types of semiconductor photon detectors are photoconductors and photovoltaics (or photodiodes). The photonic effects in these devices result from direct conversion of incident photons into conducting electrons within the material. An absorbed photon instantaneously excites an electron from the nonconducting state into a conducting state, causing a change in the electrical properties of the semiconductor material that can be measured by an external circuit. Photon detectors are very fast; however, their response speed is generally limited by the resistance-capacitance (RC) product of the read-out circuit or detector combined with input circuit capacitance.

Detector performance is described in terms of **responsivity**, **noise-equivalent power**, or **detectivity**. These figures of merit enable a quantitative prediction and evaluation of the system, and allow for comparison of relative performance between different detector types.

## Primary Sources of Detector Noise

Noise is a random fluctuation in electrical output from a detector and must be minimized to increase the performance sensitivity of an infrared system. Sources of optical-detector noise can be classified as either external or internal. However, the focus here is on the internally generated detector noises that include shot, generation–recombination, one over frequency ( $1/f$ ), and temperature fluctuation, which are a function of the detector area, bandwidth, and temperature. It is possible to determine the limits of detector performance set by the statistical nature of the radiation to which it responds. Such limits set the lower level of sensitivity and can be ascertained by the fluctuations in the signal or background radiation falling on the detector.

Random noise is expressed in terms of an electrical variable such as a voltage, current, or power. If the voltage is designated as a random-noise waveform  $v_n(t)$  and a certain probability-density function is assigned to it, its statistics are found as a function of the following statistical descriptors:

**Mean:**  $\overline{v_n} = \frac{1}{T} \int_0^T v_n(t) dt$  [volts]

**Variance or mean-square:**

$$\overline{v_n^2} = \overline{(v_n(t) - \overline{v_n})^2} = \frac{1}{T} \int_0^T [v_n(t) - \overline{v_n}]^2 dt \quad [V^2]$$

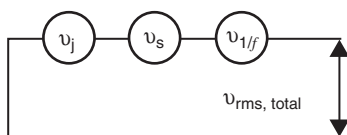
**Standard deviation:**

$$v_{\text{rms}} = \overline{\Delta v_n} = \sqrt{\frac{1}{T} \int_0^T [v_n(t) - \overline{v_n}]^2 dt} \quad [V]$$

where  $T$  is the time interval. The standard deviation represents the rms noise of the random variable.

Linear addition of independent intrinsic noise sources is carried out in power (variance), not in voltage noise (standard deviation); the total rms noise of random quantities is added in quadrature:

$$v_{\text{rms, total}} = \sqrt{v_{\text{rms, 1}}^2 + v_{\text{rms, 2}}^2 + \cdots + v_{\text{rms, n}}^2}$$



Assuming three sources of noise, Johnson, shot, and  $1/f$  noise,

$$v_{\text{rms, total}}^2 = v_j^2 + v_s^2 + v_{1/f}^2$$

## Noise Power Spectral Density

Noise can also be described in the frequency domain. The **power spectral density (PSD)**, or the mean-square fluctuation per unity frequency range, provides a measurement of frequency distribution of the mean-square value of the data (i.e., distribution of power).

For random processes, frequency can be introduced through the autocorrelation function. The time-average **autocorrelation** function of a voltage waveform may be defined as

$$c_n(\tau) = \lim_{T \rightarrow \infty} \frac{1}{T} \int_{-T/2}^{T/2} v_n(t)v_n(t+\tau)dt$$

where the autocorrelation is the measure of how fast the waveform changes in time. The PSD of a wide-sense stationary random process is defined as the Fourier transform of the autocorrelation function (Wiener-Khinchine theorem):

$$\text{PSD} = N(f) = \mathcal{F}\{c_n(\tau)\} = \int_{-\infty}^{\infty} c_n(\tau)e^{-j2\pi f\tau}d\tau$$

The inverse relation is

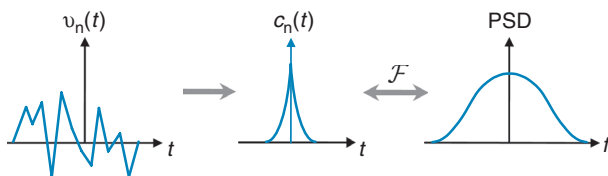
$$c_n(\tau) = \mathcal{F}^{-1}\{N(f)\} = \int_{-\infty}^{\infty} N(f)e^{j2\pi f\tau}df$$

Using the **central-ordinate theorem** yields

$$c_n(0) = \int_{-\infty}^{\infty} N(f)df = \int_{-\infty}^{\infty} v_n^2(t)dt = \overline{v_n^2(t)}$$

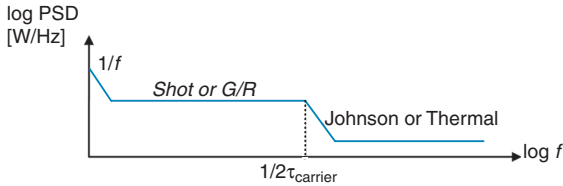
The average power of the random voltage waveform is obtained by integrating the PSD over its entire range of definition.

Uncorrelated noise such as white noise implies that its autocorrelation function is a delta function. The PSD of such random processes is a constant over the entire frequency range, but in practice, the PSD is constant over a wide but final range (i.e., it is bandpass limited).



## White Noise

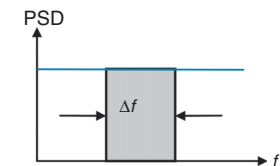
Detector noise curves have different frequency contents. A typical PSD plot for a sensor system is shown.



- $1/f$  noise can be partly excluded by ac coupling (i.e., cut off the system dc response by using a high pass filter with a cutoff between 1 Hz and 1 KHz).
- Shot noise and generation–recombination (G/R) noise have a roll-off frequency in the midband range ( $\approx 20$  KHz–1 MHz), proportional to the inverse of the carrier lifetime.
- Johnson noise and amplifier noise are usually flat to high frequencies past  $1/2\tau_{\text{carrier}}$ .
- In a photon sensor, the charge carriers transmit both signal and noise; therefore, the upper cutoff frequency of the electronic bandwidth should not be higher than  $1/2\tau_{\text{carrier}}$ ; i.e., wider bandwidth includes more noise, but not more signal.

Most system-noise calculations are done in the **white noise** region, where the PSD is flat over sufficient broadband relative to the signal band of interest. Shot and G/R noises are white up to  $f \approx 1/2\tau_{\text{carrier}}$ ; beyond that, they roll off. For white noise, the noise power is directly proportional to the detector bandwidth; consequently, the rms noise voltage is directly proportional to the square root of the detector bandwidth.

Detectors have a temporal impulse response with a width



Noise power:  $\text{PSD} \propto \Delta f = 1/2\tau$

rms noise voltage:  $v_{\text{rms}} \propto \sqrt{\Delta f} = \sqrt{1/2\tau}$

of  $\tau$ . This response time or integration time is related to the frequency bandwidth as  $\Delta f = 1/2\tau$ .

If the input noise is white, then the noise-equivalent bandwidth of the filter determines how much noise power is passed through the system.

As the integration time shortens, the noise-equivalent bandwidth widens and the system becomes noisier, while using a measurement circuit with longer response time yields a system with less noise.

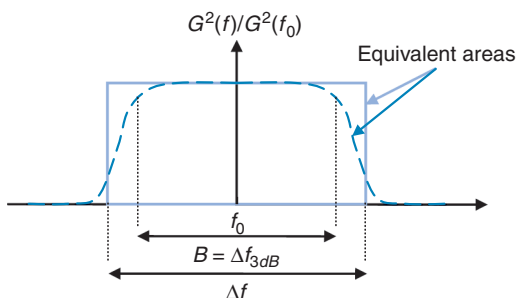
## Noise-Equivalent Bandwidth (NE $\Delta f$ )

The **noise-equivalent bandwidth** (NE $\Delta f$  or simply  $\Delta f$ ) of an ideal electronic amplifier has a constant power-gain distribution between its lower and upper frequencies, and zero elsewhere. It can be represented as a rectangular function in the frequency domain. However, real electronic frequency responses do not have such ideal rectangular characteristics, so it is necessary to find an equivalent bandwidth that would provide the same amount of noise power.

The noise-equivalent bandwidth is defined as

$$\text{NE}\Delta f \equiv \frac{1}{G^2(f_0)} \int_{-\infty}^{\infty} |G(f)|^2 df$$

where  $G(f)$  is the power gain as a function of frequency, and  $G(f_0)$  is the maximum value of the power gain. The most



common definition of bandwidth is the frequency interval within which the power gain exceeds one-half of its maximum value (i.e., 3-dB

bandwidth, which is usually denoted by  $B$ ).

The above definition of noise-equivalent bandwidth assumes white noise; that is, the power spectrum of noise is flat. However, if the noise power spectrum exhibits strong frequency dependence, the noise-equivalent bandwidth should be calculated from

$$\text{NE}\Delta f \equiv \frac{1}{G^2(f_0)\overline{v_n^2}} \int_{-\infty}^{\infty} \overline{v_n^2(f)} G^2(f) df$$

where  $\overline{v_n^2(f)}$  is the mean-square noise voltage per unit bandwidth, and  $\overline{v_n^2}$  is the mean-square noise voltage per unit bandwidth measured at a frequency high enough that the PSD of the noise is flat.

### Noise-Equivalent Bandwidth (NE $\Delta f$ ) (cont.)

For noise-equivalent bandwidth calculations, two impulse response forms are commonly considered: square and exponential. The square impulse response is most commonly used to relate response time and noise-equivalent bandwidth. The exponential impulse response arises from charge-carrier lifetime or by measuring the RC time constants in electrical circuits.

A square impulse response with a pulse width  $\tau$  can be expressed as a rectangular function as

$$v(t) = v_0 \text{rect}[(t - t_0)/\tau]$$

Applying the Fourier transform, the normalized voltage transfer function is obtained:

$$\frac{V(f)}{V_0} = e^{-j2\pi f t_0/\tau} \text{sinc}(\pi f \tau)$$

Substituting into the NE $\Delta f$  equation and solving the integral,

$$\text{NE}\Delta f = \int_{-\infty}^{\infty} |e^{-j2\pi f t_0/\tau} \text{sinc}(\pi f \tau)|^2 df = \frac{1}{2\tau}$$

The calculation of the noise-equivalent bandwidth from an exponential impulse response is obtained as follows:

The exponential impulse response can be specified as

$$v(t) = v_0 \exp(t/\tau) \text{step}(t)$$

Fourier transforming gives

$$\frac{V(f)}{V_0} = \frac{1}{1 + j2\pi f \tau}$$

and taking the absolute value squared yields

$$\left| \frac{V(f)}{V_0} \right|^2 = \frac{1}{1 + (2\pi f \tau)^2}$$

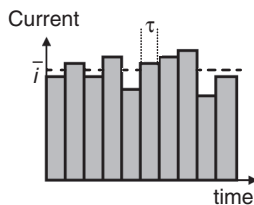
Integrating yields the following noise-equivalent bandwidth:

$$\text{NE}\Delta f = \int_{-\infty}^{\infty} \frac{df}{1 + (2\pi f \tau)^2} = \frac{1}{4\tau}$$

## Shot Noise

The **shot noise** mechanism is associated with the nonequilibrium conditions in a potential energy barrier of a photovoltaic detector through which a dc current flows. Shot noise is a result of the discrete nature of the current carriers and therefore of the current-carrying process. The dc current is viewed as the sum of many short and small current pulses, each of which is contributed by the passage of a single electron or hole through the junction depletion layer. This type of noise is practically white, considering the spectral density of a single narrow pulse.

The generation of the carriers is random according to photon arrival times. However, once a carrier is generated, its recombination is no longer random; it is actually determined by transit-time considerations that obey Poisson statistics, which state that the variance equals the mean.



$\tau$  = interval of integration.

To determine the expression for the mean-square current fluctuation at the output of the measuring circuit, the current is measured during a time interval  $\tau$ :

$$i = \frac{n_e q}{\tau}$$

where  $q$  is the electron charge, and  $n_e$  is the number of photogenerated electrons within  $\tau$ . The average current can be related to the average number of electrons created by

$$\bar{i} = \frac{\bar{n}_e q}{\tau} \Rightarrow \bar{n}_e = \frac{\bar{i} \tau}{q}$$

The mean-square fluctuation averaged over many independent measuring times  $\tau$  is

$$\overline{i_{n, \text{shot}}^2} = \overline{(i - \bar{i})^2} = \frac{q^2}{\tau^2} \overline{(n_e - \bar{n}_e)^2} = \frac{q^2}{\tau^2} \bar{n}_e$$

which yields the expression of the shot noise:

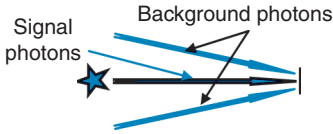
$$\overline{i_{n, \text{shot}}^2} = \frac{\bar{i} q}{\tau} = 2q \bar{i} \Delta f \Rightarrow i_{n, \text{shot}} = \sqrt{2q \bar{i} \Delta f}$$

## Signal-to-Noise Ratio: Detector and BLIP Limits

Is the **signal-to-noise ratio (SNR)** predominantly generated by the signal or the background?

Considering the current generated primarily by signal photons, without any extraneous radiation present, the signal current from the detector is

$$i_{\text{sig}} = \phi_{\text{p,sig}} \eta q$$



where  $\eta$  is the quantum efficiency (electrons per photon). Similarly, the current generated by the background flux is

$$\text{Detector current: } i_{\text{total}} = i_{\text{sig}} + i_{\text{bkg}}$$

$$i_{\text{bkg}} = \phi_{\text{p,bkg}} \eta q$$

The SNR is the ratio of the signal current to the shot noise, namely,

$$\text{SNR} = \frac{i_{\text{sig}}}{i_{\text{n,shot}}} = \frac{\phi_{\text{p,sig}} \eta q}{\sqrt{2q i_{\text{total}} \Delta f}} = \frac{\phi_{\text{p,sig}} \eta q}{\sqrt{2q(\phi_{\text{p,sig}} \eta q + \phi_{\text{p,bkg}} \eta q) \Delta f}}$$

Assuming that the dominant noise contribution is the shot noise generated by the signal-power envelope (i.e.,  $\phi_{\text{sig}} \gg \phi_{\text{bkg}}$ ),

$$\text{SNR} \cong \frac{\phi_{\text{p,sig}} \eta}{\sqrt{2\phi_{\text{p,sig}} \eta \Delta f}} = \sqrt{\phi_{\text{p,sig}} \eta \tau}$$

which states that the SNR increases as the square root of the signal flux, thus improving the sensitivity of the system.

With a weak signal source detected against a large background, which is the most common situation in infrared applications, the dominant noise contribution is associated with the shot noise of the background (i.e.,  $\phi_{\text{bkg}} \gg \phi_{\text{sig}}$ ). The photodetector is said to be background limited, yielding

$$\text{SNR}_{\text{BLIP}} \cong \frac{\phi_{\text{p,sig}} \eta}{\sqrt{2\phi_{\text{p,bkg}} \eta \Delta f}} = \phi_{\text{p,sig}} \sqrt{\frac{\eta \tau}{\phi_{\text{p,bkg}}}}$$

$\text{SNR}_{\text{BLIP}}$  is inversely proportional to the square root of the background flux; therefore, reducing the background photon flux increases the SNR when the system is operating in the **background-limited infrared photodetector (BLIP)** mode.



## Generation–Recombination Noise

**Generation–recombination (G/R) noise** is caused by fluctuations in the rates of thermal generation and recombination of free carriers in semiconductor devices without potential barriers (e.g., photoconductors), thereby giving rise to a fluctuation in the average carrier concentration. Thus, the electrical resistance of the semiconductor material changes, which can be observed as fluctuating voltage across the sample when the bias current flows through it.

The transverse photoconductivity geometry and circuit are shown.

Once a carrier is generated, it travels under the influence of an applied electric field. The carrier lasts until recombination occurs at a random time consistent with the mean carrier lifetime  $\tau_{\text{carrier}}$ . The statistical fluctuation in the concentration of carriers produces white noise.

The current noise expression for generation–recombination noise is given by

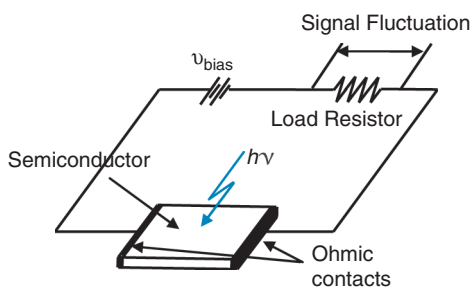
$$i_{n,G/R} = 2qG\sqrt{\eta E_p A_d \Delta f + g_{th} \Delta f}$$

where  $G$  is the photoconductive gain, and  $g_{th}$  is the thermal generation of carriers. Since photoconductors are cooled cryogenically, the second term under the square root in the above equation can be neglected. Assuming that  $G$  equals unity,

$$i_{n,G/R} = 2q\sqrt{\eta E_p A_d \Delta f}$$

$$i_{n,G/R} = \sqrt{2}i_{n,shot}$$

Note that the rms G/R noise is  $\sqrt{2}$  larger than for shot noise, since both generation and recombination mechanisms are random processes.

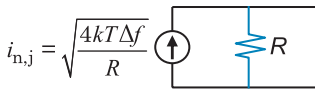


## Johnson Noise

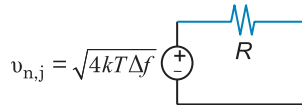
If the background flux is reduced enough, the noise floor is determined by the **Johnson noise**, also known as Nyquist or thermal noise. The fluctuation is caused by the thermal motion of charge carriers in resistive materials, including semiconductors, and occurs in the absence of electrical bias as a fluctuating rms voltage or current.

Johnson noise is an ideal noise-free resistor of the same resistance value, combined either in series with an rms noise voltage or in parallel with an rms noise current.

Norton model:  $R$  in parallel with rms noise current



Thevenin model:  $R$  in series with rms noise voltage



When multiplying the Johnson noise in terms of noise voltage and current spectra,

$$\sqrt{4kTR} \left[ \text{V}/\sqrt{\text{Hz}} \right] \quad \text{and} \quad \sqrt{\frac{4kT}{R}} \left[ \text{A}/\sqrt{\text{Hz}} \right]$$

the power spectral density of the Johnson noise depends only on temperature, and not on resistance:

$$\text{PSD} = 4kT \left[ \text{W}/\text{Hz} \right]$$

Often the detector is cooled to cryogenic temperatures, while the load resistance is at room temperature. In combination, both parallel resistors are added as usual, but the rms noises are added in quadrature, yielding

$$i_{n,j} = \sqrt{i_d^2 + i_L^2} = \sqrt{4k\Delta f \left[ \frac{T_d}{R_d} + \frac{T_L}{R_L} \right]}$$

The SNR in the Johnson noise limit is given by

$$\text{SNR}_j \cong \frac{\phi_{p,\text{sig}} \eta q}{\sqrt{\frac{4kT}{R} \Delta f}}$$

Johnson noise is independent of the photogeneration process; therefore, the SNR is directly proportional to the quantum efficiency.

## 1/f Noise and Temperature Noise

**1/f noise** is found in semiconductors and increases at low frequencies. It is characterized by a spectrum in which the noise power depends approximately inversely on the frequency. The general expression for 1/f noise current is given by

$$i_{n,f} = \sqrt{\mathcal{K} \frac{\bar{i}^\alpha \Delta f}{f^\beta}}$$

where  $\mathcal{K}$  is a proportionality factor,  $\bar{i}$  is the average dc current,  $f$  is the frequency,  $\Delta f$  is the measuring bandwidth,  $\alpha$  is a constant of  $\sim 2$ , and  $\beta$  ranges from  $\sim 0.5$  to  $1.5$ .

Although the cause of 1/f noise is not fully understood, it appears to be associated with the presence of potential barriers at the nonohmic contacts and the surface of the semiconductor.

1/f noise is typically the dominant noise to a few hundred hertz, and is often significant to several kilohertz. It is always present in microbolometers and photoconductors because there is always a dc-bias current flowing within the detector material. However, 1/f noise can be eliminated in photovoltaic detectors operating in open-circuit voltage mode when no dc-bias current is allowed to flow through the diode.

**Temperature noise** is caused by fluctuations in the temperature of the detector due to fluctuations in the rate at which heat is transferred from the sensitive element to its surroundings (i.e., radiative exchange and/or conductance with a heat sink). The spectrum of the mean-square fluctuation in temperature is given by

$$\overline{\Delta T^2} = \frac{4kKT^2}{K^2 + (2\pi f)^2 H^2}$$

where  $k$  is Boltzmann's constant,  $K$  is the thermal conductance,  $H$  is the heat capacity, and  $T$  is the temperature.

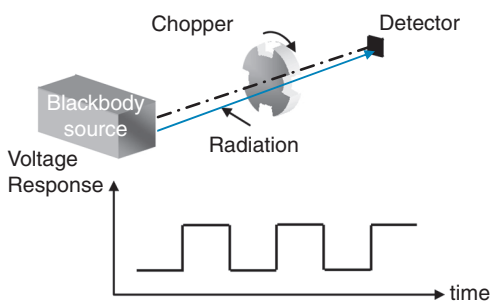
Temperature noise is primarily observed in thermal detectors and, being temperature-noise limited, provides superior performance. The power spectrum of the temperature noise is flat.

## Detector Responsivity

**Responsivity** gives the response magnitude of the detector. It provides information on gain, linearity, dynamic range, and saturation level. Responsivity is a measure of the transfer function between the input signal photon power or flux and the detector electrical signal output:

$$\mathcal{R} = \frac{\text{output signal}}{\text{input flux}}$$

where the output can be in volts or amperes, and the input in watts or photons/sec.  $\mathcal{R}_i$  is **current responsivity**, and  $\mathcal{R}_v$  is **voltage responsivity**. A common technique in detection is to modulate the radiation to be detected and to measure the modulated component of the electrical output of the detector. This technique provides some discrimination against electrical noise since the signal is contained only within the Fourier component of the electrical signal at the modulation frequency, whereas electrical noise is often broadband. Furthermore, it avoids baseline drifts that affect electronic amplifiers due to ac coupling. The output voltage would vary from peak to valley.



An important characteristic of a detector is how fast it responds to a pulse of optical radiation. The voltage response to radiation modulated at frequency  $f$  is defined as

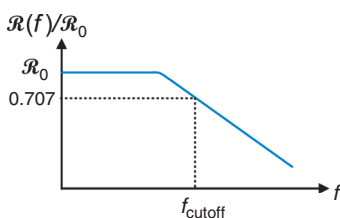
$$\mathcal{R}_v(f) = \frac{v_{\text{sig}}(f)}{\phi_{\text{sig}}(f)}$$

where  $\phi_{\text{sig}}(f)$  is the rms value of the signal flux contained within the harmonic component at frequency  $f$ , and  $v_{\text{sig}}(f)$  is the rms output voltage within this same harmonic component.

In general, the responsivity  $\mathcal{R}(f)$  of a detector decreases as the modulation frequency  $f$  increases. Changing the

### Detector Responsivity (cont.)

angular speed of the chopper, the responsivity can be obtained as a function of frequency. A typical responsivity-versus-frequency curve is plotted.



The cutoff frequency  $f_{\text{cutoff}}$  is defined as the modulation frequency at which  $|\mathcal{R}_v(f_{\text{cutoff}})|^2$  falls to one-half of its maximum value, and is related to response time as

$$f_{\text{cutoff}} = \frac{1}{2\pi\tau}$$

The response time of a detector is characterized by its **responsive time constant**, the time required for the detector output to reach 63% ( $1 - 1/e$ ) of its final value after a sudden change in the irradiance. For most sensitive devices, the response to a change in irradiance follows a simple exponential law. As an example, if a delta-function pulse of radiation  $\delta(t)$  is incident on the detector, an output voltage signal (i.e., the impulse response) of the form

$$v(t) = v_0 e^{-t/\tau} \quad t \geq 0$$

is produced, where  $\tau$  is the time constant of the detector. Transforming this time-dependent equation into the frequency domain by using the corresponding Fourier transform yields

$$V(f) = \frac{v_0 \tau}{1 + j2\pi f \tau}$$

which can be extended to responsivity as

$$\mathcal{R}_v(f) = \frac{\mathcal{R}_0}{1 + j2\pi f \tau}$$

where  $\mathcal{R}_0 = v_0 \tau$  is the dc value of the responsivity. The modulus is written as

$$|\mathcal{R}_v(f)| = \frac{\mathcal{R}_0}{\sqrt{1 + (2\pi f \tau)^2}}$$

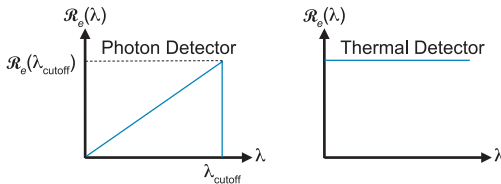
## Spectral Responsivity

Responsivity depends on the wavelength of the incident radiation beam; therefore, the spectral response of a detector can be specified in terms of its responsivity as a function of wavelength. **Spectral responsivity**  $\mathcal{R}(\lambda, f)$  is the output signal response to monochromatic radiation incident on the detector, modulated at frequency  $f$ . It determines the amplifier gain required to bring the detector output up to acceptable levels. To measure the spectral responsivity of a detector, a tunable narrowband source is required.

In energy-derived units, the spectral responsivity for a thermal detector is independent of wavelength (i.e., 1 W of radiation produces the same temperature rise at any spectral line). Therefore, its spectral response is limited by the spectral properties of the material of the window placed in front of the detector. In a photon detector, the ideal spectral responsivity is linearly proportional to the wavelength:

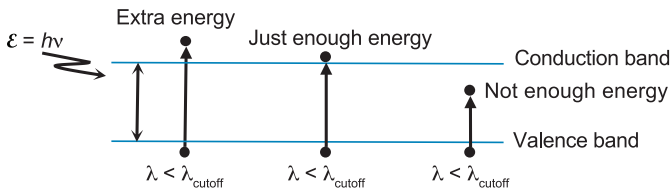
$$\mathcal{R}_e(\lambda) = \mathcal{R}_e(\lambda_{\text{cutoff}}) \frac{\lambda}{\lambda_{\text{cutoff}}}$$

Photons with  $\lambda > \lambda_{\text{cutoff}}$  are not absorbed by the material of the detector and are therefore not detected.



Long-wavelength cutoff is the longest wavelength detected by a sensor made of a material with a certain energy gap and is given by

$$\lambda_{\text{cutoff}} = \frac{hc}{\mathcal{E}_{\text{gap}}}$$



## Blackbody Responsivity

---

An expression to determine the energy gap in electron-volt units is

$$\mathcal{E}_{\text{gap}} = \frac{hc}{\lambda_{\text{cutoff}}} \cdot \frac{1 \text{ eV}}{1.6 \times 10^{-19} \text{ J}} = \frac{1.24}{\lambda_{\text{cutoff}}}$$

The energy gap of silicon is 1.12 eV; therefore, photons with  $\lambda > 1.1 \mu\text{m}$  are not detected. The photogenerated current of a photon detector is given by

$$i = \eta \phi_p q$$

where  $q$  is the elementary charge of an electron:  $1.6 \times 10^{-19}$  C (coulombs). The current spectral responsivity in photon-derived units is

$$\mathcal{R}_{i,p} = \frac{i}{\phi_p} = \eta q \quad [\text{Amp/Ph} \times \text{sec}^{-1}]$$

and in energy-derived units is

$$\mathcal{R}_{i,e} = \frac{i}{\phi_e} = \frac{\lambda \eta q}{\phi_p (hc/\lambda)} = \frac{\eta q}{hc} \cdot \lambda \quad [\text{Amp/W}]$$

which as stated before, is a linear function of  $\lambda$ .

**Blackbody responsivity**  $\mathcal{R}(T, f)$  is interpreted as the output produced in response to a watt of input optical radiation from a blackbody at temperature  $T$  modulated at electrical frequency  $f$ . Since a blackbody (BB) source is widely available and rather inexpensive compared to a tunable narrowband laser source, it is more convenient to measure the  $\mathcal{R}(T)$  and calculate its corresponding  $\mathcal{R}_v(\lambda)$ .

For a blackbody that produces a spectral flux  $\phi_\lambda(\lambda)$ , the **detector output voltage** is calculated from the following integral:

$$v_{\text{out,det}} = \int_0^{\lambda_{\text{cutoff}}} \phi_\lambda(\lambda) \mathcal{R}_v(\lambda) d\lambda$$

which determines the contribution to the detector output in those regions where the spectral flux and the voltage spectral responsivity overlap.

When measuring blackbody responsivity, the radiant power on the detector contains all wavelengths of radiation, independent of the spectral response curve of the

## Blackbody Responsivity (cont.)

detector. Using the Stefan–Boltzmann law and some of the basic radiometric principles presented previously, the blackbody responsivity is

$$\mathcal{R}(T) = \frac{v_{\text{out,det}}}{\phi_e} = \frac{\int_0^{\lambda_{\text{cutoff}}} \phi_{e,\lambda}(\lambda) \mathcal{R}_v(\lambda) d\lambda}{\sigma T^4 A_{\text{source}} \Omega_{\text{det}}} = \frac{\int_0^{\lambda_{\text{cutoff}}} M_{e,\lambda}(\lambda) \mathcal{R}_v(\lambda) d\lambda}{\sigma T^4}$$

Substituting the ideal response of a photon detector,

$$\mathcal{R}(T) = \frac{\frac{\mathcal{R}_v(\lambda_{\text{cutoff}})}{\lambda_{\text{cutoff}}} \int_0^{\lambda_{\text{cutoff}}} M_{e,\lambda}(\lambda) \lambda d\lambda}{\sigma T^4}$$

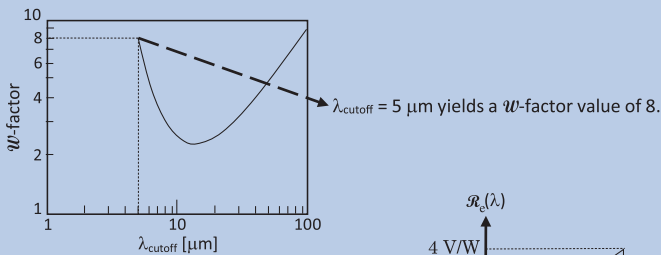
The ratio of  $\mathcal{R}(T)$  to  $\mathcal{R}_v(\lambda)$  is defined by the  $\mathcal{W}$ -factor:

$$\begin{aligned} \mathcal{W}(\lambda_{\text{cutoff}} T) &= \frac{\mathcal{R}_v(\lambda_{\text{cutoff}})}{\mathcal{R}(T)} = \frac{\lambda_{\text{cutoff}} \sigma T^4}{\int_0^{\lambda_{\text{cutoff}}} M_{e,\lambda}(\lambda) \lambda d\lambda} \\ &= \frac{\lambda_{\text{cutoff}} \sigma T^4}{hc \int_0^{\lambda_{\text{cutoff}}} M_{p,\lambda}(\lambda) \lambda d\lambda} \end{aligned}$$

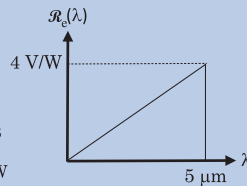
Two standard blackbody temperatures are used to evaluate detectors: (1) 500 K for MWIR and LWIR measurements, and (2) 2850 K for visible and NIR measurements.

**Example:** A detector with  $\lambda_{\text{cutoff}}$  is measured to have  $\mathcal{R}(T = 500 \text{ K}) = 0.5 \text{ V/W}$ . What is  $\mathcal{R}(\lambda)$ ?

Plotting the  $\mathcal{W}$ -factor equation as a function of  $\lambda_{\text{cutoff}}$  for a 500 K blackbody,



$$\begin{aligned} \mathcal{W}(\lambda_{\text{cutoff}} T) &= \frac{\mathcal{R}_v(\lambda_{\text{cutoff}})}{\mathcal{R}(T)} = 8 \\ \Rightarrow \mathcal{R}_v(\lambda_{\text{cutoff}}) &= 8 \times 0.5 = 4 \text{ V/W} \end{aligned}$$

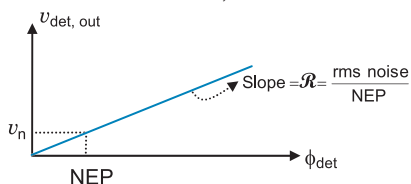




## Noise-Equivalent Power

Although the responsivity is a useful measurement to predict a signal level for a given irradiance, it gives no indication of the minimum radiant flux that can be detected. In other words, it does not consider the amount of noise at the output of the detector that ultimately determines the SNR.

The ability to detect small amounts of radiant energy is inhibited by the presence of noise in the detection process. Since noise produces a random fluctuation in the output of a radiation detector, it can mask the output that is produced



by a weak optical signal. Noise thus sets limits on the minimum input spectral flux that can be detected under given conditions.

One convenient description of this minimum detectable signal is the **noise-equivalent power (NEP)**, which is defined as the radiant flux necessary to give an output signal equal to the detector noise. In other words, it is the radiant power  $\phi_e$  incident on the detector that yields  $\text{SNR} = 1$  and is expressed as the rms noise level divided by the responsivity of the detector:

$$\text{NEP} = \frac{v_n}{\mathcal{R}_v} = \frac{v_n}{v_{\text{sig}}/\phi_{\text{sig}}} = \frac{\phi_{\text{sig}}}{\text{SNR}} \quad [\text{W}]$$

where  $v_n$  denotes the rms voltage produced by a radiation detection system. A smaller NEP implies better sensitivity.

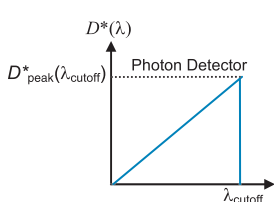
The disadvantage of using the NEP to describe detector performance is that the NEP does not allow a direct comparison of the sensitivity of different detector mechanisms or materials. This is because of its dependence on both the square root of the detector area and the square root of the electronic bandwidth. A descriptor that circumvents this problem is called  $D^*$  (pronounced “dee star”), which normalizes the inverse of the NEP to a 1-cm<sup>2</sup> detector area and 1 Hz of noise bandwidth.

## Specific or Normalized Detectivity

NEP is a situation-specific descriptor useful for design purposes, but it does not allow direct comparison of the sensitivity of different detector materials. The **specific** or **normalized detectivity**  $D^*$  is often used to specify detector performance. It normalizes the noise-equivalent bandwidth and the area of the detector; however, in order to predict the SNR, the sensor area and bandwidth must be chosen for a particular application.

$D^*$  is independent of detector area and electronic bandwidth because the NEP is also directly proportional to the square root of these parameters.  $D^*$  is directly proportional to the SNR as well as to the responsivity:

$$D^* = \frac{\sqrt{A_d \Delta f}}{\text{NEP}} = \frac{\sqrt{A_d \Delta f}}{\phi_d} \text{SNR} = \frac{\sqrt{A_d \Delta f}}{v_n} \mathcal{R}_v \left[ \text{cm} \sqrt{\text{Hz}} / \text{W} \right]$$



Plots of spectral  $D^*$  for photon detectors have the same linear dependency with  $\lambda$ :

$$D^*(\lambda) = D^*_{\text{peak}}(\lambda_{\text{cutoff}}) \frac{\lambda}{\lambda_{\text{cutoff}}}$$

The same  $\mathcal{W}$ -factor applies between  $D^*_{\text{peak}}(\lambda_{\text{cutoff}})$  and  $D^*(T)$ .

The cutoff value of  $D^*(\lambda)$  is defined as the peak spectral value  $D^*_{\text{peak}}(\lambda_{\text{cutoff}})$  and corresponds to the largest potential SNR. In addition, any optical radiation incident on the detector at a wavelength shorter than the cutoff wavelength  $\lambda_{\text{cutoff}}$  has  $D^*(\lambda)$  reduced from the peak  $D^*_{\text{peak}}(\lambda_{\text{cutoff}})$  in proportion to the ratio  $\lambda/\lambda_{\text{cutoff}}$ .

Unlike the NEP,  $D^*$  increases with the sensitivity of the detector. Depending on whether the NEP is spectral or blackbody,  $D^*$  can also be either spectral or blackbody.  $D^*(\lambda, f)$  is the detector's SNR when 1 W of monochromatic radiant flux (modulated at  $f$ ) is incident on a 1-cm<sup>2</sup> detector area within a noise-equivalent bandwidth of 1 Hz. The blackbody  $D^*(T, f)$  is the signal-to-noise output when 1 W of blackbody radiant power (modulated at  $f$ ) is incident on a 1-cm<sup>2</sup> detector within a noise-equivalent bandwidth of 1 Hz.

## Photovoltaic Detectors or Photodiodes

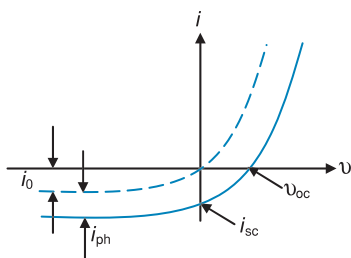
In **photovoltaic (PV) detectors**, more commonly called **photodiodes**, the optical radiation is absorbed at the p-n junction, which produces an output current or voltage.

The photodiode equation is given by

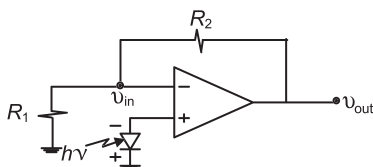
$$i = i_{\text{diode}} - i_{\text{ph}} = i_0 \left[ \exp\left(\frac{qV}{kT}\right) - 1 \right] - \eta q \phi_p$$

where  $i_{\text{ph}}$  is the photo-generated current,  $i_0$  is the dark current,  $q$  is the charge of an electron,  $v$  is the voltage,  $k$  is Boltzmann's constant, and  $T$  is the temperature.

The photodiode operating in each quadrant has different electro-optical characteristics. The most common operating points are open circuit, reverse bias, and short circuit.



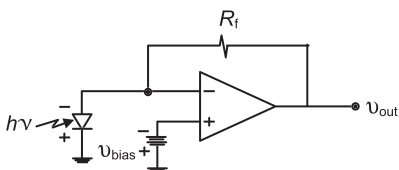
**Open circuit:**



$$v_{\text{oc}} = \frac{kT}{q} \ln \left( \frac{i_{\text{ph}}}{i_0} + 1 \right)$$

$$\frac{v_{\text{out}}}{v_{\text{in}}} = 1 + \frac{R_2}{R_1}$$

**Reverse bias:**



$$v_{\text{out}} = v_{\text{bias}} + R_f i_{\text{ph}}$$

If capacitance  $C$  decreases, then  $RC$  decreases, the junction widens, and the detector response increases.

**Short circuit:** The voltage is zero across the photodiode, and  $i_{\text{ph}}$  is forced to flow into an electrical short circuit:

$$i = i_{\text{ph}} = \eta q \phi_p = \eta q E_p A_d$$

## Sources of Noise in PV Detectors

The sources of noise in a PV detector are

1. shot noise due to the dark current,
2. shot noise due to the signal and background,
3. Johnson noise due to detector resistance,
4. Johnson noise due to the load resistors,
5.  $1/f$  noise associated with the current flow,
6. preamplifier circuit noise, and
7. preamplifier voltage noise.

The noise expression for the photodiode is then

$$i_n^2 = 4q^2 i_0^2 \Delta f + 2q^2 \eta \phi_{p, \text{sig}} \Delta f + 2q^2 \eta \phi_{p, \text{bkg}} \Delta f \\ + 4k\Delta f \left( \frac{T_d}{R_d} + \frac{T_L}{R_L} \right) + \frac{\beta_0 \bar{i} \Delta f}{f} + i_{pa}^2 + v_{pa}^2 (R_L || R_d)$$

where  $R_L$  and  $T_L$  are the load resistance and load temperature, respectively. The preamplifier noise can be made negligible by using low-noise transistors or by cooling the preamplifier to cryogenic temperatures.  $1/f$  noise is almost zero if the device is operating in either open or reverse circuit modes. It is assumed that the dark current is also negligible compared to both the background and signal currents (i.e.,  $i_0 \ll i_{\text{sig}} + i_{\text{bkg}}$ ), and that BLIP conditions are in effect. Under these conditions, the rms shot noise current is approximately

$$i_n \cong \sqrt{2q^2 \eta \phi_{p, \text{bkg}} \Delta f} = \sqrt{2q^2 \eta \phi_{e, \text{bkg}} \frac{\lambda}{hc} \Delta f}$$

Recalling that the peak signal current generated by a photovoltaic detector is

$$i_{\text{signal}} = \phi_{p, \text{sig}} \eta q = \phi_{e, \text{sig}} \eta q \frac{\lambda}{hc}$$

the SNR for a photovoltaic detector is then

$$\text{SNR}_{\text{PV}} = \frac{\phi_{e, \text{sig}} \eta q \frac{\lambda}{hc}}{\sqrt{2q^2 \phi_{e, \text{bkg}} \eta \frac{\lambda}{hc} \Delta f}}$$

Setting  $\text{SNR}_{\text{PV}} = 1$ , the spectral  $\text{NEP}_{\text{PV, BLIP}}$  is obtained:

$$\text{NEP}_{\text{PV, BLIP}}(\lambda) = \sqrt{\frac{hc}{\lambda} \frac{2\phi_{e, \text{bkg}} \Delta f}{\eta}}$$

### Expressions for $D_{\text{PV,BLIP}}^*$ , $D_{\text{PV,BLIP}}^{**}$ , and $D_{\text{PV,JOLI}}^*$

Spectral  $D_{\text{PV,BLIP}}^*$  for a PV detector is obtained from the definition of  $D^*$  in terms of NEP:

$$D_{\text{PV,BLIP}}^*(\lambda) = \frac{\sqrt{A_d \Delta f}}{\text{NEP}_{\text{PV,BLIP}}} = \sqrt{\frac{\lambda}{hc} \frac{\eta}{2E_{\text{e,bkg}}}} = \frac{\lambda}{hc} \sqrt{\frac{\eta}{2E_{\text{p,bkg}}}}$$

If the background is not monochromatic,  $E_{\text{bkg}}$  needs to be integrated over the sensor response from  $\lambda_{\text{cutoff}}$  to  $\lambda_{\text{cutoff}}$ :

$$\begin{aligned} D_{\text{PV,BLIP}}^*(\lambda_{\text{cutoff}}) &= \frac{\lambda_{\text{cutoff}}}{hc} \sqrt{\frac{\eta}{2 \int_{\lambda_{\text{cutoff}}}^{\lambda_{\text{cutoff}}} E_{\text{p,bkg}}(\lambda) d\lambda}} \\ &= (F/\#) \frac{\lambda_{\text{cutoff}}}{hc} \sqrt{\frac{2\eta}{\pi \int_{\lambda_{\text{cutoff}}}^{\lambda_{\text{cutoff}}} L_{\text{p,bkg}}(\lambda) d\lambda}} \end{aligned}$$

where  $E_{\text{p,bkg}} = \pi L_{\text{p,bkg}} \sin^2 \theta \cong \pi L_{\text{p,bkg}} [1/2(F/\#)]^2$ .

$D_{\text{BLIP}}^*$  increases when increasing the  $F/\#$ , which illuminates the detector with a smaller cone of background radiation.  $D^{**}$  normalizes the dependence on  $\sin \theta$ , allowing a comparison of detectors normalized to the hemispherical background:

$$D_{\text{PV,BLIP}}^{**}(\lambda) = \sin \theta D_{\text{PV,BLIP}}^*(\lambda)$$

**Johnson-limited (JOLI) noise performance** occurs in deep-space applications when the shot noise has been decreased. It becomes negligible compared to the Johnson noise:

$$2q^2 \eta (\phi_{\text{p,sig}} + \phi_{\text{p,sig}}) \Delta f \ll 4k\Delta f \left( \frac{T_d}{R_d} + \frac{T_L}{R_L} \right)$$

where  $T_d$  and  $R_d$  are the temperature and resistance of the detector, respectively. The SNR of the PV detector under this condition becomes

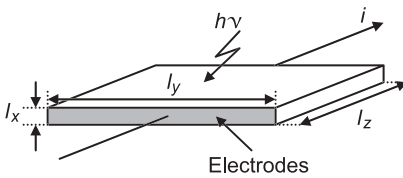
$$\text{SNR}_{\text{PV,JOLI}} = \frac{q\eta\phi_{\text{e,sig}} \frac{\lambda}{hc}}{4k\Delta f \left( \frac{T_d}{R_d} + \frac{T_L}{R_L} \right)} \cong \frac{q\eta\phi_{\text{e,sig}} \frac{\lambda}{hc}}{4k\Delta f \frac{T_d}{R_d}} R_L \gg R_d$$

Setting  $\text{SNR}_{\text{PV,JOLI}} = 1$ , converting the noise-equivalent photon flux to  $\text{NEP}_{\text{PV,JOLI}}$ , and substituting the NEP expression in terms of  $D^*$ ,

$$D_{\text{PV,JOLI}}^* = \frac{\lambda q \eta}{2hc} \sqrt{\frac{R_d A_d}{k T_d}}$$

## Photoconductive Detectors

Shot noise occurs in diodes and other devices with a potential-energy barrier for which the generation is a random process, while recombination is a deterministic process. In



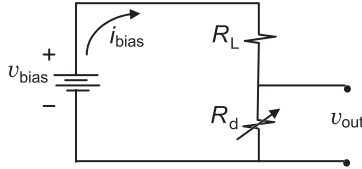
devices such as **photoconductive (PC) detectors** without junctions or other potential-energy barriers, both generation and recombination are random processes.

**Photoconductors** respond to light by changing the resistance or conductance of the detector's material:

$$R_d \propto \frac{1}{\phi_p} \Rightarrow dR_d \propto \frac{d\phi_p}{\phi_p^2}$$

where  $\phi_p$  is the photon flux.

Photoconductive detectors have no junction; therefore, there is no intrinsic field. They cannot operate under open-circuit conditions and do not generate voltage independently (i.e., they must use bias current). In order to detect the change in resistance, a biasing circuit with an applied field must be utilized.



The output voltage is given by

$$v_{out} = \frac{R_d}{R_d + R_L} v_{bias}$$

where a small change in the detector resistance produces a change in signal voltage, which is directly proportional to the change in the photon flux incident on the photoconductive detector:

$$dv_{out} = \frac{dR_d}{(R_d + R_L)^2} v_{bias} \propto \frac{d\phi_p}{(R_d + R_L)^2 \phi_p^2} v_{bias}$$

## Sources of Noise in PC Detectors

The sources of noise in **photoconductors** are listed as

1. generation–recombination (G/R) noise,
2. Johnson noise due to detector resistance,
3. Johnson noise due to load resistors,
4.  $1/f$  noise associated with the current flow,
5. preamplifier circuit noise, and
6. preamplifier voltage noise.

The noise expression for the photoconductive detector is then

$$i_n^2 = 4q^2\eta E_p A_d G^2 \Delta f + 4q^2 g_{th} G^2 \Delta f + 4k\Delta f \left( \frac{T_d}{R_d} + \frac{T_L}{R_L} \right) + \frac{\beta_0 \bar{i} \Delta f}{f} + i_{pa}^2 + v_{pa}^2 (R_L || R_d)$$

where  $g_{th}$  is the thermal generation rate of carriers, and  $G$  is the photoconductive gain.  $G$  is proportional to the number of times an electron can transit the detector electrodes in its lifetime (i.e., excess signal electrons through the PC). The photoconductive gain depends on the detector size, material, and doping, and can vary as  $1 < G < 10^5$ . If  $G < 1$ , the electron does not reach the electrode before recombining. Usually PC detectors are cooled cryogenically, in which case the thermal term in the generation–recombination noise is negligible.

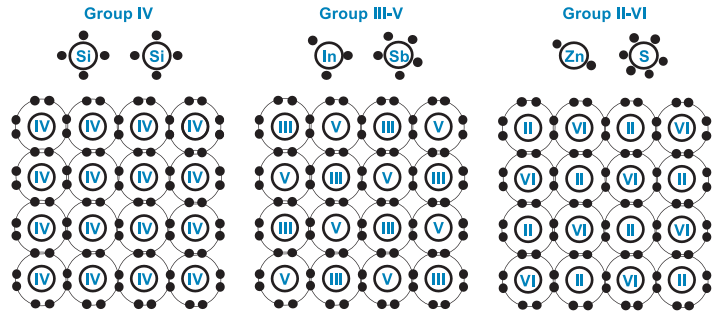
Photoconductors for BLIP and Johnson-limited conditions are defined in the table.

| BLIP   | JOLI  |
|--|---|
| $NEP_{PC,BLIP} = \frac{2hc}{\lambda G} \sqrt{\frac{E_{bkg} A_d \Delta f}{\eta}}$ | $NEP_{PC,JOLI} \equiv \frac{i_j}{\mathcal{R}_{i,PC}} \equiv \frac{\sqrt{4k\Delta f T / R_{eq}}}{\frac{\lambda q \eta G}{hc}}$ |
| $D_{PC,BLIP}^* = \frac{\lambda}{2hc} G \sqrt{\frac{\eta}{E_{bkg}}}$              | $D_{PC,JOLI}^* = \frac{\lambda q \eta}{2hc} G \sqrt{\frac{R_{eq} A_d}{kT}}$   |
| where:<br>$T \equiv T_d \approx T_L$ and $R_{eq} = R_d    R_L$                   |   |

For a given photon flux and a photoconductive gain of unity, the generation–recombination noise is larger than the shot noise by a factor of  $\sqrt{2}$ .

## Infrared Semiconductor Material Groups

**Semiconductors** are crystals created by covalent and ionic atomic bonds, through which the valence band of the atom is filled with eight electrons by means of sharing the electrons with its four neighboring atoms. These alloys might use atoms of a single species from group IV, or other materials composed of two atoms, one from group  $M < 4$ , while the other from  $N > 4$ , so  $M + N = 8$  electrons (i.e., the octet chemical rule).



Optoelectronics has taken advantage of these compounds to form ternary semiconductors of the form  $(A_xA'_{1-x})B$  or  $A(B_xB'_{1-x})$ , and quaternary semiconductors of the form  $(A_xA'_{1-x})(B_yB'_{1-y})$ .

Their alloy compositions ( $0 < x < 1$ ;  $0 < y < 1$ ) allow for the cutoff wavelength (and thus the bandgap) to be adjusted.

| Families of Semiconductor Materials        |                           |                            |                           |                           |                           |                            |                           |                          |                           |                          |                         |                          |                          |                           |                           |                         |                        | 19                       |                          |                            |                           |                               |                           |                            |                            |                            |                           |                           |                             |                              |                         |                             |                             |                            |                           |
|--|---------------------------|----------------------------|---------------------------|---------------------------|---------------------------|----------------------------|---------------------------|--------------------------|---------------------------|--------------------------|-------------------------|--------------------------|--------------------------|---------------------------|---------------------------|-------------------------|------------------------|--------------------------|--------------------------|----------------------------|---------------------------|-------------------------------|---------------------------|----------------------------|----------------------------|----------------------------|---------------------------|---------------------------|-----------------------------|------------------------------|-------------------------|-----------------------------|-----------------------------|----------------------------|---------------------------|
| IV-IV: Si, Ge, Pb                          |                           |                            |                           |                           |                           |                            |                           |                          |                           |                          |                         |                          |                          |                           |                           |                         |                        | He                       |                          |                            |                           |                               |                           |                            |                            |                            |                           |                           |                             |                              |                         |                             |                             |                            |                           |
| III-V: InSb, InAs, AlGaAs, InGaAs, InGaAsP |                           |                            |                           |                           |                           |                            |                           |                          |                           |                          |                         |                          |                          |                           |                           |                         |                        | He                       |                          |                            |                           |                               |                           |                            |                            |                            |                           |                           |                             |                              |                         |                             |                             |                            |                           |
| II-VI: ZnSe, ZnS, CdSe, HgCdTe, CdZnTe     |                           |                            |                           |                           |                           |                            |                           |                          |                           |                          |                         |                          |                          |                           |                           |                         |                        | He                       |                          |                            |                           |                               |                           |                            |                            |                            |                           |                           |                             |                              |                         |                             |                             |                            |                           |
| I  | 2                         |                            |                           |                           |                           |                            |                           |                          |                           |                          |                         | III                      | IV                       | V                         | VI                        | 17                      | 18                     |                          |                          |                            |                           |                               |                           |                            |                            |                            |                           |                           |                             |                              |                         |                             |                             |                            |                           |
| H<br>hydrogen<br>1.00794                   | He<br>helium<br>4.00260   |                            |                           |                           |                           |                            |                           |                          |                           |                          |                         | B<br>boron<br>10.811     | C<br>carbon<br>12.011    | N<br>nitrogen<br>14.007   | O<br>oxygen<br>15.999     | F<br>fluorine<br>18.998 | Ne<br>neon<br>20.180   |                          |                          |                            |                           |                               |                           |                            |                            |                            |                           |                           |                             |                              |                         |                             |                             |                            |                           |
| Li<br>lithium<br>6.941                     | Be<br>beryllium<br>9.012  |                            |                           |                           |                           |                            |                           |                          |                           |                          |                         | Al<br>aluminum<br>26.982 | Si<br>silicon<br>28.086  | P<br>phosphorus<br>30.974 | S<br>sulfur<br>32.06      | Cl<br>chlorine<br>35.45 | Ar<br>argon<br>39.948  |                          |                          |                            |                           |                               |                           |                            |                            |                            |                           |                           |                             |                              |                         |                             |                             |                            |                           |
| Na<br>sodium<br>22.990                     | Mg<br>magnesium<br>24.305 | Al<br>aluminum<br>26.982   | Si<br>silicon<br>28.086   | P<br>phosphorus<br>30.974 | S<br>sulfur<br>32.06      | Cl<br>chlorine<br>35.45    | Ar<br>argon<br>39.948     | K<br>potassium<br>39.098 | Ca<br>calcium<br>40.078   | Sc<br>scandium<br>44.956 | Ti<br>titanium<br>47.88 | V<br>vanadium<br>50.942  | Cr<br>chromium<br>52.00  | Mn<br>manganese<br>54.938 | Fe<br>iron<br>55.845      | Co<br>cobalt<br>58.933  | Ni<br>nickel<br>58.69  | Cu<br>copper<br>63.546   | Zn<br>zinc<br>65.38      | Ga<br>gallium<br>69.723    | Ge<br>germanium<br>72.64  | As<br>arsenic<br>74.922       | Se<br>selenium<br>78.96   | Br<br>bromine<br>79.904    | Kr<br>krypton<br>83.80     |                            |                           |                           |                             |                              |                         |                             |                             |                            |                           |
| K<br>potassium<br>39.098                   | Ca<br>calcium<br>40.078   | Sc<br>scandium<br>44.956   | Ti<br>titanium<br>47.88   | V<br>vanadium<br>50.942   | Cr<br>chromium<br>52.00   | Mn<br>manganese<br>54.938  | Fe<br>iron<br>55.845      | Co<br>cobalt<br>58.933   | Ni<br>nickel<br>58.69     | Cu<br>copper<br>63.546   | Zn<br>zinc<br>65.38     | Ga<br>gallium<br>69.723  | Ge<br>germanium<br>72.64 | As<br>arsenic<br>74.922   | Se<br>selenium<br>78.96   | Br<br>bromine<br>79.904 | Kr<br>krypton<br>83.80 | Rb<br>rubidium<br>85.468 | Sr<br>strontium<br>87.62 | Y<br>yttrium<br>88.906     | Zr<br>zirconium<br>91.224 | Nb<br>niobium<br>92.906       | Mo<br>molybdenum<br>95.94 | Tc<br>technetium<br>98.906 | Ru<br>ruthenium<br>101.07  | Rh<br>rhodium<br>102.91    | Pd<br>palladium<br>106.42 | Ag<br>silver<br>107.87    | Cd<br>cadmium<br>112.41     | In<br>indium<br>114.82       | Sn<br>tin<br>118.71     | Sb<br>antimony<br>121.76    | Te<br>tellurium<br>127.60   | I<br>iodine<br>126.905     | Xe<br>xenon<br>131.29     |
| Rb<br>rubidium<br>85.468                   | Sr<br>strontium<br>87.62  | Y<br>yttrium<br>88.906     | Zr<br>zirconium<br>91.224 | Nb<br>niobium<br>92.906   | Mo<br>molybdenum<br>95.94 | Tc<br>technetium<br>98.906 | Ru<br>ruthenium<br>101.07 | Rh<br>rhodium<br>102.91  | Pd<br>palladium<br>106.42 | Ag<br>silver<br>107.87   | Cd<br>cadmium<br>112.41 | In<br>indium<br>114.82   | Sn<br>tin<br>118.71      | Sb<br>antimony<br>121.76  | Te<br>tellurium<br>127.60 | I<br>iodine<br>126.905  | Xe<br>xenon<br>131.29  | Cs<br>cesium<br>132.91   | Ba<br>barium<br>137.33   | La<br>lanthanum<br>138.905 | Hf<br>hafnium<br>178.49   | Ta<br>tantalum<br>180.948     | W<br>tungsten<br>183.84   | Re<br>rhenium<br>186.207   | Os<br>osmium<br>190.23     | Ir<br>iridium<br>192.222   | Pt<br>platinum<br>195.084 | Au<br>gold<br>196.967     | Hg<br>mercury<br>200.59     | Tl<br>thallium<br>204.38     | Pb<br>lead<br>207.2     | Bi<br>bismuth<br>208.98     | Po<br>polonium<br>209       | At<br>astatine<br>210      | Rn<br>radon<br>222        |
| Cs<br>cesium<br>132.91                     | Ba<br>barium<br>137.33    | La<br>lanthanum<br>138.905 | Hf<br>hafnium<br>178.49   | Ta<br>tantalum<br>180.948 | W<br>tungsten<br>183.84   | Re<br>rhenium<br>186.207   | Os<br>osmium<br>190.23    | Ir<br>iridium<br>192.222 | Pt<br>platinum<br>195.084 | Au<br>gold<br>196.967    | Hg<br>mercury<br>200.59 | Tl<br>thallium<br>204.38 | Pb<br>lead<br>207.2      | Bi<br>bismuth<br>208.98   | Po<br>polonium<br>209     | At<br>astatine<br>210   | Rn<br>radon<br>222     | Fr<br>francium<br>223    | Ra<br>radium<br>226      | Ac<br>actinium<br>227      | Th<br>thorium<br>232.038  | Pa<br>protactinium<br>231.036 | U<br>uranium<br>238.029   | Np<br>neptunium<br>237.048 | Pu<br>plutonium<br>244.064 | Am<br>americium<br>243.061 | Cm<br>curium<br>247.07    | Bk<br>berkelium<br>247.07 | Cf<br>californium<br>251.08 | Es<br>einsteinium<br>252.083 | Fm<br>fermium<br>257.10 | Mn<br>mendelevium<br>258.10 | Lv<br>livermorium<br>260.10 | Ts<br>tennessine<br>289.10 | Og<br>oganesson<br>289.10 |

There is a trend in the change of chemical bonds—from the all-covalent group IV to the mostly covalent, partially ionic, group III-V to the partially covalent, mostly ionic, group II-VI. High-performance heterostructures are required to be microelectronic and must have strong optical absorption.



## Third-Generation Infrared Imagers: Requirements

---

Third-generation **infrared focal plane arrays (IRFPAs)** are being actively developed by the U.S. Department of Defense (DoD). The proliferation of second-generation cooled and uncooled IRFPAs threatens to nullify the advantage that U.S. soldiers have in night combat. Third-generation FPA technology is being defined and developed to maintain this current advantage enjoyed by U.S. and allied armed forces.

This new generation of IRFPA technology should have some, or all, of the following capabilities:

- Ability to achieve sensitivity improvements corresponding to **noise-equivalent temperature difference (NETD)** single-digit values;
- Large and multicolor FPA formats with high-spatial-resolution cooled imagers in order to improve global system performance;
- High-performance multispectral and hyperspectral cooled detectors with the ability of each pixel to detect two or more infrared spectral bands;
- Thermal performance improvements of the cryogenic technologies in order to improve thermal resolution;
- Fast-frame-rate operation to provide more data throughput for advanced signal-processing functions such as automatic target recognition (ATR), missile projectile tracking, and collection of a high percentage of available signals;
- Reduction of power dissipation as well as power consumption of cryogenic coolers;
- 3D active imagery with high-speed detectors and low noise to improve identification range and efficiency;
- **Higher operating temperature (HOT)** to reduce cryogenics constraints and to improve reliability driven by **size, weight, power, and cost (SWaP+C)**;
- Smart **read-out integrated circuits (ROICs)**;
- Medium-high-performance uncooled imagers with small pixels and power reduction;
- Small pixels enabling high-density sensors in small packages; IRFPA smaller than a dime; and
- Very low-cost, expendable uncooled imagers (optics, electronic packaging, and communications link).

### Third-Generation Infrared Imagers: Challenges

---

The charge capacity of the read out, the **integration time** linked to the frame time, and the **dark current** of the semiconductor material are the major issues limiting the performance of third-generation IRFPAs. The **charge well capacity** is the maximum amount of charge that can be stored on the storage capacitor of each unit cell. The size of the unit cell is limited to the dimensions of the detector element in the array. At high background and long integration times, the capacitor well is easily saturated. Since the noise-equivalent bandwidth is inversely proportional to the integration time, shorter integration times result in extra noise in the integration process. Furthermore, as imaging IRFPAs grow in detector number of pixels for high-resolution densities, so do the system requirements for the embedded digital image processing.

The **uniformity** affects the infrared system complexity as well. It also verifies that every sensor pixel of the IRFPA produces the same output when given an even stimulation. Uniformity is important for accurate temperature measurements, background subtraction, and threshold testing, which are inherent in the detection and identification of targets. Non-uniformities compel the electronics to use additional analog-to-digital bits, thus reducing the system's dynamic range, and require the development of compensation algorithms to correct the image.

The NETD is inversely proportional to the normalized detectivity  $D^*$ . However, when  $D^*$  exceeds values greater than  $10^{10}$  Jones, the IRFPA performance becomes independent of  $D^*$  prior to the **non-uniformity correction (NUC)**. For example, improving the non-uniformity from 0.1% to 0.01% could improve the thermal sensitivity of a thermal imaging system operating in BLIP conditions by an order of magnitude.

ROIC capabilities may be enhanced through the use of advanced wafer-level processes. One approach is to build stacks of multiple vertically integrated layers of silicon circuitry interconnected beneath the IRFPA (i.e., 3D ROICs).

### Third-Generation Infrared Imagers: Challenges (cont.)

---

Fast frame rates produce additional power dissipation on the ROIC, thus increasing the power consumption of the **integrated dewar cooler assembly (IDCA)**. One way to reduce the read-out power is to digitize the analog signals on chip and use laser diodes as multiplexing devices. Moreover, a level of 15–18 bits in the analog-to-digital circuitry is necessary to handle the dynamic range between the noise floor and signal levels.

Other challenges in small-pixel FPAs include achieving high-yield detector-to-ROIC integration techniques, pixel transimpedance gains that allow BLIP conditions, and the development of low-leakage infrared photodetectors.

Small pixels in uncooled detector FPAs pose different types of challenges. The design of microbolometers requires a significant decrease in thermal conductivity to maintain a feasible thermal response time. Deep-ultraviolet lithographic processes with fine linewidths  $<0.25\ \mu\text{m}$  are required to decrease the width and thickness of the structural legs. Thinner bridge and umbrella structures are also necessary to reduce thermal mass without sacrificing absorption efficiency. Due to the current practical limitations and acceptable cost of lithographic tools available to manufacture thermally isolated bridge structures, the thermal conductance of microbolometer devices is still larger than the thermal radiation among the small pixels. As a result, uncooled technology remains far from the performance limits at which cooled FPAs operate. Cost reduction is still one of the main drivers in the development of expendable uncooled infrared imagers.

Small pixel arrays improve the spatial resolution and are better able to oversample an image. This diminution in aliasing enables a thermal sensor to better discriminate between real targets and noise artifacts. The reduction in sensitivity may be compensated by the use of low- $F/\#$  optics. The reduced dynamic range can be extended by further reducing the noise floor, implementing ferroelectric capacitors into standard CMOS foundries, oversampling, change skimming, etc.

## Indium Antimonite (InSb) Photodiodes

**Indium antimonite (InSb)** is a crystalline compound made from the elements indium and antimony. It is a narrow-gap intrinsic III-V semiconductor detector material with a direct bandgap.

The relationship between the energy gap and operating temperature from 4 K to 300 K is given by

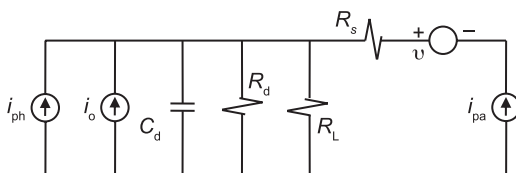
$$\mathcal{E}_{\text{gap}}(x) = 0.233 - (6.498 \times 10^{-5})T - (5.0826 \times 10^{-7})T^2$$

and its current–voltage characteristics are described by

$$i = i_o[\exp(qv/kT) - 1] - i_{\text{ph}} + \frac{v}{R_s}$$

where  $R_s$  represents a shunt resistance of a leakage current path in the p-n junction, and  $i_{\text{ph}}$  is the photo-generated current.

The diode equivalent circuit with simplified preamplifier and noise sources is depicted below.



InSb FPAs are highly uniform, multichannel imaging devices that provide sensitive detection at 1–5.3  $\mu\text{m}$  (80 K). These imaging devices have very high external quantum efficiencies (i.e.,  $\eta > 90\%$  for device thicknesses of 5–10  $\mu\text{m}$ ), while operabilities exceeding 99.5% are routine. Large-format resolutions are commercially available.

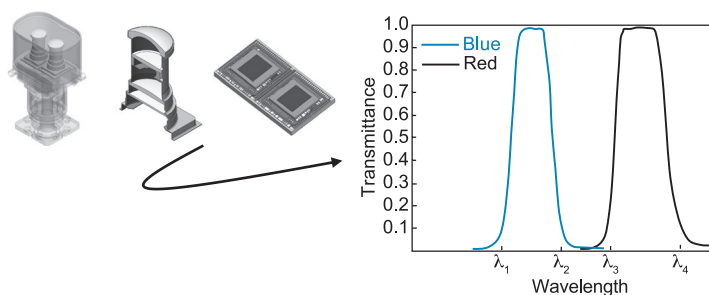
The spectral response in these types of devices shifts to longer wavelengths with increasing temperature. Their thermionic noise also increases rapidly with temperature.

Distinct advantages to advanced digital FPA technology include low-noise data output and immunity to external noise sources for **non-uniformity correction (NUC)** stability, high-speed digital data output, and virtually no crosstalk.

## InSb Dual-Band Integrated Dewar Cooler Assembly

Many of the missile applications in the MWIR spectral region require the use of two-color spectral wavebands to discriminate the missile infrared signature from the background.

InSb photodiodes are simple binary compounds with a fixed bandgap and are not suitable for multiband operations. In order to employ these photodevices in this type of high-sensitivity multicolor application, they require the incorporation of cold color filters to select the bands of interest, commonly known as blue (shorter) and red (longer) spectral wavebands. Two FPAs must be operated simultaneously at high frame rates in an **IDCA** to optimize both spectral bands [images are from Dhar, Dat, and Sood (2013.)]



Some important facts concerning **InSb photodiodes** are:

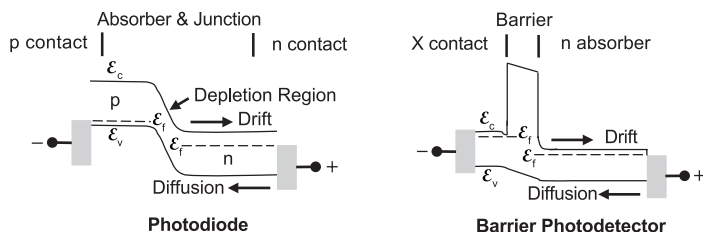
- They are the only relevant binary compound.
- Their composition cannot be tuned.
- They have a well-characterized and mature, direct-bandgap material with low defects.
- They have superior uniformity.
- Fabrication of large FPAs is easy.
- They have high quantum efficiency.
- They have excellent MWIR BLIP performance at 77 K.
- The dark current is dominated by Shockley–Read–Hall (SRH) centers.
- Passivation is required to protect the device against undesired environmental effects and to reduce the surface leakage current. Native oxides or other insulators are used for the passivation process, which is time consuming and hence undesirable.

## Concept of Barrier Infrared Photodetectors

A conventional photodiode operating in reverse bias incorporates a **depletion region (barrier)** to the flow of majority charge carriers across the p-n junction. However, minority carriers that happen to move near the junction are swept across. The dark current in these types of photodevices increases exponentially with temperature. Under BLIP conditions, this noise is mainly produced by **generation-recombination (G/R) centers**, also known as **Shockley-Read-Hall (SRH)** traps in the depletion region of the photodiode.

SRH noise processes are extrinsic, and they use energy levels within the bandgap resulting from impurities and material defects. Electrons and holes may be captured and emitted from these traps, which impacts lifetimes of the excess carrier.

Barrier photodetectors are heterostructure devices that incorporate a design with a unipolar barrier. This barrier architecture blocks the majority carriers but allows the unimpeded flow of minority carriers. It is created by adjusting the bandgap of the different semiconductor materials.

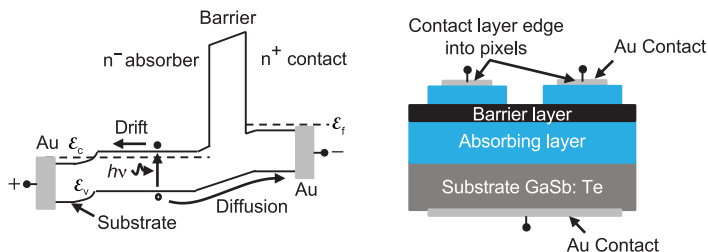


Barrier detectors can be divided in two groups:  $\text{XB}_n\text{n}$  and  $\text{XB}_p\text{p}$ , where X stands for either an n- or a p-type contact layer. In a  $\text{nBn}$  photodetector, all layers have the same n-type structural unit. This eliminates the need for a p-n junction as well as the excess dark current from the depletion zone.

**Barrier photodetectors** offer the temperature and wavelength flexibility of  $\text{HgCdTe}$ , along with the array size, uniformity, and high operability of  $\text{InSb}$  photodiodes.

## MWIR nBn Photodetector

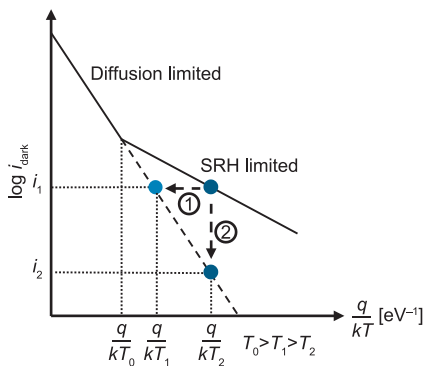
The name of the MWIR **nBn** heterostructure derives from the n-type absorption layer, the barrier layer, and the n-type contact layer.



The  $n^-/n^+$  type and barrier layers are ternary compositions of  $\text{AlSb}_{1-x}\text{As}_x$  and  $\text{InAs}_{1-y}\text{Sb}_y$ , respectively. Both the zero-valence-band and the large-conduction-band energy discontinuities are achieved by adjusting the allowed compositions of  $x$  and  $y$ .

When the top layer is etched into pixels, the wide-bandgap barrier eliminates surface leakage.

The nBn architecture operates like a p-i-n photodiode but with lower dark current. The reason for this decrease in noise is the absence of a depletion layer. By removing the SRH current noise source, nBn detectors ideally operate with superior performance compared to standard photodiodes at the same operating temperature, or with similar performance at higher operating temperatures. This effect can be seen in the **Arrhenius plot** below.



$T_0$  is defined as the cross-over temperature at which the diffusion and G/R currents are equal.

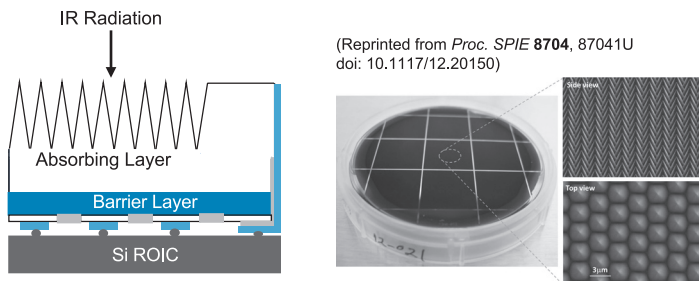
1. nBn photodetectors operate at higher temperature  $T_1$  than photodiodes with the same dark current.

## MWIR nBn Photodetector (cont.)

2. nBn devices exhibit better SNR than photodiodes operating at the same temperature  $T_2$ .

nBn's high operating temperature, simple structure, and mature III-V material growth translate into a 4–6 $\times$  reduction in SWaP, reliability, schedule, and cost. The poorest-performance devices are able to achieve BLIP conditions with **high operating temperatures (HOT)** (i.e.,  $\geq 150$  K), which induces less internal stress in the **IDCA**, thus allowing for production of larger formats and smaller pixels with lower risk. In addition, nBn photodetectors can offer multicolor MWIR FPAs.

**nCBn (compound barrier)** detector architectures are designed to achieve high quantum efficiencies over broad spectral wavebands with HOT. Each detector pixel has an array of multiple pyramid-shaped absorbers that enhance photon trapping for high absorptance of the incident light.



The pyramid base width and height as well as the spacing between the pyramids are optimized to minimize the front-side reflection. Photon absorption could be further enhanced if a backside reflector were to be implanted beneath the absorbing slab.

Problems that remain with the nBn structure are related to the lack of basic understanding of what is happening at the interface of the different layers. Developing empirical models will increase the understanding of the nBn photodetector technology. This will result in detailed growth procedures and device characterization of InAsSb/AlSbAs photodetectors, as well as faster processes for attaining nBn structures using alternative semiconductor materials.



## Mercury Cadmium Telluride (HgCdTe) Photodetectors

---

**Mercury cadmium telluride (HgCdTe)** photodetectors are intrinsic PC and PV devices. The PC HgCdTe detector is a mature product that has been in production for many years. It is typically fabricated from n-type material with a high intrinsic concentration of carriers, which can achieve background-limited sensitivities at operating temperatures substantially higher than extrinsic detectors. Even though HgCdTe PC detectors are excellent single-element sensor devices, they are not conducive to producing 2D FPAs. Producing two identical HgCdTe PC detectors is rather difficult because of the material's non-uniformity. In addition, their large current densities (i.e., low resistance) can lead to overheating problems, and their potential wells fill too quickly because of background currents. HgCdTe photodiodes also have difficulties associated with producing homogeneous material. However, modern fabrication methods can be applied to produce device-quality PV superlattice structures consisting of thin CdTe/HgTe stacked layers. This approach controls and improves the non-uniformity of the photodiodes and reduces the  $1/f$  noise contributions of the detector FPAs.

$\text{Hg}_{1-x}\text{Cd}_x\text{Te}$  is a ternary semiconductor compound that exhibits a wavelength cutoff proportional to the alloy composition (or molar fraction ratio  $x$  of Cd to Hg). Pure CdTe ( $x = 1$ ) will detect radiation wavelengths out to  $\sim 0.83 \mu\text{m}$ ; the greater the percentage of Hg the longer the wavelength response. HgCdTe photodiodes can operate up to  $13 \mu\text{m}$ , while HgCdTe PC detectors can be tailored to operate farther in the infrared to about  $30 \mu\text{m}$ .

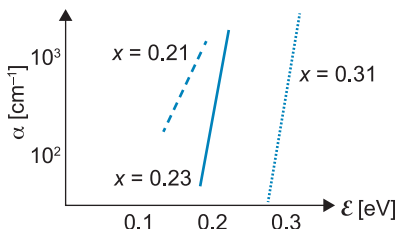
An empirical expression that relates the bandgap energy  $\mathcal{E}_{\text{gap}}$ , the temperature  $T$ , and the alloy composition  $x$  is given by

$$\mathcal{E}_{\text{gap}}(x) = -0.302 + 1.93x + (5.35 \times 10^{-4})T(1 - 2x) - 0.801x^2 + 0.832x^3$$

This equation is almost linear for molar values in the range of  $0.2 \leq x \leq 0.6$  and fits  $\mathcal{E}_{\text{gap}}$  data for the temperature range  $4.2 \text{ K} \leq T \leq 300 \text{ K}$ .

## Control of the Alloy Composition

The optical **absorption coefficient**  $\alpha$  of HgCdTe ranges from  $10^2$  to  $10^5 \text{ cm}^{-1}$ , so virtually all photons are absorbed within  $10 \text{ }\mu\text{m}$  of the incident surface, which means that the detector thickness can be much less than the thickness required of other detector materials for similar wavelengths. For example, a plot of  $\alpha$  vs. photon energy for  $x = 0.21$ ,  $0.23$ , and  $0.31$  is shown. The steepness of this curve leads to a rapid decline in detectivity for wavelengths larger than the cutoff wavelength.



The downside of this steep variability is that the **molar fraction**  $x$  is not well controlled in fabrication, so the alloy composition and cutoff wavelength must be determined by infrared transmission maps at a temperature of  $300 \text{ K}$ , usually at several points on the wafer. The fact that  $x$  is not able to be tightly controlled leads to a non-uniform material; therefore, both the responsivity and cutoff wavelength can vary as a function of  $x$ .

The variation of  $x$  is related to the cutoff wavelength by

$$\lambda_{\text{cutoff}} = \frac{1.24}{\mathcal{E}_{\text{gap}}(x)}$$

$$\lambda_{\text{cutoff}} = \frac{1}{-0.2435 + 1.5565x + (4.3145 \times 10^{-4})T(1 - 2x) - 0.646x^2 + 0.671x^3}$$

To determine the impact of the uncertainty of  $x$  in manufacturing on variations in  $\lambda_{\text{cutoff}}$ , we take the differential, yielding

$$\frac{\partial \lambda_{\text{cutoff}}}{\lambda_{\text{cutoff}}^2} = (1.5565 - 8.629 \times 10^{-4}T - 1.292x + 2.013x^2)\partial x$$

This variation in  $x$  is typical of good-quality HgCdTe material. The variation in cutoff wavelength is negligible for SW/MWIR spectral bands; however, in the LWIR, the uncertainty is quite large and cannot be neglected. This variation causes radiometric calibration issues, in which the radiation is sensed over a different spectral region.

## HgCdTe Photodiodes and FPAs

An uncertainty in cutoff wavelength for  $\partial x = 0.2\%$  is shown in the table below.

| $x$   | $\lambda_{\text{cutoff}} [\mu\text{m}] @ 77 \text{ K}$ | $\partial\lambda_{\text{cutoff}} [\mu\text{m}]$ |
|-------|--|---|
| 0.395 | 3  | 0.023   |
| 0.295 | 5  | 0.064   |
| 0.21  | 10   | 0.26  |
| 0.196 | 14   | 0.51  |

Integrating the exitance of a blackbody at temperature  $T$  for  $x = 0.196$  from 0 to  $13.5 \mu\text{m}$  will yield the same response as integrating from 0 to  $14 \mu\text{m}$  of a source at temperature  $T - \Delta T$ . Therefore, if a FPA is manufactured, a different output voltage for a uniform background would appear due to the non-uniformities of the semiconductor.

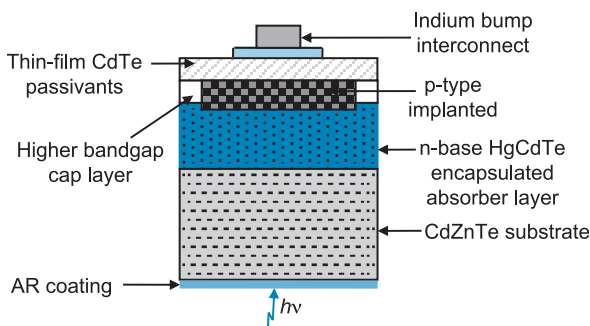
HgCdTe FPAs are made up of two components: an HgCdTe detector array and a silicon ROIC multiplexer. The ROIC reads the photocurrent from each pixel of the detector FPA and outputs the signal in a desired sequence that is used to form the 2D image.

The highest detector performance is achieved by growing HgCdTe on lattice-matched substrate CdZnTe. The coefficient of thermal expansion (CTE) mismatch between CdZnTe and Si affects the size of the FPA and its reliability during repeated thermal cycling from room temperature to cryogenic operating temperatures. This temperature-cycling fatigue is addressed by using a shim between the Si and the dewar cold plate, thus constraining the detector array and the ROIC to expand and contract at the same rate during thermal cycling. HgCdTe growth on alternative substrates such as silicon and sapphire are also being developed to reduce this thermal expansion mismatch. These alternative substrate materials suffer from a large lattice mismatch with HgCdTe, leading to a higher defect density and consequently reducing the detector performance. As a result, the tradeoff between FPA performance, size, and cost dictates the selection of the substrate material.

The fabrication of HgCdTe photodiodes is usually based on DLHJ, TLHJ, and HDVIP technologies, defined next.

## Double-Layer Heterostructure Junction Photodiodes

The **double-layer heterostructure junction (DLHJ)** photodiode fabrication process starts with *in situ* molecular beam epitaxy (MBE) growth of a double-layer heterostructure consisting of an absorbing base layer and a higher-bandgap cap layer. The formation of p-on-n photodiodes is achieved by selective-area p-type arsenic (As) ion implantation through the cap layer into the narrow-gap base layer. Each implanted area defines an individual pixel of the detector array. The implantation step is followed by a two-step thermal anneal under a Hg overpressure. A high-temperature anneal in Hg vapor activates the dopant by substituting arsenic atoms on the Te sub-lattice. A lower-temperature anneal is performed immediately after the high-temperature anneal, annihilating the Hg vacancies formed in the HgCdTe lattice during growth and the high-temperature annealing step. Individual photodiodes are delineated by a mesa etch through the thin cap layer. The exposed surface is then passivated, and metal contacts and metal interconnect bumps are formed. The thin polycrystalline MBE-deposited CdTe layer provides the device passivation, which reduces surface recombination as well as  $1/f$  noise and renders the surface impermeable to environmental conditions.

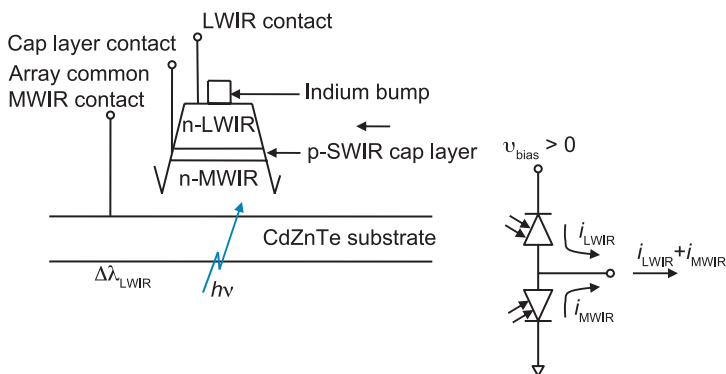


The goal is to have the p-type cap layer thin enough and of sufficiently wide bandgap that it contributes a negligible amount of thermally generated diffusion current compared to that from the n-type encapsulated absorber layer.

## Dual-Band HgCdTe FPAs

Multicolor third-generation IRFPAs are desirable for numerous applications. For example, by using two infrared wavebands, spurious information such as background clutter and sun glint may be subtracted from an infrared image, leaving only the targets of interest. Thus, the effective SNR of two-color IRFPAs exceeds that of single-color IRFPAs for specific targets.

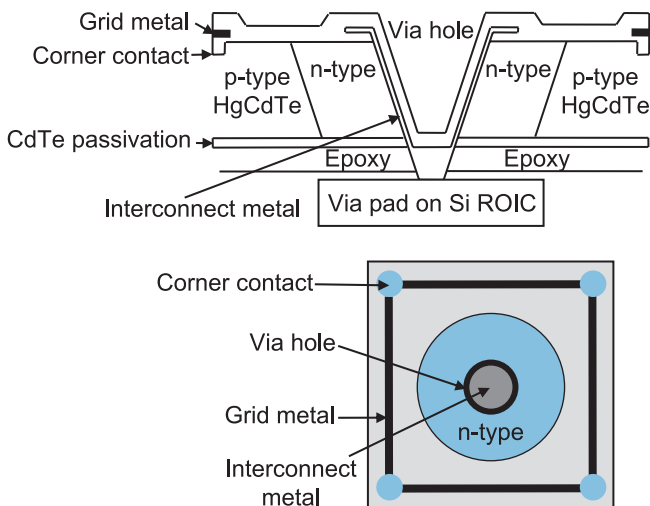
Two-color detector arrays are usually based on an n-p-n HgCdTe **triple-layer heterostructure junction (TLHJ)** design. TLHJ detectors consist of back-to-back photo-diode p-n junctions. This device architecture is realized by placing a longer-wavelength HgCdTe photodiode behind a shorter-wavelength photodiode. An additional electrical contact to the shared-type centered layer is employed so that each junction can be accessed independently with both signal channels integrated simultaneously.



High-quality MWIR/LWIR IRFPAs for third-generation systems have been fabricated from MBE-grown HgCdTe TLHJ wafers with 100% optical fill factor and high frame rate. These devices contain cutoff wavelengths greater than  $10.5 \mu\text{m}$  at 77 K. They provide simultaneous temporal detection in the MWIR and LWIR bands using time-division-multiplexed integration (TDMI) incorporated into the ROIC. They have operability of  $>99.9\%$  and  $>98\%$  in the midwave and longwave spectral bands, respectively.

## High-Density Vertically Integrated Photodiodes

The **high-density vertically integrated photodiode (HDVIP)** consists of a thin layer of extrinsically doped p-HgCdTe, passivated on both surfaces with an interdiffused layer of CdTe, which is glued to an underlying silicon ROIC with a uniformly thin bond-line of epoxy. The stress in the HgCdTe is uniform throughout the whole layer except for a small region around the periphery about the size of a layer thickness. Contact to the silicon ROIC is achieved by etching a via hole through the HgCdTe down to landing pads on the silicon. The  $n^+/n^-$  region of the diode is formed around the via hole by both the etching process itself and a subsequent ion-implant step. The other notable feature of this architecture technology is the  $p^+/p$  non-injecting contact that is formed in each unit cell of the FPA. These contacts are joined electrically by a top surface metal grid, which results in negligible de-biasing across a large area array, even at relatively high background flux currents. The fill factor of the unit cell is greater than 80%, with resulting unit cell collection efficiencies in excess of 60%.

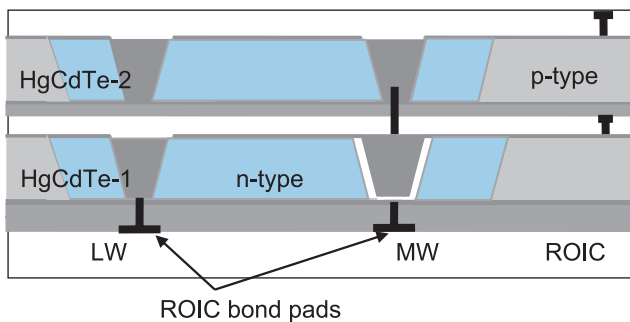


## High-Density Vertically Integrated Photodiodes (cont.)

Liquid phase epitaxy (LPE) is used to grow the material, resulting in inherently purer HgCdTe epitaxial layers; therefore, the depletion region presents fewer threading dislocations. Applying the hybridization technique to silicon renders the device immune to rapid thermal cycling. Furthermore, the photodiode is frontside illuminated, leading to high quantum efficiencies and near-theoretical MTF performance.

HDVIP technology is currently employed for production manufacturing of a wide variety of FPAs and detector-dewar cooler assemblies (DDCAs).

This technology has been extended to two colors by gluing two mono-color layers together into a composite and forming an insulated via hole through the lower layer in order to read out the upper color. This approach has been used to fabricate MW/MW and MW/LW FPAs with co-located and simultaneous read out of the two colors using existing ROICs. The two color signals are read out individually. This approach is readily adaptable to three or four colors.



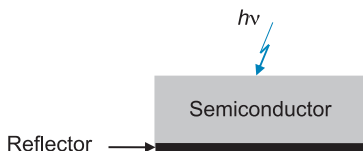
**Electron-injected avalanche photodiode (EAPD)** detectors are based on HDVIP architecture. This fairly new technology has been demonstrated to be one of the most promising paths to FPAs because of these detectors' exponential gains of 100–1000 for low values of reverse bias (5–10 V) and the high bandwidth associated with excess noise factors ( $f = \text{SNR}_{\text{in}}/\text{SNR}_{\text{out}}$ ) of 1.0–1.3.

## Uncooled HgCdTe Photodiodes

When operating at midwave and long-wave spectral bands, infrared photodetectors require cryogenic cooling to achieve useful performance. The need for cooling is a major limitation of these devices that prevents more widespread use of infrared technology. Thermal detectors operate at room temperature, but they cannot replace photon detectors in most applications due to their slow response and ineffectiveness in applications requiring multispectral detection.

There are some ways to improve the performance of photodetectors without cooling. One way is the suppression of the Auger generation–recombination process. The Auger recombination and its counterpart impact ionization. It involves two electrons and a heavy hole, which recombine in a band-to-band transition and give off the resulting excess kinetic energy to another electron–hole pair. A moderate p-type doping of the absorber region is widely used for some suppression of the Auger mechanism. Another way to improve the performance of uncooled infrared photon detectors is to reduce the physical volume of the semiconductor, thus reducing the amount of thermal generation. This must be done without decreasing the quantum efficiency, optical area, or FOV of the detector.

The thickness of the active region of the detector can be significantly reduced by enhancing the absorption of the radiation. This can be achieved by making use of multiple-pass radiation with a backside reflector. Even more efficient is the use of interference phenomena to set up a resonant cavity within the photodetector.



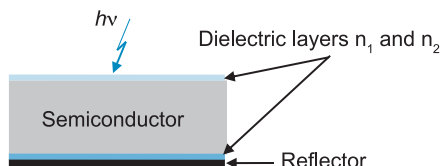
Interference occurs between the waves reflected at the rear and at the front surface of the semiconductor.



## Uncooled HgCdTe Photodiodes (cont.)

The thickness of the semiconductor is selected to set up the thermal standing waves in the structure with peaks at the front and nodes at the back surface. The quantum efficiency oscillates with the thickness of the structure, with the peaks at a thickness corresponding to an odd multiple of  $\lambda/4n$ , where  $n$  is the refractive index of the semiconductor.

Higher gain can be obtained in structures immersed between two dielectric layers and supplied with a backside reflector. The gain in quantum efficiency increases with  $n$ . Increased absorption allows for improved collection efficiency in photodiodes since the thickness can be smaller than the diffusion length.



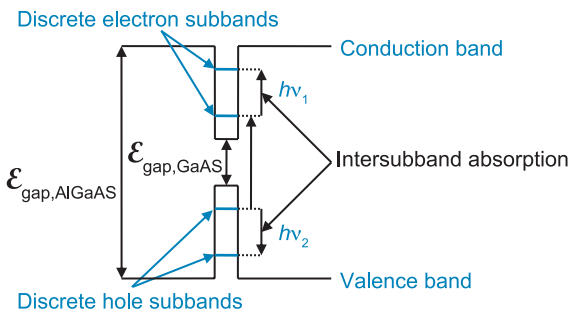
Interference effects modify the spectral response of the device; therefore, the gain within the optical cavity is achieved only in narrow spectral regions. Another limitation is that optical resonance occurs primarily for perpendicular incidence and is less effective for oblique incidence, thus limiting the use of these devices with fast optics.

Fundamental considerations dictate that HgCdTe is the optimal material for high-performance FPAs. The semiconductor's direct bandgap translates to high absorptive efficiency, and the material's composition can be tailored to absorb infrared radiation throughout the infrared spectral region. These attributes translate to flexibility and capability for BLIP detection. Unfortunately, insufficient demand to transition to high-rate production has led to difficulties in meeting the ultimate limit of HgCdTe detectors. Nevertheless, the fundamental performance limits of HgCdTe photodiodes have not been reached yet. Continued development of the *in situ* epitaxial techniques will allow bandgap-engineered devices of increasing quality and complexity.

## Quantum Well Infrared Photodetectors

**Quantum wells (QWs)** are potential wells that confine particles that were originally free to move in three dimensions to two dimensions, forcing them to occupy a planar region. **Quantum well infrared photodetectors (QWIPs)** are infrared photodetectors made from semiconductor materials that contain one or more QWs. QWIP development is showing that the bulk of semiconductors addressing the 8- to 14- $\mu\text{m}$  spectral region (mainly HgCdTe) have a number of disadvantages in terms of fabrication and non-uniformity. Detection at these long wavelengths requires materials with small bandgaps, which are often difficult to grow and process. QWIP technology is based on large-bandgap III-V semiconductor materials such as **GaAs**, which is simpler than HgCdTe, leading to high uniformity and reproducibility, as well as low-cost photodetectors.

QWs are formed in semiconductors by having a material such as GaAs sandwiched between two layers of a material with a wider bandgap, like **AlGaAs**. These structures can be grown by molecular beam epitaxy (MBE) or chemical vapor deposition (CVD) with control of the layer thickness down to a monolayer ( $<10 \text{ \AA}$ ). QWIPs operate by the photo-excitation of carriers between the ground-state and first-excited-state subbands of a GaAs/AlGaAs QW.



**Multiple quantum wells (MQWs)** are engineered by placing as many as 50 alternating thin layers of two different, high-bandgap semiconductor materials. The bandgap discontinuity of these materials creates quantized intersubbands in the potential wells associated with conduction bands or valence bands.

## Quantum Well Infrared Photodetectors (cont.)

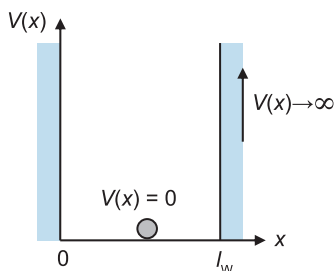
The position of these energy levels is established by adjusting the thickness and height of the QW. The design operating wavelength of intersubband photodetectors can be tailored from 3 to 20  $\mu\text{m}$ , offering great flexibility. The lattice-matched GaAs/ $\text{Al}_x\text{Ga}_{1-x}\text{As}$  detector material is an excellent choice for QW structures because the bandgap of  $\text{Al}_x\text{Ga}_{1-x}\text{As}$  can be changed continuously by varying the composition index or molar ratio  $x$  (and hence the height of the quantum well). QW structures are designed such that the photo-excited carriers can escape from the QW and be collected as photocurrent.

Unlike intrinsic photodetectors, which use interband transition, QWIPs must be extrinsic in order for the photon to have sufficient energy to create photocarriers (i.e.,  $h\nu > \mathcal{E}_{\text{gap}}$ ).

The effects of quantum confinement take place when the QW thickness approaches the **de Broglie wavelength**  $\Lambda$  of the carriers, leading to energy levels called **energy intersubbands** (i.e., the carriers can only have discrete energy values).  $\Lambda$  is defined as

$$\Lambda = \frac{h}{2\pi p}$$

where  $h$  is Planck's constant, and  $p$  is the momentum of the electron. The condition for a bound energy state is that  $\Lambda/2$  must be an integral multiple of the well width, and that the energy must be smaller than the energy-band offset.



A heterostructure such as a QW is equivalent to a single point particle in an immovable box that experiences zero potential energy. At the barriers of the well, the potential rises to infinity, thus constraining the particle to remain in the well.

## Quantum Well Infrared Photodetectors (cont.)

The quantum behavior (boundary conditions) within the well includes energy quantization and zero-point energy (i.e., lowest possible ground-state energy).

The idea of using multiple-quantum-well structures to detect IR radiation can be explained by using the basic principles of quantum mechanics and the Schrödinger equation. The time-independent Schrödinger equation for the particle inside the well [i.e.,  $V(x) = 0$ ] is given by

$$-\frac{\hbar^2}{8\pi^2 m_e^*} \frac{d^2\psi}{dx^2} = \mathcal{E}\psi$$

where  $m_e^*$  is the effective mass of an electron, and  $\psi$  is the eigenfunction of the system. The possible eigenfunctions and discrete energy levels for a QW with infinitely high barriers are obtained by solving the Schrodinger equation:

$$\psi_i = \sqrt{\frac{2}{l_w}} \sin\left(\frac{\pi x}{l_w} i\right) \quad \mathcal{E}_i = \frac{\hbar^2}{8m_e^* l_w^2} i^2$$

where  $i$  is an integer, and  $l_w$  is the width of the well. The intersubband transition between the ground-state energy level and the first excited state is

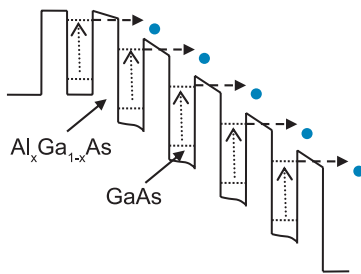
$$\Delta\mathcal{E} = \mathcal{E}_2 - \mathcal{E}_1 = \frac{3\hbar^2}{8m_e^* l_w^2}$$

The transition energy is inversely proportional to the square of the thickness of the well. The infinite potential-well wave solution gives us slightly higher energies than the energy levels of a finite potential well, but it is a good approximation to a more complex quantum problem.

When QWIPs are fabricated with thin barriers, the wavefunctions in neighboring wells overlap, causing energy-level perturbation and level shifting. The thin barriers allow tunneling of carriers between wells, providing a new degree of freedom in the materials' optical properties. QWIPs are photoconductors, and their performance depends for the most part on minimizing the dark current (i.e., tunneling leakage and thermionic emissions), as well as improving the quantum efficiency.

## Types of QWIPs

**Bound-to-bound (B-B)** QWIPs contain two bound states. The interaction of a photon of energy  $\mathcal{E}_2 - \mathcal{E}_1$  and an electron in the ground state causes a transition to the first excited state. The two processes critical to the operation of this device as an IR detector are intersubband absorption and tunneling. A bias voltage is applied across the device, changing the square wave potential to a stair-case-type potential. This external electric field lowers the barrier height enough that tunneling processes allow electrons to escape the well.

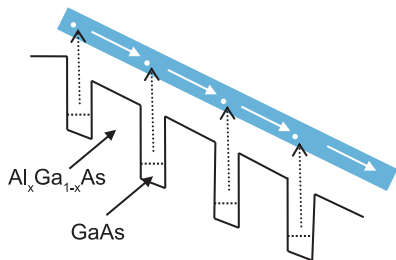


Once the electron has escaped the confines of the well, it accelerates toward the side with the applied voltage until it is captured by collision with a ground-state electron. The distance the electron travels before it collides with the other electron is called the transport length  $L_t$ . If the kinetic energy of the first electron is large enough, it can cause the transition of the other electron to its first excited state. This process repeated many times down the chain of wells will cause avalanche multiplication.

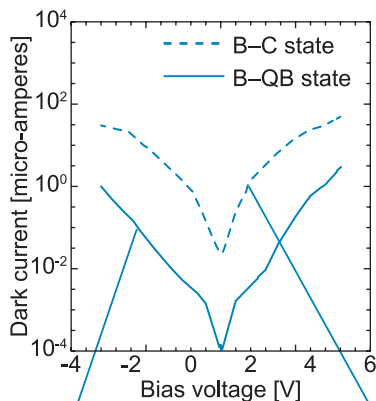
By reducing the width of the QW, it is possible to push the photo-excited carriers directly into the continuum, resulting in a strong **bound-to-continuum (B-C)** intersubband absorption. The major advantage of the B-C QWIP is that the photo-excited electrons can escape to the continuum transport without tunneling through the barrier. As a result, the bias required to efficiently collect photo-electrons can be decreased substantially, thus reducing the tunneling leakage dark current. In addition, the width of the AlGaAs barrier can be incremented without reducing the photo-electron collection, thus lowering the ground-state sequential tunneling by an order of magnitude.

### Types of QWIPs (cont.)

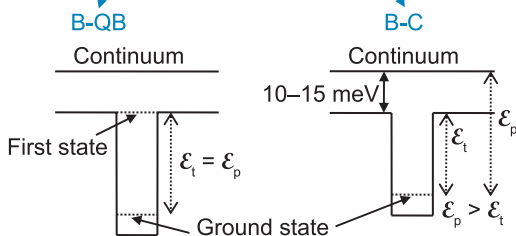
Nevertheless, for temperatures over 45 K, the overall dark current in this type of detector is quite high since it is dictated by thermionic emissions of ground-state electrons directly into the energy continuum. This thermionic leakage of dark current depends exponentially on the bias voltage and is governed by the Bose–Einstein probability distribution.



In **bound-to-quasi-bound (B-QB)** photodetectors, the design is engineered in such a way that the first excited energy state is exactly at the top of the well barriers of the QWs. Thermionic emissions dominate the production of dark currents within these longwave infrared devices. Dropping the first excited state to the quantum well top



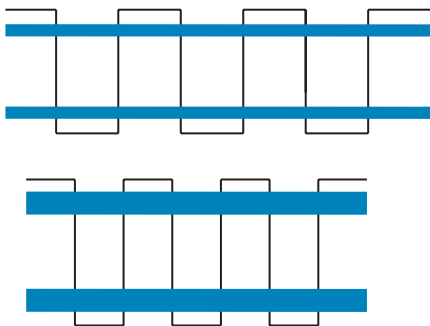
causes the energy barrier of thermionic emissions to be 10–15 meV higher than in the B-C state, thus reducing the dark current by an order of magnitude.



## Superlattices

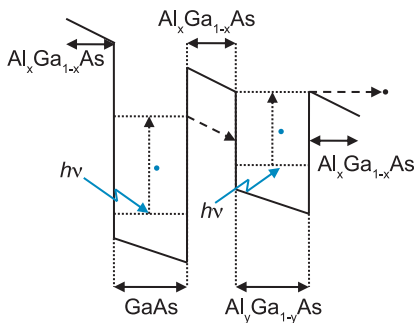
The wavefunctions decay exponentially within the barriers; however, if the barriers are thin enough (comparable to the de Broglie wavelength), perturbation will occur between the adjacent QWs.

This perturbation causes the energy levels in the well to split by means of selection rules into two levels ( $\mathcal{E}$  and  $\mathcal{E} + \Delta\mathcal{E}$ ), where  $\Delta\mathcal{E}$  is the overlap energy resulting from the wavefunction interaction. The spread in energy levels (or minibands) varies



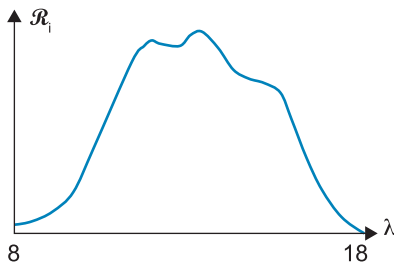
with layer thickness, with thinner layers having the wider minibands. These energy bands determine the spectral bandwidths and the material response of the QWIPs. The width of the miniband is exponentially dependent on the thickness of the barriers. The spectra of B-C QWIPs are much broader than those of B-B or B-QB QWIPs, but their absorption is also significantly lower.

Large, stark shifts can be obtained by introducing QWIPs with asymmetrical barriers. The electric field shifts of graded asymmetrical QWs are approximately an order of magnitude larger than those of symmetrical rectangular wells. They have much stronger bias-dependent behavior in escape probability, photoconductive gain, and in the responsivity spectrum. In addition, their spectral responsivity is narrower, and their cutoff wavelength is shorter compared to QWIPs operating in B-C transitions.



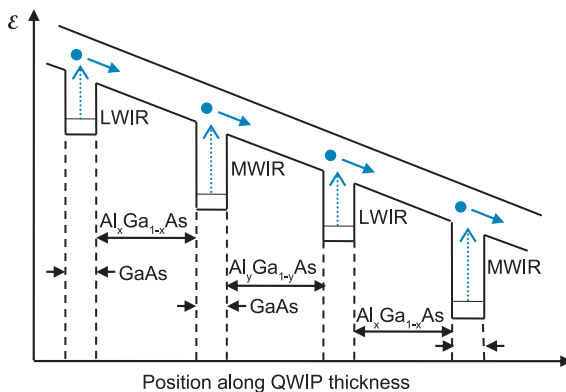
## Multispectral QWIPs

QWIPs can be manufactured with a typical narrowband ( $\Delta\lambda/\lambda \approx 10\%$ ) array, or with two-band, three-band, four-band, and broadband detector arrays. These devices are built by stacking different quantum wells in a repeating sequence. Each sequence contains several quantum wells; the thicknesses and compositions of the barrier and well layers within each sequence can be tailored to optimize each well for a different pass band that partly overlaps one or more pass bands of the other wells in the sequence. The net effect of the multiple partial overlaps is a broader overall pass band or minibands for the QWIP device as a whole.



For example, the spectral responsivity of a device made with repeating three-well sequences and designed for peak responses at three different long wavelengths is shown above.

A QWIP designed to operate simultaneously at MWIR and LWIR spectral bands is shown below.

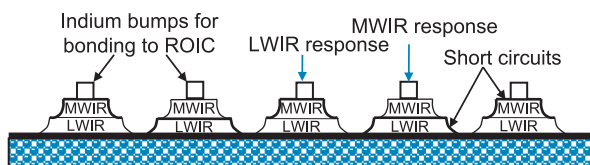


Two constraints arise with such a device: (1) the device must be supplied with two voltages, which cannot be acquired from the ROIC's available currents; and (2) to switch on MWIR detection, a high bias must be supplied to the LWIR segment.

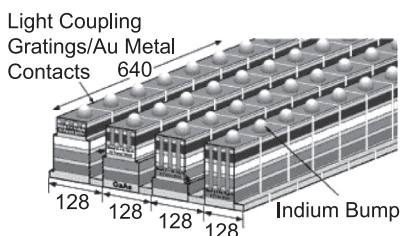


## Multispectral QWIPs (cont.)

To overcome these difficulties, the device structure is built with  $(n + 1)$  terminal contacts per pixel to access the CMOS read-out multiplexer. Then an interlace scheme is used to separate the two colors (i.e., odd-numbered rows for the MWIR QWIP and even-numbered rows for the LWIR QWIP). This interlaced short-circuiting of the MWIR and LWIR detectors eliminates complicated voltage tuning and the necessity for very high bias voltage to operate the LWIR QWIPs. The QWIP FPA is then hybridized to a CMOS multiplexer, which reads the alternating LWIR and MWIR rows, thus producing a two-color image of the same infrared scene target.



A four-band QWIP device structure with a  $640 \times 128$  pixel format of a four-band FPA is shown below. This device consists of a 15-period stack of  $4\text{--}5\text{ }\mu\text{m}$ , a 25-period stack of  $8.5\text{--}10\text{ }\mu\text{m}$ , a 25-period stack of  $10\text{ }\mu\text{m}$ , and a 30-period stack of  $13\text{--}15.5\text{ }\mu\text{m}$ . Each photosensitive MQW stack is separated by a heavily n-doped intermediate GaAs contact layer. The four-band QWIP structure is sandwiched between GaAs top and bottom n-doped contact layers and grown on a GaAs substrate. The light is incident from below.



Reprinted with permission from S. D. Gunapala et al., *IEEE Trans. Elect. Dev.* **50**(12), 2353–2360 (2003).



Reprinted with permission from R. Sweda, *III-Vs Review* **18**(2), 44–47 (2005).

A QWIP's wavelength coverage can be bandgap engineered from  $3$  to  $20\text{ }\mu\text{m}$ . The longer-wavelength limit can be easily extended using shallow quantum wells.

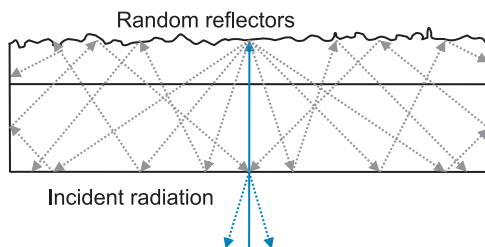
## Light Couplers

The structure of a QWIP FPA poses an optical-coupling problem because of a confluence of three considerations:

1. The direction through the thicknesses of the quantum wells is normal to the focal plane.
2. Quantum selection rules allow the detection of only that part of the incident light that is transverse electric along the direction through the thicknesses of the quantum wells (i.e., s-polarized to the focal plane).
3. The light to be detected is incident at approximately 90 deg to the focal plane; therefore, only a small fraction of it is absorbed by the QWIP.

A QWIP device is fabricated such that the planes that bound the quantum-well layers are parallel to the broad outermost faces of the device; therefore, by virtue of this quantum mechanical selection rule, light incident normal to these faces is not detected. A **light coupler** is required to redirect incident light so that it traverses the QWIP layers in a direction that includes at least some vector component parallel to the planes that make the quantum wells. In other words, the function of a light coupler on a QWIP is to redirect normally incident light to oblique incidence.

The purpose of **random reflectors** in QWIP light couplers is to divert the incoming light as efficiently as possible to propagate at large angles from the perpendicular.



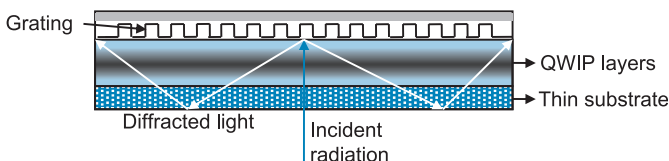
Light that is not absorbed is reflected to a different structure on each bounce, thus improving the capability of the QWIP to trap light and absorb a larger number of photons.

## Light Couplers (cont.)

Random reflectors are fabricated using lithographic processes, allowing feature sizes to be controlled to preserve pixel-to-pixel uniformity. The sizes of the random facets are proportionally scaled with the peak response wavelength of the QWIP; in this case, fewer sharp features are obtained for QWIPs operating in the midwave part of the spectrum, thus lowering the coupling efficiency of the device. Therefore, 2D periodic gratings are used for light coupling in the midwave infrared waveband.

In **2D periodic gratings**, the periodicity repeats in two perpendicular directions on the detector plane, leading to the absorption of both polarizations of incident infrared radiation. Because a 2D grating exhibits the same periodicity along the  $x$ - $y$  directions in the focal plane array, it diffracts more light to higher angles, giving rise to increased coupling.

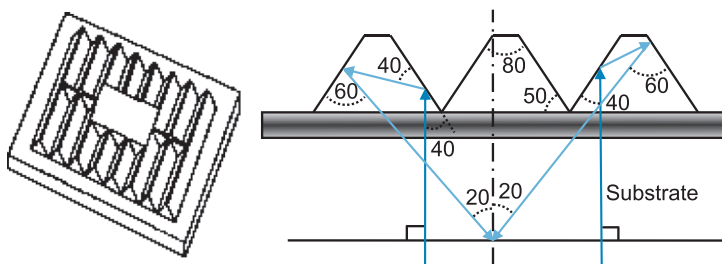
The difficulties in designing a grating for optical coupling involve choosing the proper dimensions of the grating to maximize the efficiency of the diffractive orders and attaining suitable angles away from the perpendicular. Further improvement is attained when a thin substrate of AlGaAs is attached to the cavity and produces total internal reflection (TIR). The grating peak wavelength depends linearly on the grating period, but is independent of the groove depth.



The standard approach of using gratings at the top of detectors for light diffraction has several shortcomings. For example, diffraction is less efficient for small detector pixels, which limits the array's spatial resolution. Also, each grating design is only effective for a specific wavelength, not for dual-band detection or broadband detection. The fine features in the grating design require stringent electron-beam lithography, which limits the production of these quantum devices and increases their cost.

## Light Couplers (cont.)

**Corrugated QWIPs (CQWIPs)** can be created within the detector design to allow total internal reflection to redirect light inside a detector. V-grooves are chemically etched through the active detector region down to the bottom contact layer to create a collection of angle facets within a single detector pixel. The normally incident light reflects at these angled sidewalls and travels at large oblique angles, allowing for efficient light absorption. Based on reflection rather than diffraction, the corrugated coupling scheme is both pixel-sized and wavelength-independent. These two important features improve the normalized detectivity of these corrugated devices by an order of magnitude.



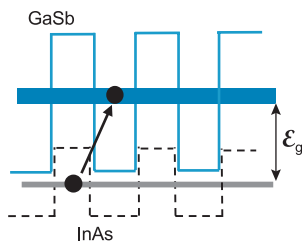
Reprinted from K. K. Choi et al., *Proc. SPIE* **3287**, 118–127 (1989).

CQWIP structures expose the active layer; therefore, the top metal contact cannot be placed directly into the detector pixel. Two solutions are considered to address this problem: leave a reserved unetched center island for contact bonding, or isolate the active layers with dielectric polymers such as pyrozone and pyrodium.

CQWIPs are appropriate for both dual-band and broadband detection. Since the corrugations are created during the separation of the detector pixels, no extra processing steps are required for their fabrication. CQWIP devices increase the absorption and improve the sensitivity of the detector IRFPA. CQWIP production is rather simple and of low cost.

## Type II Strained-Layer Superlattices

A **type II strained-layer superlattice (T2SLS)** is a Sb-based III-V material system with thin alternating nanolayers (4–20 nm) of InAs/GaSb or InAs/InGaSb that form the superlattice structure. T2SLS systems are similar to type I GaAs/AlGaAs QWIP systems, except for the overlapping conduction and valence bands in the adjacent layers. The band alignment of InAs/GaSb and the forming minibands are shown in the figure.

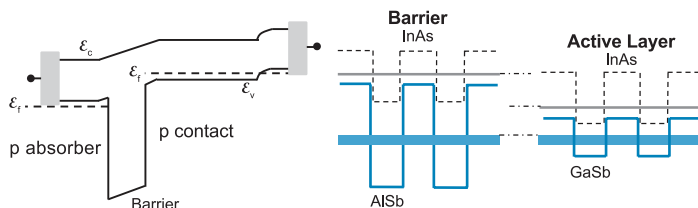


Quantum mechanics is used to calculate the electron and hole band structures and the effective bandgap. The absorption of these devices is strong, thus providing high responsivity and quantum efficiency. The effective bandgap of T2SLS devices can be tailored from 2 to 30  $\mu\text{m}$  by varying the thickness and height of constituent layers.

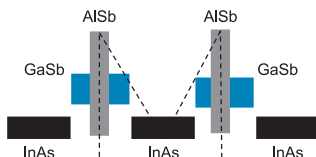
Photovoltaic p-i-n structures are required to detect cutoff wavelengths in the 8- to 12- $\mu\text{m}$  spectral range. These photodiodes are formed by doping the superlattice with trace amounts of Be, Te, or Si. The major technological challenge for the fabrication of small-area-size p-i-n photodiodes is the number of generated surface leakage currents due to tunneling electrons. The suppression of these large G/R surface leakage mechanisms is minimized by the use of barrier structures. These devices show dark current reduction of at least two orders of magnitude at 77 K. In theory, T2SLS photodetectors have the potential to match or even exceed HgCdTe detector performance. This novel technology has superior uniformity compared to HgCdTe and creates affordable multicolor and multiband detector FPAs.

## Type II Strained-Layer Superlattices (cont.)

The schematic profile and band diagrams of both the active and barrier layers of a pBp device are shown below.



Complex SLS supercell structures can be fabricated to further reduce the electrical noise due to the dark current. For example, the M-structure superlattice uses a barrier between the p and n regions of the superlattice photodiode. The AlSb barrier efficiently blocks the interaction between electrons in the two adjacent InAs wells, thereby suppressing both the tunneling probability and the diffusion current of the device.



Improvement areas are material quality and surface passivation of small pixels in large arrays, particularly as the cutoff wavelength is extended to the LWIR spectral band. The increase in quantum efficiency and high pixel operability are essential factors as well. Further strategies should concentrate on decreasing or even removing the band offset in the barrier layer. Such improvement will result in lower operating bias, reduced dark current, and the ability to perform efficiently in HOT conditions.

## Dual-Band IRFPA Technology: Advantages

---

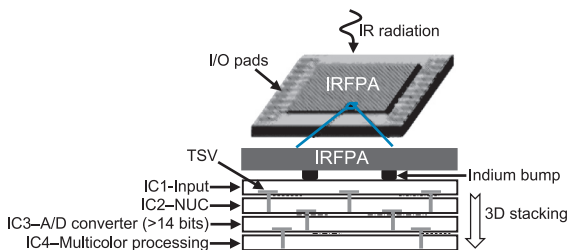
A unique aspect of dual-band IRFPAs is that they are able to read out independent spectral data. Both MWIR and LWIR spectral bands are highly correlated and are imaged at the same detector plane. They are both able to read out the scenes simultaneously with the same pixel size and resolution. Merging MWIR and LWIR spectral bands into a single system allows for numerous system trades:

- It provides adequate resolution in the MWIR spectral region.
- The effective SNR exceeds that of a single-color IRFPA. The merge also enables advanced color-processing algorithms to further improve sensitivity.
- Serious information such as background clutter and sun glint may be subtracted from an infrared image, leaving only the target(s) of interest.
- It offers narrowband responses and wavelength tailorability. Specific midwave and longwave spectral regions might be selected where the emissivity of a two-color infrared window is the lowest possible.
- It maximizes performance when viewing targets with low and high temperatures.
- It computes absolute temperatures of a target with unknown emissivity, which is important to the process of identifying temperature differences between missile targets, warheads, and decoys.
- It shows good performance in all weather conditions. The transmittance in the LWIR is superior in the presence of haze because it attenuates less than the MWIR (i.e., CO<sub>2</sub> heavily absorbs MWIR radiation). However, in high humidity, MWIR is clearly better than LWIR due to its low water vapor absorption.

An alternative method of exploiting dual-band IRFPAs is to use the dual-band nature of the focal plane to simultaneously view different scenes with dissimilar magnifications. For example, this method will enable a pilot and co-pilot to access a wide FOV for battlefield situational awareness while performing narrow-FOV feature identification tasks.

### 3D Read-Out Integrated Circuits

ROIC technology has become a major barrier in the evolution of high-performance IRFPAs. The addition of vertical processing layers of silicon foundry interconnected using metal-filled **through-silicon vias (TSVs)** addresses this obstacle.



Each of the layers is tested, thinned, and glued over the layer below it. TSVs are then etched and metalized to interconnect the pixels. The **3D integration** is performed at the die-to-die or die-to-wafer level, which increases yield and allows a higher degree of flexibility. Wafers/die can be of different sizes and materials, and the individual device layers can be manufactured in different foundries.

3D interconnect technology can be used to increase the charge storage area of the read out in small pixel limits. The increase in charge capacity allows the full use of available signal current, thus increasing the sensitivity of the device. Smart windowing techniques for large IRFPAs can be implemented to detect changes from frame-to-frame and to read out only the relevant information from the FPA at a particular instant. This windowing function provides elemental decision making, while keeping data processing power to a minimum. 3D architecture also offers parallel signal manipulation, thus expanding the number of spectral bands. Other possible functions are analog-to-digital conversion, threshold timing, and circuit latching. The dynamic range can be expanded from 14 bits to 20 bits or more.

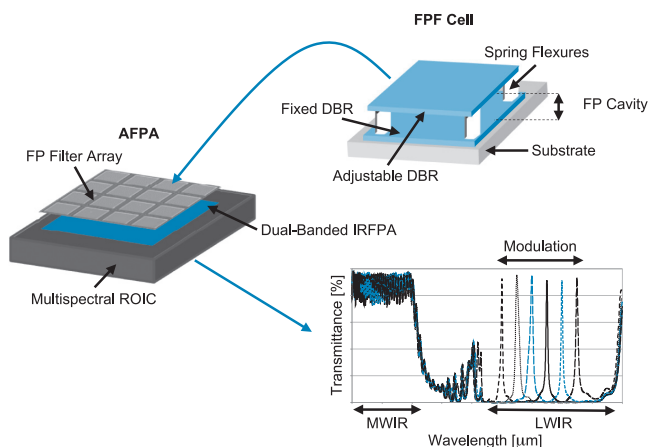
This novel ROIC technology could ultimately result in the sensor behaving like a smart system rather than a passive component, with complex image-processing functions being executed on the FPA chip.



## Adaptive FPAs

The effectiveness of infrared imaging sensors for target detection and identification is greatly enhanced by adding spectral analysis capability. Multispectral and hyperspectral datasets are normally acquired by using Fourier transform or grating spectrometers. Presently, these conventional apparatuses are heavy, slow, large computational devices that generate large volumes of data, thus delaying image collection and processed-information delivery. Other drawbacks include the inefficient utilization of detector pixels and/or available integration time with relevant spectral bands, as well as complications caused by push-broom scanning artifacts and pixel spectral misregistration.

Significant benefits can be achieved by developing a miniaturized light-weight IR spectrometer. This is achieved by coupling a double-band FPA with a **micro-electro-mechanical systems (MEMS)-based Fabry–Pérot filter (FPF)**. This **adaptive focal plane array (AFPA)** allows narrowband (100–150 nm) spectral tuning in the LWIR with simultaneous broadband pixel-registered imagery in the MWIR. AFPAs enhance target discrimination (e.g., detection/identification) of concealed targets and can be deployed on SWaP-constrained platforms to provide real-time information. (DBR in the figure means distributed Bragg reflector; see next page.)



[Graph adapted from W. Gunning (2007).]

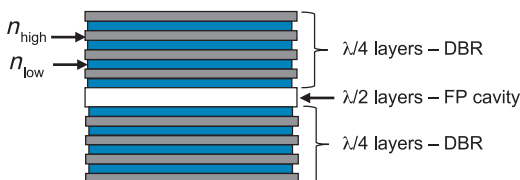
### Adaptive FPAs (cont.)

AFPA designs allow individual areas of an IRFPA to be spectrally filtered independently of each other.

The bandpass wavelength is determined by the resonant condition, where the total cavity thickness corresponds to one half-wave ( $\lambda/2$ ) of the optical phase. FPFs that operate in the MWIR and LWIR spectral regions are, in most cases, **distributed Bragg reflectors (DBRs)**. DBRs are dielectric coatings formed from multiple quarter-wave ( $\lambda/4$ ) layers of alternating materials with varying refractive indices (e.g., Ge/ZnS). The reflectance of a DBR stack is given by

$$\rho = \left[ \frac{n_0(n_2)^{2N} - n_s(1)^{2N}}{n_0(n_2)^{2N} + n_s(1)^{2N}} \right]^2$$

where  $N$  is the number of repeated pair layers, and  $n_0$ ,  $n_1$ ,  $n_2$ , and  $n_s$ , are the refractive indices of the incident media, the two alternating materials, and the terminating substrate, respectively. The reflectance increases as the refractive index contrast between the material in the Bragg pairs increases or the number of pairs in a DBR is incremented.



The peak transmittance and bandwidth of a FPF can be calculated by

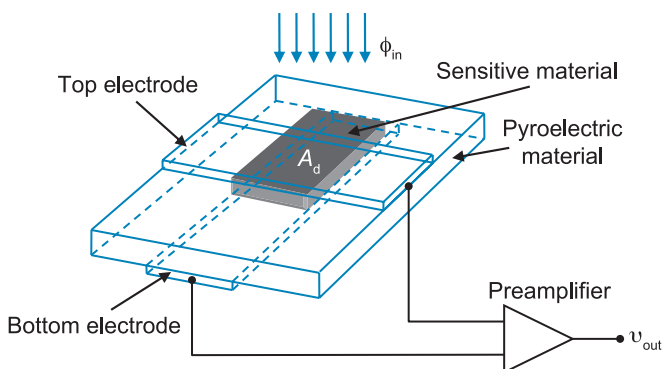
$$\tau_{\text{peak}} = \left( 1 - \frac{a}{1 - \rho} \right)^2 \quad \Delta f = \frac{1 - \rho}{\pi m \sqrt{\rho}}$$

where  $\rho$  is the reflectance,  $a$  is the absorptance, and  $m$  is any integer that denotes the order of interference. The **finesse**, the figure of merit used to measure the resolution of a FPF, is inversely proportional to the wavefront error. Finesse is defined as

$$F = \frac{\pi \sqrt{\rho}}{\rho}$$

## Pyroelectric Detectors

**Pyroelectric detectors** are made of monoclinic ferromagnetic crystals that have a high degree of crystalline asymmetry and therefore possess an electric dipole moment. Incident radiation heats the device, expanding the crystalline lattice and changing the dielectric constant, which alters the internal dipole moment, thus producing a change in the surface charge density and in the polarization state of the material. This affects the charge on the mounted metal electrodes and causes a current to flow in an external circuit. The electrodes must be placed on opposite faces of the crystal perpendicular to the polarization axis.



At a constant sample temperature, this internal polarization is neutralized by mobile charges on the surface of the sample; therefore, there is no voltage difference measured by the metal electrodes. A change in irradiance causes a temperature variation, thus producing a change in polarization; consequently, a measurable voltage difference occurs at the detector's output. As a result, pyroelectric detectors based on ferroelectric materials can only be used in an ac mode. In order to detect these small charges, low-noise, high-impedance amplifiers are necessary.

The surface temperature is modulated in time by means of a radiation chopper. The chopper provides a continuous source of temperature variation that allows the material to generate charge while a scene is monitored.

## Pyroelectric Detectors (cont.)

This differential aspect provides a real-time calibration of offset non-uniformity, making the sensor essentially unaffected by severely dynamic thermal environments. High chopping frequencies (usually 25–60 Hz) are supported by pyroelectric devices in exchange for sensitivity. The polarization change in these ac-coupled devices is quite fast, but the thermal properties of the detector limit the high-frequency response.

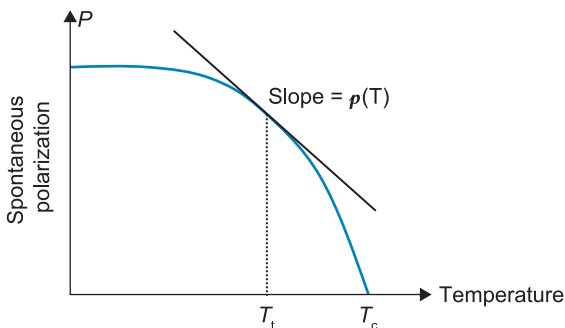
The pyroelectric coefficient  $\rho$  measures the rate of change of electric polarization with respect to temperature:

$$\rho = \frac{dP}{dT}, \quad [\text{C}/\text{cm}^2\text{K}]$$

where  $P$  is the magnitude of internal polarization, and  $T$  is the temperature in Kelvin. An applied field induces an electrical displacement  $\mathbf{D}$ , resulting in a more general coefficient:

$$\rho(\mathbf{E}) = \frac{d\mathbf{D}}{dT}$$

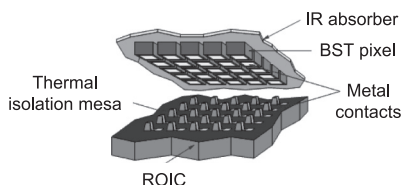
This produces a stable response in ferroelectric materials operated below and above their temperature phase transition (i.e., the Curie temperature  $T_c$ ). Once the material is heated above the Curie temperature, the ferroelectric material produces large pyroelectric coefficients.



In some cases, an absorption layer is applied in front of the responsive element to improve its absorption behavior.

## Pyroelectric Detectors: Mathematical Approach

Most pyroelectric FPA sensors are made from barium strontium titanate (BST), a crystal of ferroelectric ceramic material hybridized to a CMOS multiplexer circuit and mounted in contact with a thermoelectric cooler/stabilizer. The device's temperature set point is set close to the BST crystal's Curie temperature, or the narrow temperature band at which the crystal material exhibits the highest polarization relative to the detector's temperature change resulting from scene illumination.



Pyroelectric sensing materials are sensitive from  $0.2\ \mu\text{m}$  to over  $100\ \mu\text{m}$ , and their spectral range is limited only by the infrared window placed in front of the detector.

To investigate how a pyroelectric material produces an electrical current, it is good to start with Maxwell's equation, known as Gauss's law in its differential form:

$$\nabla \cdot \mathbf{D} = \rho$$

where  $\mathbf{D}$  is the electric displacement, and  $\rho$  is the electric charge. From elementary electrostatics,

$$\mathbf{D} = \epsilon_0 \mathbf{E} + \mathbf{P}$$

where  $\mathbf{E}$  is the electric field,  $\mathbf{P}$  is the polarization, and  $\epsilon_0$  is the permeability of the material. Below the Curie temperature,  $\mathbf{P}$  is large compared to  $\epsilon_0 \mathbf{E}$ ; therefore,  $\mathbf{D}$  and  $\mathbf{P}$  can often be used interchangeably, in which case

$$\nabla \cdot \mathbf{P} = \rho$$

Applying Green's theorem and integrating over a cylindrically shaped volume that covers the area of one side of the detector that has an electrical lead, we arrive at the following equation:

## Pyroelectric Detectors: Mathematical Approach (cont.)

$$\int_{\text{Vol}} \rho dV = \int_{\text{Vol}} \nabla \cdot \mathbf{P} dV = \int_{\text{Sur}} \mathbf{P} dA_d = \mathbf{P} A_d$$

When the ferroelectric material is aligned so that the intrinsic polarization is perpendicular to the surface through which the current flows, the detector current is

$$i = \frac{d\mathbf{P}A_d}{dt} = A_d \frac{d\mathbf{P}}{dT} \frac{dT}{dt} = A_d \rho \frac{dT}{dt}$$

From this equation, it is clear that current flows through the device only when a temperature change  $dT/dt$  occurs, thus resulting in an ac detector.

The temperature difference  $\Delta T$  between the ferromagnetic material and the heat sink is related to the incident radiation by the heat balance equation:

$$H \frac{d(\Delta T)}{dt} + K\Delta T = \varepsilon \phi_e(t)$$

where  $K$  is the thermal conductance,  $H$  is the heat capacity,  $\varepsilon$  is the emissivity of the surface material, and  $\phi_e$  is the flux in energy-derived units.

Since the radiation is modulated at an angular frequency  $\omega$ , it can be expressed as an exponential function  $\phi_e = \phi_{e,o} e^{j\omega t}$ , in which case the heat balance equation provides the following solution:

$$|\Delta T| = \frac{\varepsilon \phi_{e,o} R_{th}}{\sqrt{1 + (\omega \tau_{th})^2}} \Rightarrow \tau_{th} \equiv \frac{H}{K} = R_{th} C_{th}$$

where  $\tau_{th}$  is the thermal time constant, and  $C_{th}$  and  $R_{th}$  are the thermal capacitance and thermal resistance, respectively, of the ferroelectric material.

Recognizing that  $\frac{d(\Delta T)}{dt} = \frac{dT}{dt}$ , we obtain

$$\left| \frac{dT}{dt} \right| = \frac{\omega \varepsilon \phi_{e,o} R_{th}}{\sqrt{1 + (\omega \tau_{th})^2}}$$

The detector current flowing through the pyroelectric is

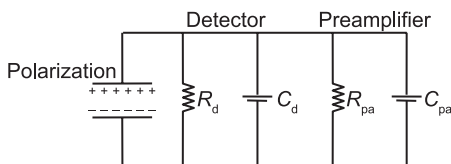
## Pyroelectric Detectors: Mathematical Approach (cont.)

$$i = \frac{p\omega\epsilon\phi_{e,o}R_{th}A_d}{\sqrt{1 + (\omega\tau_{th})^2}}$$

Thus, the current responsivity is defined as

$$\mathcal{R}_i = \frac{i}{\phi_{e,o}} = \frac{p\omega\epsilon R_{th}A_d}{\sqrt{1 + (\omega\tau_{th})^2}}$$

The equivalent circuit of a pyroelectric element is shown below.



The voltage across the pyroelectric device is the current times the parallel electrical impedance of the detector/preamplifier combination, yielding

$$v = \frac{iR}{\sqrt{1 + (\omega\tau_{RC})^2}}$$

where  $\tau_{RC}$  is the electrical time constant. The voltage responsivity is simply

$$\mathcal{R}_v = \frac{p\omega\epsilon R_{th}RA_d}{\sqrt{1 + (\omega\tau_{th})^2}\sqrt{1 + (\omega\tau_{RC})^2}}$$

At high frequencies, the voltage responsivity is inversely proportional to frequency, while at low frequencies, it depends on the electric and thermal constants.

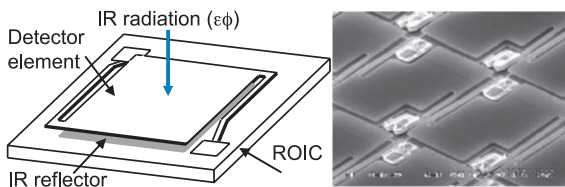
The dominant noise in pyroelectric detectors is most commonly Johnson noise, so the normalized detectivity may be calculated by

$$D^* = \frac{\mathcal{R}_v\sqrt{A_d\Delta f}}{v_j} = \frac{p\omega\epsilon(R_{th}A_d)\sqrt{RA_d}}{\sqrt{4kT}\sqrt{1 + (\omega\tau_{th})^2}\sqrt{1 + (\omega\tau_{RC})^2}}$$

## Microbolometers

Microbolometers are thermistor-based detectors that measure temperature change in a thermally isolated membrane heated by infrared radiation absorbed on the surface. **Micro-electro-mechanical systems (MEMS)** technology is used to provide good thermal isolation from the silicon ROIC substrate and to obtain a high fill factor as well as good integrated circuit process compatibility.

Starting with a large silicon wafer, CMOS multiplexer (MUX) circuitry is fabricated by a commercial silicon foundry. The infrared detector foundry then deposits successive layers of silicon nitrate ( $\text{Si}_3\text{N}_4$ ) and silicon dioxide ( $\text{SiO}_2$ ) to fabricate a bridge structure. A layer of vanadium oxide ( $\text{VO}_x$ ), commonly known as vanadium pentoxide ( $\text{VO}_5$ ), amorphous silicon (a-Si), or yttrium-barium-copper-oxide ( $\text{YBa}_2\text{Cu}_3\text{O}_5$ ) is used to form a thin-film resistor over the surface of the bridge deck. Integral thin legs are released from the successive layers of  $\text{SiO}_2$ . These legs provide structural support to the detector material and electrical contact between the CMOS MUX and the film resistor on the bridge deck. Once all of the layers necessary to build the complete pixel structure have been deposited, a gas is used to dissolve the sacrificial materials, and a freestanding suspended bridge is created. The wafer with individual detectors is tested, and the functioning parts are diced and packaged into vacuum (typically,  $10^{-6}$  Torr) for thermal insulation. The structure is dimensioned to operate at 60/120/240 Hz frequencies by adjusting the thermal conductance of the isolating legs to match the desired time constant.



The optical cavity is tuned for maximum absorption at a wavelength  $\lambda_m = 4nd$ , where  $d$  and  $n$  are the thickness and index of refraction, respectively, of the microbolometer material.

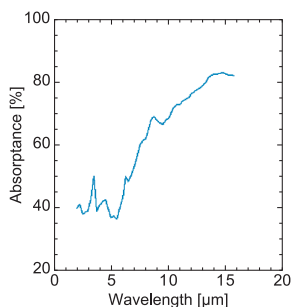


## Microbolometers (cont.)

The infrared reflecting surface at the bottom of the optical cavity improves the thermal response of the device.

The two most commonly used IR radiation detecting materials in microbolometers are  $\text{VO}_x$  and a-Si. Other materials that have been investigated are a-Si carbide,  $\text{YBaCuO}$ , poly SiGe, and  $\text{GeSiO}$ . These materials exhibit large thermal resistance coefficients (TRCs) of  $2\text{--}5\% \text{K}^{-1}$ . Microbolometer technology requires the deposition of these high-TRC materials after CMOS fabrication. The post-CMOS surface micromachining process is complicated and expensive, thus increasing the cost of these devices. Furthermore, one of the difficulties of microbridge structures is the limited optical fill factor ( $\sim 65\%$ ) because the detector area is reduced by the support legs.

The pixel structure of the basic microbolometer FPAs allows a substantial percentage of infrared radiation to pass through and exit the TRC material without being absorbed. As a consequence, the decrement in performance of the thermal device is rather significant.

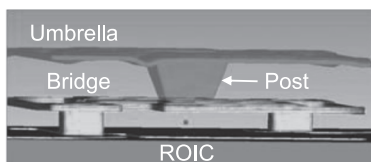
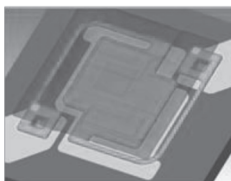


Basic microbolometer structures of conventional uncooled FPAs have been recently improved by DRS Sensors and Targeting Systems. The DRS approach consists of placing a high-fill-factor absorber ( $>90\%$ ) with a high resistivity on top of the microbridge. This patented top layer, called the “umbrella” structure, enhances the absorption in both MWIR and LWIR spectral regions.

The absorption structure is formed of a layer of nickel-chromium (NiCr), or another highly resistive alloy or

## Microbolometers (cont.)

metal, sandwiched between two layers of  $\text{SiO}_2$  and supported by a central post, also formed of  $\text{SiO}_2$ . This post serves as a thermal connection between the absorbing layer composition and the transducer bridge.

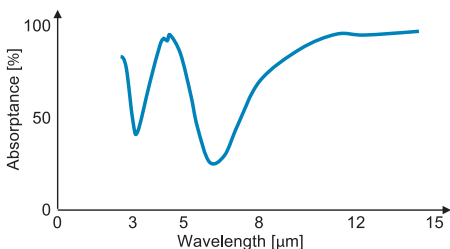


Images courtesy of DRS Technologies, Inc.

The umbrella pixel structural design is strongly absorptive to radiation of a predetermined spectral band. It can be tailored to control the thermal conductance and heat capacitance, and to maximize the absorption of infrared radiation, thus minimizing the noise contributions and maximizing the responsivity. The combined spacing of the two existing gaps in this structure is  $\lambda/4n$  or  $3\lambda/4n$ .

Modern microbolometer technology is suitable to operate in either MWIR or LWIR wavebands; however, at 300 K the performance of a MWIR thermal detection system is decremented by a factor of 9.4 compared to the same system operating in the LWIR. The MWIR spectral band is commonly used with narrowband-pass filters for high-temperature applications such as hostile fire detection.

State-of-the-art devices are based on  $1280 \times 1024$ ;  $12\text{-}\mu\text{m}$  pixel @ 120 Hz and  $640 \times 480$ ;  $12\text{-}\mu\text{m}$  pixel @ 240 Hz (high performance),  $320 \times 240$ ;  $17\text{-}\mu\text{m}$  pixel @ 120 Hz (most common), and  $160 \times 120$ ;  $25\text{-}\mu\text{m}$  pixel @ 60 Hz (low cost). The response time for a  $17\text{-}\mu\text{m}$  pixel is 10–12 msec and for a  $12\text{-}\mu\text{m}$  pixel is 7–8 msec. Typical LWIR FPA sensitivities



Courtesy of L3 Technologies

are 35 mK (best performance 18–24 mK) for  $F/\# < 1.2$  optical devices. Microbolometers can be windowed to operate at fast frame rates (e.g., 600 fps).

## Microbolometers: Mathematical Approach

The resistance in a microbolometer semiconductor material has an exponential dependence on temperature:

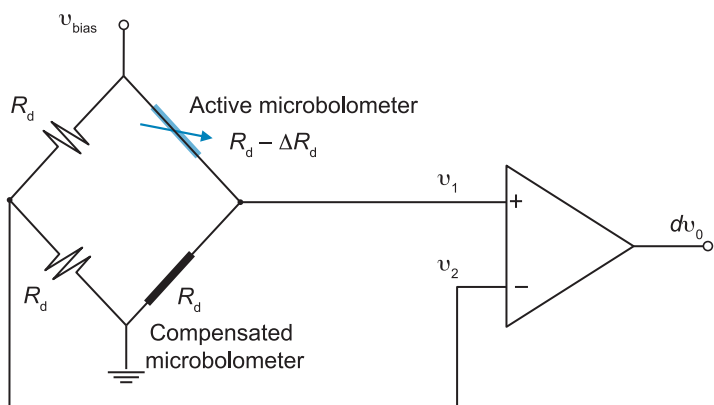
$$R_d = R_o e^{(\frac{1}{T} - \frac{1}{T_o})},$$

where  $R_o$  is the ambient resistance at a nominal temperature  $T_o$ , and  $\mathcal{C}$  is a material characteristic constant. The resistance change that results from the optically induced temperature change is obtained by differentiation, yielding a TRC of

$$\alpha = \frac{1}{R_d} \frac{dR_d}{dT} = -\frac{\mathcal{C}}{T^2}$$

When infrared radiation is absorbed into the microbolometer material, the material's temperature rises slightly, causing a small decrease in resistance. In order to produce an electrical current from this change in resistance, a bias voltage must be applied across the sensing device. This is accomplished by interfacing two identical microbolometer chips into a Wheatstone bridge.

When infrared radiation is incident on the active microbolometer, the detector resistance  $R_d$  decreases by  $\Delta R_d$ , thus unbalancing the bridge and producing an electrical current through the active device. The compensated microbolometer is shielded from infrared radiation, and the operational amplifier amplifies the output signal.



### Microbolometers: Mathematical Approach (cont.)

The heat balance differential equation that relates the incident radiation to the heat loss is given by

$$H \frac{d\Delta T}{dt} + K\Delta T = \varepsilon\phi_e$$

where  $H$  is the heat capacity [ $\text{J} \cdot \text{K}^{-1}$ ],  $K$  is the thermal conductance [ $\text{W} \cdot \text{K}^{-1}$ ],  $\varepsilon$  is the emissivity of the surface, and  $\phi_e$  is the IR flux in watts. Assuming that a periodic radiant power incident on the microbolometer is sinusoidally varying (i.e.,  $\phi_e = \phi_{e,o}e^{j\omega}$ ), the heat balance differential equation provides the following solution:

$$|\Delta T| = \frac{\varepsilon\phi_{e,o}}{K\sqrt{1 + \omega^2\tau_{th}^2}} \Rightarrow \tau_{th} \equiv \frac{H}{K} = R_{th}C_{th}$$

where  $\tau_{th}$  is the thermal time constant,  $R_{th}$  is the thermal resistance, and  $C_{th}$  is the thermal capacitance.

The transfer function of the electronic circuit is

$$dv_o = \frac{v_{bias}}{2} \frac{\Delta R_d}{2R_d - \Delta R_d} = \frac{v_{bias}}{2} \frac{\alpha\Delta T}{2 - \Delta T}$$

where  $dv_o$  is the change in output voltage due to the change in detector resistance  $\Delta R_d$ , which is given by

$$\Delta R_d = \frac{dR_d}{dT}\Delta T = \alpha R_d\Delta T$$

Substituting  $\Delta T$ , the radiation-induced change in output voltage  $dv_o$  is

$$dv_o = \frac{\alpha\varepsilon\phi_{e,o}v_{bias}}{4K\sqrt{1 + \omega^2\tau_{th}^2} - 2\varepsilon\phi_{e,o}}$$

The voltage responsivity is obtained by dividing both sides of the previous equation by  $\phi_{e,o}$ :

$$\mathcal{R}_v = \frac{\alpha\varepsilon v_{bias}}{4K\sqrt{1 + \omega^2\tau_{th}^2} - 2\varepsilon\phi_{e,o}}$$

While photon detectors are subject to BLIP conditions, microbolometer detectors are subject to temperature and background fluctuation noise limits.

## Microbolometers: Mathematical Approach (cont.)

Whatever the heat-loss mechanisms (i.e., convection, conduction, and/or radiation) are, the ultimate sensitivity  $D^*$  is set by the temperature fluctuation noise

$$D_{\text{TF}}^* = \sqrt{\frac{\epsilon A_{\text{d}}}{4kKT_{\text{d}}^2}}$$

If the microbolometer is thermally isolated so well that the only heat mechanism is by radiation from the pixel to its surroundings, the thermal device is said to be background fluctuation noise limited. In this case, the sensitivity of the device is given by

$$D_{\text{BF}}^* = \sqrt{\frac{\epsilon}{8k\sigma(T_{\text{d}}^5 + T_{\text{bkg}}^5)}}$$

The sensitivity is independent of the responsivity. The purpose of having a high responsivity is to minimize the contribution of the total system noise from the electronics in the ROIC from the IRFPA. Obviously, if the noise is dominated by the electronic noise, the microbolometer cannot be either fluctuation or background noise limited.

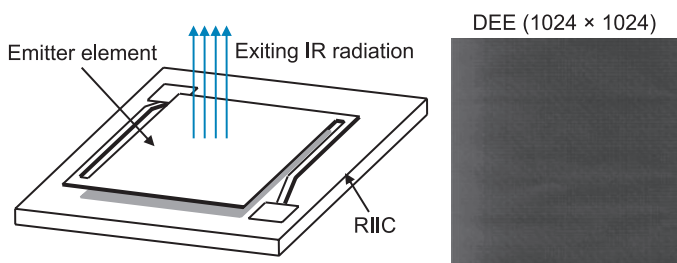
### Design elements for consideration in microbolometer performance:

- read-out noise from the CMOS devices,
- the thermal resistance coefficient (TRC),
- thermal isolation of the active device from the substrate,
- the vacuum level in the sealed detector package, eliminating the convective transfer of energy between pixels, and
- detector time constant or response time. Even though the detector must be thermally isolated, it must be able to transfer some energy to the substrate so that the device does not heat up due to constant radiation impinging on it. The thermal constant must be optimized to provide both high sensitivity and a small integration time.

## Infrared Dynamic Scene Simulators

What would happen if the process of a microbolometer were reversed? In this case, the resistive element would be connected to a read-in integrated circuit (RIIC) instead. This would result in an emitter array instead of the classical detector FPA, which is the principle of operation of a **dynamic scene simulator (DSS)**. The emitter element is called the digital emitter engine (DEE). These types of devices are used in laboratory dynamic infrared scenarios, thus reducing the cost of field testing. They also offer shorter development cycles for infrared-based imaging systems by giving developers more immediate access to data.

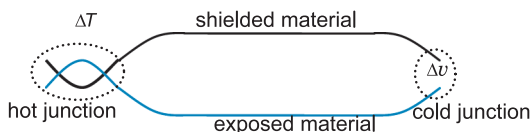
For example, the MIRAGE™-XL DSS from Santa Barbara Infrared, Inc. (SBIR) is an emitter array with a resolution of  $1024 \times 1024$  pixels. Its RIIC is designed to be mechanically mated to the suspended membrane, resulting in resistively heated micro-emitters. Each micro-emitter element is electronically connected to one of the  $1024 \times 1024$  RIIC unit cells, allowing individual control of the current driven through each emitter element during scene generation. As in the microbolometer, the electrical connection to the emitter from the RIIC also serves as the mechanical support for the emitter structure and provides the thermal path for the heat flow during operation.



To generate the scene, the RIIC must be supplied with the required bias voltage, timing, and formatter digital scene data (e.g., DVI digital video or NTSC/PAL analog video).

## Thermoelectric Detectors

A **thermoelectric detector** or **thermocouple** comprises two junctions between two dissimilar conductors having a large difference in their thermoelectric power (i.e., a large **Seebeck coefficient**  $\Theta$ ). The hot junction is an efficient absorber exposed to incident radiation, while the cold junction is purposely shielded.



The diagram above displays the Seebeck effect, where two semiconductor materials are joined at a hot point, and a temperature  $\Delta T$  is maintained between the hot and cold junctions; an open-circuit voltage  $\Delta v$  is developed between these materials at the cold point:

$$\Delta v = \Theta \Delta T \rightarrow \Theta \quad [\mu\text{V/K}]$$

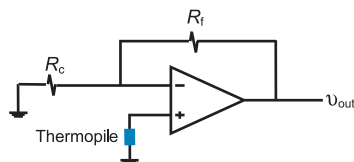
To obtain efficient and large electrical conductivity  $\sigma$ , both the thermal conductivity  $K$  and the Joulean heat loss must be minimized. This is achieved by maximizing the coefficient  $\sigma\Theta^2/K$  found in some heavily doped semiconductors.

The voltage output between the two dissimilar materials is increased by connecting numerous thermocouples in series, creating a device called a radiation **thermopile**. The responsivity of a thermopile is given by

$$\mathcal{R}_v = \frac{\varepsilon \Theta N}{K \sqrt{1 + \omega^2 \tau_{th}^2}}$$

where  $N$  is the number of thermocouples in the electrical series.

The thermopile device may then be interfaced to an operational amplifier circuit to increase the voltage to usable levels.



Thin-film techniques enable chip thermopiles to be fabricated as complex arrays with good reliability.

## Carbon Nanotubes for Infrared Applications

---

A **carbon nanotube (CNT)** is a tubular structure of single sheets of graphene. CNTs come in two principal forms, single-walled (SWCNT), a one-atom-thick layer of graphene, and multiwalled (MWCNT), multiple concentric layers of graphene. These allotropes of carbon are excellent materials for infrared applications due to their outstanding electronic and optoelectronic properties, along with their mechanical and chemical robustness.

SWCNTs are favorable candidates for future uncooled IRFPAs because of their low thermal mass, strong absorption coefficients, and TRCs of greater than  $3\% \text{ K}^{-1}$ . Photo-thermal chemical vapor deposition (PTCVD) processes are used to produce SWCNTs that can be deposited on top of the microbolometer bridge structures. CNTs are also compatible with Si-founded technology, thus allowing wafer-scale CNT IRFPAs to be integrated directly onto ROIC unit cells.

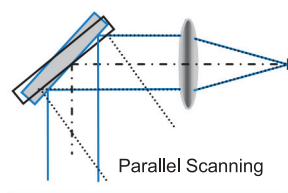
These asymmetric carbon structures can also form photodiodes by using SWCNTs of varying diameters and wavelength tunability. Electron-beam lithography and plasma edging techniques can be used to realize large arrays of nanopillars with excellent uniformity over large surfaces. These nanoscale photodiode structures have the potential to attain high sensitivities, fast frame rates, and high operational temperatures.

Vantablack<sup>®</sup> is an effective light-suppression material and is composed of millions of vertically aligned nanotube arrays. Incident radiation ricochets among the CNTs and is rapidly absorbed by the tubular structures. These functional coatings exhibit  $<0.15\%$  total hemispheric reflectance across the visible and infrared spectral wavebands, thus creating a virtually perfect black surface. Vantablack<sup>®</sup> has virtually undetectable levels of outgassing and particle fallout, and can be used to reduce scatter and stray light, thus improving the performance of thermal imaging systems.

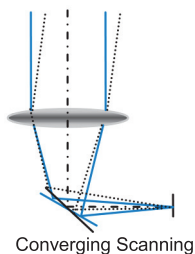


## Raster Scan Format: Single Detector

Scanning mechanisms are often necessary in infrared systems to cover a 2D FOV with a reasonable number of detector elements, or when a substantial FOV is required. The many applications that need scanning usually depend on optomechanical elements to direct and focus the infrared radiation. There are two basic types of scanners: pre-objective or **parallel-beam scanners**, and post-objective or **converging-beam scanners**.



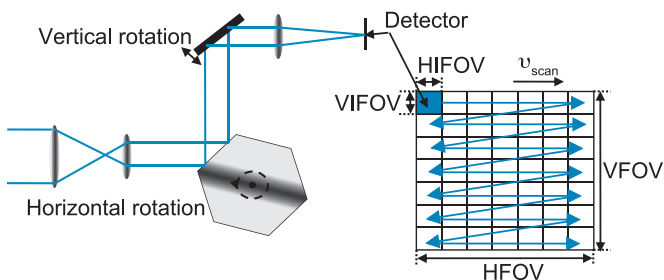
In parallel scanning, the scanning element is in front of the final image-forming element and must be the entrance pupil of the optical system. The converging scanner has the moving element between the final optical element and the image, and works on axis.



There are three basic scan formats: raster, parallel, and the staring focal plane array.

In raster scan mechanisms, a single detector is scanned in two orthogonal directions in a 2D raster across the FOV. The moving footprint sensed by the detector is called the **instantaneous field of view (IFOV)**, and the specific time required for the footprint to pass across the detector is called the **dwell time**

$\tau_{\text{dwell}}$ .



One-hundred percent scan efficiency  $\eta_{\text{scan}}$  is assumed. Scan inefficiencies include overlap between scan lines, over-scanning of the IFOV beyond the region sensed, and finite retrace time to move the detector to the next line.

### Raster Scan Format: Single Detector (cont.)

The number of horizontal lines making up a 2D scene is given by

$$n_{\text{lines}} = \frac{\text{vertical field of view (VFOV)}}{\text{vertical instantaneous field of view (VIFOV)}}$$

The time needed to scan one particular line is

$$\tau_{\text{line}} = \frac{\tau_{\text{frame}}}{n_{\text{lines}}} = \tau_{\text{frame}} \frac{\text{VIFOV}}{\text{VFOV}}$$

The dwell time is the line time divided by the number of horizontal pixels contained in that line:

$$\tau_{\text{dwell}} = \frac{\tau_{\text{line}}}{\text{horizontal field of view (HFOV)}/\text{horizontal instantaneous field of view (HIFOV)}}$$

The scan velocity and the dwell time can be written as

$$v_{\text{scan}} = \frac{\text{HFOV}}{\tau_{\text{line}}} \Rightarrow \tau_{\text{dwell}} = \frac{\text{HIFOV}}{v_{\text{scan}}}$$

The dwell time can be also interpreted as the frame time divided by the total number of pixels within the 2D FOV:

$$\tau_{\text{dwell}} = \frac{\tau_{\text{frame}}}{(\text{VFOV}/\text{VIFOV}) \cdot (\text{HFOV}/\text{HIFOV})} = \frac{\tau_{\text{frame}}}{n_{\text{pixels}}}$$

where the frame time can be found by

$$\tau_{\text{frame}} = n_{\text{lines}} \cdot \tau_{\text{line}} = \frac{\text{VFOV}}{\text{VIFOV}} \cdot \frac{\text{HFOV}}{v_{\text{scan}}}$$

The electronic bandwidth can be written in terms of the dwell time as

$$\Delta f = \frac{1}{2\tau_{\text{dwell}}}$$

A scanning system that covers the entire FOV with a single detector considerably lowers the duration that the sensing element remains on a particular IFOV and therefore results in a higher noise-equivalent bandwidth.

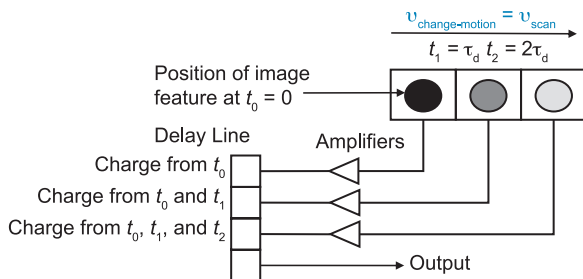
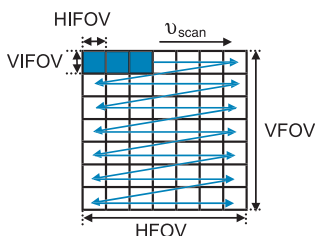
A longer dwell time is obtained using a multiple-detector system. In this case, the noise is reduced by the square root of the number of sensing elements, thus improving the SNR of the infrared system.

## Multiple-Detector Scan Formats: Serial Scene Dissection

**Serial scanning** uses multiple sensors along the scan direction in such a way that each point in the image is scanned by all detectors.

The number of detectors used in a practical system varies between two and ten.

The main mechanism used to implement a serial scan is called **time delay and integration (TDI)**. TDI requires a synchronized delay line (typically a charge-coupled device) to move the signal charge along with the optical-scan motion. A particular IFOV is viewed  $n_d$  times,  $n_d$  being the number of detectors in series dissecting the overall system's FOV of the scanned system. The output charge from each detector is added together as the serial scan proceeds. As a result, the amplitude of the added charge signal is incremented  $n_d$  times, and the uncorrelated noise, since it is added in quadrature, is intensified by a factor of  $\sqrt{n_d}$ . The overall SNR of the system is thereby improved by the square root of the number of sensor elements.



**Advantage:** The non-uniformity of the detectors is improved.

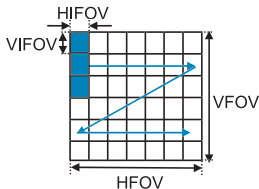
**Disadvantages:** High mirror speeds are necessary to cover the 2D FOV. A TDI circuit increases the weight and power of the electronics subsystem.

**Assumption:** The  $\sqrt{n_d}$  increment in the SNR assumes that all of the detectors are identical in noise and responsivity. The practical result is around 10% short of the ideal.

## Multiple-Detector Scan Formats: Parallel Scene Dissection

**Parallel scanning** uses multiple sensors in cross-scan directions. For a given fixed frame time, a slower scan is used since multiple vertical lines are covered simultaneously.

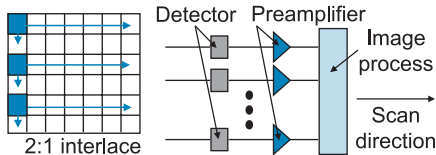
If  $n_d < VFOV/VIFOV$ , a 2D raster is required, with the scan format such that any given detector will drop  $n_d \times VIFOV$ . If there are sufficient detectors to cover a full line, only horizontal scan motion is required.



**Advantage:** Lower mirror speeds are required.

**Disadvantage:**  $D^*$  variations produce image non-uniformities.

In second-generation forward-looking infrared (FLIR) imagers, TDI/parallel scanning is used to perform 2:1 interlacing. A full line is stored and summed to the next line. Here, TDI is applied along the scan direction, and all of the detectors are preamplified, processed, and displayed.



For a system with a fixed frame time, an  $n_d$  sensor has a time line of

$$\tau_{\text{line}} = \frac{\tau_{\text{frame}}}{n_{\text{lines}}/n_d} = \tau_{\text{frame}} n_d \frac{VFOV}{VIFOV}$$

where longer dwell time is achieved by a factor of  $n_d$ , yielding

$$\tau_{\text{dwell}} = \frac{\tau_{\text{line}}}{HFOV/HIFOV} = \frac{\tau_{\text{frame}} n_d}{(VFOV/VIFOV) \cdot (HFOV/HIFOV)} = \frac{\tau_{\text{frame}} n_d}{n_{\text{pixels}}}$$

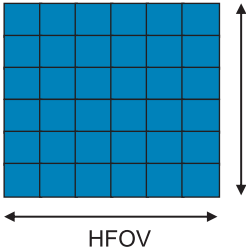
Bandwidth decreases in inverse proportion to  $n_d$ , and the noise is proportional to the square root of the bandwidth, yielding

$$\Delta f = \frac{1}{2\tau_{\text{dwell}}} = \frac{n_{\text{pixels}}}{2\tau_{\text{frame}} n_d} \Rightarrow v_n \propto \sqrt{\Delta f} = \sqrt{\frac{n_{\text{pixels}}}{2\tau_{\text{frame}} n_d}}$$

Therefore, the overall SNR increases by  $\text{SNR} \propto \sqrt{n_d}$ .

Staring Systems

**Staring systems** cover the 2D FOV in its entirety such that the number of detector elements equals the number of resolution elements in the image. As a result, the dwell time equals the frame time of the system, increasing the SNR significantly:



$$\tau_{\text{dwell}} = \tau_{\text{frame}}$$

Each detector reduces the bandwidth because of the increment in the dwell time, so the SNR increases by a factor of  $\sqrt{n_d}$ .

Non-uniformities and dead pixels are implicit in a staring array.

The SNR square root dependence can be used to compare

the potential performance of the various system configurations. For example, a  $320 \times 256$  staring array produces a SNR that is higher by a factor of 25.3 in comparison to a parallel-scanning system with a linear array of 128 detectors.

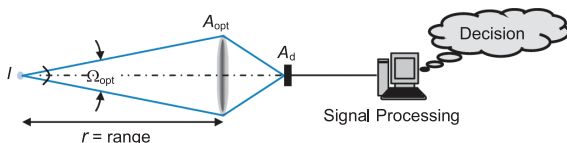
| Staring Systems                                   | Scanning Systems                                   |
|---|--|
| Good SNR  | Low SNR  |
| No moving parts                                   | Moving parts                                       |
| Uniformity problems                               | Good uniformity                                    |
| More complex electronically                       | More complex mechanically                          |
| Under-sampling problems                           | Prone to line-of-sight jitter                      |
| More prone to aliasing                            | Need more flux for a given SNR                     |
| Lower bandwidth for a given $\tau_{\text{frame}}$ | Higher bandwidth for a given $\tau_{\text{frame}}$ |
| $D^*$ for the array is lower                      | Good $D^*$ for individual detectors                |
| Expensive   | Cheaper  |

## Search Systems and the Range Equation

**Search systems** are also called **detection, warning, or go-no-go systems**. Their intent is to detect and locate a target that has a prescribed minimum intensity within a prescribed search volume. Search systems operate on an unresolved point-source basis (that does not fill the IFOV of the system); therefore, the spectral radiant intensity [W/sr·μm] is the variable of interest.

The principal concern is to assess the maximum SNR required for specified values of the probability of correct detection to minimize the false-alarm rate. The result is a statistical decision about the existence or state of a target phenomenon within a search volume. Linear fidelity is unimportant for these systems because they do not produce an image.

The objective is to establish the maximum range at which an infrared search system can detect or track a point-source target. The **range equation** states the distance at which a given point source can be detected and establishes the available design tradeoffs.



The amount of flux reaching the detector as a function of the radiant intensity is

$$\phi_d = I \cdot \Omega_{opt} \tau_{opt} \tau_{atm} = \frac{I \cdot A_{opt}}{r^2} \tau_{opt} \tau_{atm}$$

where  $\tau_{opt}$  is the optical transmittance, and  $\tau_{atm}$  is the atmospheric transmittance between the point source and the search system. The signal voltage from the detector is given by

$$v_s = \mathcal{R}_v \cdot \phi_d = \mathcal{R}_v \frac{I \cdot A_{opt}}{r^2} \tau_{opt} \tau_{atm}$$

The SNR is found by dividing each side of the equation by the rms value of the noise from the detector, yielding

$$\text{SNR} = \frac{v_s}{v_n} = \frac{\mathcal{R}_v}{v_n} \frac{I \cdot A_{opt}}{r^2} \tau_{opt} \tau_{atm}$$

## Search Systems and the Range Equation (cont.)

Using the definition of NEP, and recasting in terms of  $D^*$ ,

$$\text{SNR} = \frac{1}{\text{NEP}} \frac{I \cdot A_{\text{opt}}}{r^2} \tau_{\text{opt}} \tau_{\text{atm}} = \frac{D^*}{\sqrt{A_d \Delta f}} \frac{I \cdot A_{\text{opt}}}{r^2} \tau_{\text{opt}} \tau_{\text{atm}}$$

where  $\Delta f$  is the noise-equivalent bandwidth. Recasting in terms of the  $F/\#$  and the IFOV, and solving for the range,

$$r = \sqrt{\frac{ID^*}{\text{SNR} \sqrt{\Delta f}} \frac{\pi D_{\text{opt}}^2}{4f \sqrt{\Omega_d}} \tau_{\text{opt}} \tau_{\text{atm}}} = \sqrt{\frac{ID^*}{\text{SNR} \sqrt{\Delta f}} \frac{\pi D_{\text{opt}}}{4(F/\#) \sqrt{\Omega_d}} \tau_{\text{opt}} \tau_{\text{atm}}}$$

where  $D_{\text{opt}}$  is the diameter of the entrance pupil, and  $f$  is the effective focal length of the optics. When the range equation is used to find the maximum detection or tracking range, the SNR is the minimum required for the system to work appropriately. To analyze how the various factors affect the detection range, the range equation is regrouped in terms of optics, target and atmospheric transmittance, detector, and signal processing, respectively, yielding

$$r = \sqrt{\frac{\pi D_{\text{opt}} \tau_{\text{opt}}}{4(F/\#)}} \sqrt{I \tau_{\text{atm}}} \sqrt{D^*} \sqrt{\frac{1}{\text{SNR} \sqrt{\Omega_d \Delta f}}}$$

In the first term, the diameter, the speed of the optics, and the transmittance characterize the optics. The first two terms are written separately to facilitate their independent solutions in the tradeoff process. The range is directly proportional to the square root of  $D_{\text{opt}}$ , where the bigger the optics the more flux is collected. However, scaling up the entrance pupil changes the  $F/\#$  of the system and requires a corresponding increase in both the focal length and the linear size of the detector to maintain the original FOV.

The second term contains the radiant intensity of the target and the transmittance along the line of sight. Both the amount of attenuation caused by the atmosphere and the shot-noise contribution from the background can be optimized by choosing the best spectral band for the specific optical system. For example, if the emitting flux from the target is high, the spectral band that yields the best contrast is selected; however, if the flux is low, the spectral band that produces the optimum SNR is selected.

## Search Systems and the Range Equation (cont.)

The third factor pertains to the characteristics of the detector. The range is proportional to the square root of the normalized detectivity of the detector. Therefore, an increment in the detection range can be achieved by enhancing the sensitivity of the system using serial TDI approaches, or by effectively shielding the detector from background radiation. Also, notice that since the radiation is collected from a point source, increasing the area of the detector reduces the SNR of the system.

The final factor describes the range in terms of the signal-processing parameters. It shows that decreasing either the FOV or the noise-equivalent bandwidth slowly increases the range because of the inverse fourth root dependence. The product  $\Delta/\Omega_d$  represents the angular scan rate in steradians per second. Increasing the integration time of the system averages random noises, resulting in longer detection ranges. The SNR in this type of system is interpreted as the minimum SNR required to reach a detection decision with an acceptable degree of certainty. For example, if the search system requires a higher SNR to improve the probability of correct detection, the system will have a shorter range.

The range equation for BLIP search systems is obtained by substituting  $D_{\text{BLIP}}^*$  for  $D^*$ , which, in photon-derived units, translates to

$$r_{\text{BLIP}} = \sqrt{\frac{\pi D_{\text{opt}} \tau_{\text{opt}}}{4}} \sqrt{\tau_{\text{atm}}} I \sqrt{\frac{\lambda_{\text{cutoff}}}{hc}} \sqrt[4]{\frac{2\eta}{\pi \int_{\lambda_{\text{cuton}}}^{\lambda_{\text{cutoff}}} L_{\text{p,bkg}} d\lambda}} \sqrt{\frac{1}{\text{SNR} \sqrt{\Delta f} \sqrt{\Omega_d}}}$$

Note that the  $F/\#$  term has dropped out of the equation. Thus, a BLIP search system is influenced by the diameter of its optics but not by its speed.

Several design concepts can be used to decrease the background noise: the detector cold stop is designed to produce a 100% cold efficiency; a spectral filter is used to limit the spectral pass band to the most favorable region of the corresponding target flux; the wavelengths at which the atmosphere absorbs strongly are avoided; the emissivity of all of the optical and optomechanical components is minimized, and, if necessary, the elements by the detector's angular subtense are cooled.



## Noise-Equivalent Irradiance

The **noise-equivalent irradiance (NEI)** is one of the main descriptors of infrared warning devices. It is the flux density at the entrance pupil of the optical system that produces an output signal equal to the system's noise (i.e., SNR = 1). NEI characterizes the response of an infrared system to a point-source target.

The irradiance from a point-source target is given by

$$E = \frac{\phi}{A_{\text{opt}}} = \frac{I \cdot \Omega_{\text{opt}}}{A_{\text{opt}}} = \frac{I}{r^2}$$

Substituting the range expression and setting the SNR equal to 1,

$$\text{NEI} = E|_{\text{SNR}=1} = \frac{\sqrt{A_d \Delta f}}{A_{\text{opt}} D^* \tau_{\text{opt}} \tau_{\text{atm}}} = \frac{\text{NEP}}{A_{\text{opt}}} \frac{1}{\tau_{\text{opt}} \tau_{\text{atm}}}$$

Recasting in terms of the  $F/\#$  and IFOV,

$$\text{NEI} = \frac{4(F/\#) \sqrt{\Omega_d \Delta f}}{\pi D_{\text{opt}}^* \tau_{\text{opt}} \tau_{\text{atm}}}$$

In BLIP conditions, the NEI is independent of the  $F/\#$ , yielding

$$\text{NEI}_{\text{BLIP}} = \frac{2hc}{\lambda_{\text{cutoff}} D_{\text{opt}} \tau_{\text{opt}} \tau_{\text{atm}}} \sqrt{\frac{2\Omega_d \Delta f \int_{\lambda_{\text{cutoff}}}^{\lambda_{\text{cutoff}}} L_{\text{p,bkg}} d\lambda}{\pi \eta}}$$

NEI is especially useful when it is plotted as a function of wavelength. Such a plot defines the irradiance at each wavelength necessary to give a signal output equal to the system's rms noise. It can be interpreted either as an average value over the spectral measuring interval, or as the peak value.

Although NEI has a broader use in characterizing the performance of an entire system, it may also be used to evaluate the performance of a detector alone. In this case, it is defined as the radiant flux density necessary to produce an output signal equal to the detector noise. This term can also be used to compare the ability of differently sized sensor devices to detect a given irradiance:

$$\text{NEI} = \frac{E}{\text{SNR}} = \frac{\text{NEP}}{A_d}$$

## Performance Specification: Thermal Imaging Systems

---

A **thermal imaging system (TIS)** collects, spectrally filters, and focuses the infrared radiation onto a multi-element detector array. The detectors convert the optical signals into analog signals, which are then amplified, digitized, and processed for display on a monitor. The main function of a TIS is to produce a picture that maps temperature differences across an extended-source target; therefore, radiance is the variable of interest.

Two parameters are measured to completely specify a TIS and produce good thermal imagery: **thermal sensitivity** and **spatial resolution**. Spatial resolution indicates how small an object can be resolved by the thermal system, and thermal sensitivity concerns the minimum temperature difference discerned above noise level.

The **modulation transfer function (MTF)** characterizes both the spatial resolution and image quality of an imaging system in terms of spatial frequency response. The MTF is a major parameter used for system specifications and design analysis.

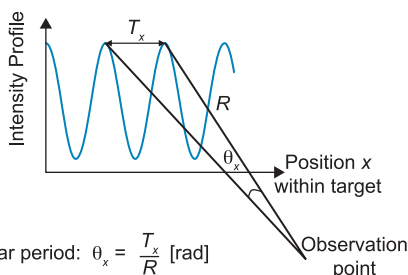
The **noise-equivalent temperature difference (NETD)** measures the thermal sensitivity of a TIS. While the NETD is a useful descriptor that characterizes the target-to-background temperature difference, it ignores the spatial resolution and image quality of the system.

The **minimum resolvable temperature difference (MRTD)** is a subjective measurement that depends on the infrared imaging system's spatial resolution and thermal sensitivity. At low spatial frequencies, the thermal sensitivity is more important, while at high spatial frequencies, the spatial resolution is the dominant factor. The MRTD combines both the thermal sensitivity and the spatial resolution into a single measurement. The MRTD is not an absolute value but is a perceivable temperature differential relative to a given background.

The **Johnson** and **TTP metric methodologies** are computer models that predict the target-acquisition range performance of modern electro-optical imaging systems.

## Modulation Transfer Function (MTF)

**Spatial frequency** is defined as the reciprocal crest-to-crest distance (i.e., the spatial period) of a sinusoidal wavefront used as a basic function in the Fourier analysis of an object or image. It is typically specified in cycles/millimeter in the image plane, and in angular spatial frequency (cycles/milliradian) in object space. For an object located at infinity, these two representations are related through the focal length  $f$  of the image-forming optical system.



$$\text{Angular period: } \theta_x = \frac{T_x}{R} \text{ [rad]}$$

$$\text{Spatial frequency: } \xi = \frac{10^{-3}}{\theta_x} \text{ [cycles/mrad]}$$

$$\xi_{\text{ang., obj}} \text{ [cycles/mrad]} = \xi_{\text{img}} \text{ [cycles/mm]} \times \frac{f \text{ [mm]}}{10^3}$$

The **image quality** of an optical or electro-optical system is characterized either by the system's **impulse response** or its Fourier transform, the **transfer function**. The impulse response  $h(x, y)$  is the 2D image formed in response

to an impulse or delta-function object. Because of the limitations imposed by diffraction and aberrations, the resulting image quality depends on the wavelength distribution of the source, the  $F/\#$  at which the system operates, the field angle at which the point is located, and the choice of focus position.

A continuous object  $f(x, y)$  is decomposed using the shifting property of delta functions into a set of point sources, each with a strength proportional to the brightness of their original object at that location. The final image  $g(x, y)$  obtained is the superposition of the individual weighted impulse responses. This is equivalent to the convolution of the object with the impulse response:

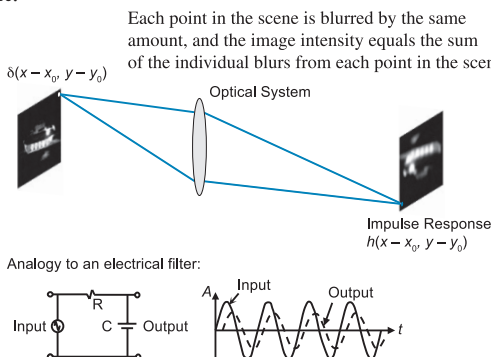
$$g(x, y) = f(x, y) ** h(x, y)$$

where the double asterisk denotes a 2D convolution.

## Modulation Transfer Function (MTF) (cont.)

The validity of this requires **linearity** and **shift invariance**; a condition called **isoplanatism**.

- Systems are linear if superposition holds: If input  $f_1(x, y)$  yields an output  $g_1(x, y)$ , and input  $f_2(x, y)$  yields an output  $g_2(x, y)$ , then the scaled and summed input  $af_1(x, y) + bf_2(x, y)$  must yield the scaled and summed output  $ag_1(x, y) + bg_2(x, y)$ .
- Linear systems are shift invariant if the output due to input  $f(x, y)$  is  $g(x, y)$ ; in this case, the output due to input  $f(x - x_0, y - y_0)$  is  $g(x - x_0, y - y_0)$ .
- Another feature of linear-shift invariant (LSI) systems is that the output contains the same frequencies as were input.



These assumptions are often violated in practice; however, to preserve the convenience of a transfer function analysis, the variable that causes nonisoplanatism is allowed to assume a set of discrete values. Each set has separate impulse responses and transfer functions. Although  $h(x, y)$  is a complete specification of image quality, additional insight is gained by use of the transfer function. A transfer-function analysis considers the imaging of sinusoidal objects rather than point objects. It is more convenient than impulse-response analysis because the combined effect of two or more subsystems can be calculated by a point-by-point multiplication of the transfer functions rather than convolving the individual impulse responses.

## Modulation Transfer Function (MTF) (cont.)

Using the convolution theorem of Fourier transforms, the product of the corresponding spectra is given by

$$G(\xi, \eta) = F(\xi, \eta) \cdot H(\xi, \eta)$$

where  $F(\xi, \eta)$  is the object spectrum,  $G(\xi, \eta)$  is the image spectrum, and  $H(\xi, \eta)$  is the transfer function, which is the Fourier transform of the impulse response.  $\xi$  and  $\eta$  are spatial frequencies in the  $x$  and  $y$  directions, respectively.

The transfer function  $H(\xi, \eta)$  is normalized to have a unit value at zero spatial frequency. This normalization is appropriate for optical systems because the transfer function of an incoherent optical system is proportional to the 2D autocorrelation of the exit pupil, and the autocorrelation is the necessary maximum at the origin. In its normalized form, the transfer function  $H(\xi, \eta)$  is referred to as the **optical transfer function (OTF)**, which plays a key role in the theoretical evaluation and optimization of an optical system as a complex function that has both a magnitude and a phase portion:

$$\text{OTF}(\xi, \eta) = |H(\xi, \eta)| \cdot e^{i\theta(\xi, \eta)}$$

The absolute value or magnitude of the OTF is the MTF, while the phase portion of the OTF is referred to as the **phase transfer function (PTF)**. The system's MTF and PTF alter the image as it passes through the system.

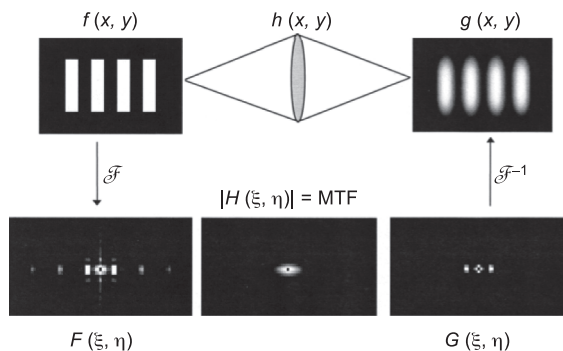


[Figure adapted from Vollmerhausen, Reago, and Driggers (2010).]

## Modulation Transfer Function (MTF) (cont.)

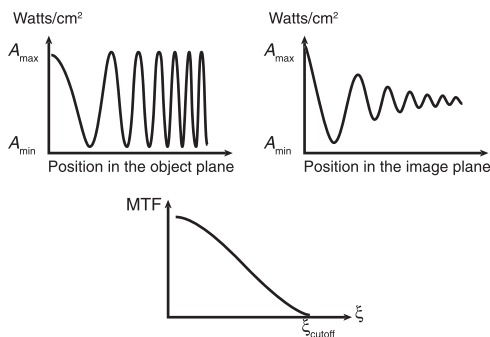
For linear phase-shift-invariant systems, the PTF is of no special interest since it indicates only a spatial shift with respect to an arbitrary selected origin. An image in which the MTF is drastically altered is still recognizable, where large nonlinearities in the PTF can destroy recognizability. PTF nonlinearity increases at high spatial frequencies. Since the MTF is small at high spatial frequencies, the linear phase-shift effect is diminished.

The MTF is then the magnitude response of the imaging system to sinusoids of different spatial frequencies. This response can also be defined as the attenuation factor in **modulation depth**:

$$M = \frac{A_{\max} - A_{\min}}{A_{\max} + A_{\min}}$$

where  $A_{\max}$  and  $A_{\min}$  refer to the maximum and minimum values of the waveform that describe the object or image in  $\text{W}/\text{cm}^2$  versus position. The modulation depth is actually a measure of visibility or contrast. The effect of the finite-size impulse response (i.e., not a delta function) of the optical system is to decrease the modulation depth of the image relative to that in the object distribution. This attenuation in modulation depth is a function of position in the image plane. The MTF is the ratio of image-to-object modulation depth as a function of spatial frequency:

$$\text{MTF}(\xi, \eta) = \frac{M_{\text{img}}(\xi, \eta)}{M_{\text{obj}}(\xi, \eta)}$$



## Optics MTF: Calculations

---

The overall transfer function of an electro-optical system is calculated by multiplying individual transfer functions of its subsystems. The majority of thermal imaging systems operate with broad spectral bandpasses and detect noncoherent radiation. Therefore, classical diffraction theory is adequate for analyzing the optics of incoherent electro-optical systems. The OTF of diffraction-limited optics depends on the radiation wavelength and the shape of the entrance pupil. Specifically, the OTF is the autocorrelation of the entrance pupil function with entrance pupil coordinates  $x$  and  $y$  replaced by spatial frequency coordinates  $\xi$  and  $\eta$ , respectively. The change of variable for the coordinate  $x$  is

$$\xi = \frac{x}{\lambda d_i}$$

where  $x$  is the autocorrelation shift in the pupil,  $\lambda$  is the working wavelength, and  $d_i$  is the distance from the exit pupil to the image plane. The image-spaced cutoff frequency with a full width  $D$  is

$$\xi_{\text{cutoff}} = \frac{1}{\lambda(F/\#)}$$

which occurs when the autocorrelation reaches zero. The same analytical procedure is performed for the  $y$  coordinate.

A system whose image has no wave aberrations and is affected only by diffraction effects is called **diffraction limited**. The OTF for such a near-perfect system is purely real and nonnegative (i.e., MTF), and represents the best performance that the system can achieve for a given  $F/\#$  and  $\lambda$ .

Consider the MTFs that correspond to diffraction-limited systems with square (width  $l$ ) and circular (diameter  $D$ ) exit pupils. When the exit pupil of the system is circular, the MTF is circularly symmetric with a  $\xi$  profile:

$$\text{MTF}(\xi) = \begin{cases} \frac{2}{\pi} \left\{ \cos^{-1}(\xi/\xi_{\text{cutoff}}) - \xi/\xi_{\text{cutoff}} \left[ 1 - (\xi/\xi_{\text{cutoff}})^2 \right]^{1/2} \right\} & \text{for } \xi \leq \xi_{\text{cutoff}} \\ 0 & \text{otherwise} \end{cases}$$

## Optics MTF: Calculations (cont.)

The square aperture has a linear MTF along the spatial frequency  $\xi$ , given by

$$\text{MTF}(\xi) = 1 - \frac{\xi}{\xi_{\text{cutoff}}}$$

The MTF curve for a system with appreciable geometric aberrations is upwardly bounded by the diffraction-limited MTF curve. Aberrations broaden the impulse response  $h(x, y)$ , resulting in a narrower, lower MTF with a smaller integrated area. The area under the MTF curve relates to the **Strehl ratio (SR)**, which measures image quality degradation and is the irradiance at the center of the impulse response divided by that at the center of a diffraction-limited impulse response. Small aberrations reduce the intensity at the principal maximum of the diffraction pattern, or the diffraction focus, and the intensity of the removed light is distributed to the outer parts of the pattern. Using the **central-ordinate theorem** for Fourier transforms, SR is written as the ratio of the area under the actual MTF curve to that under the diffraction-limited MTF curve, yielding

$$\text{SR} = \frac{\iint \text{MTF}_{\text{actual}}(\xi, \eta) d\xi d\eta}{\iint \text{MTF}_{\text{diff-limited}}(\xi, \eta) d\xi d\eta}$$

The Strehl ratio falls between 0 and 1; however, its useful range is  $\sim 0.8$  to 1 for highly corrected optical systems. Geometrical-aberration OTF is calculated from ray-trace data by Fourier transforming the spot-density distribution without regard for diffraction effects. The OTF is accurately obtained if the aberration effects dominate the impulse-response size. The OTF of a uniform blur spot is written as

$$\text{OTF}(\xi) = \frac{J_1(\pi \xi d_{\text{blur}})}{\pi \xi d_{\text{blur}}}$$

where is  $J_1(\cdot)$  the first-order Bessel function, and  $d_{\text{blur}}$  is the diameter of the blur spot. The overall optics portion MTF of an infrared system is determined by multiplying the ray-trace data MTF by the diffraction-limited MTF of the proper  $F/\#$  and wavelength.



## Detector MTF: Calculations

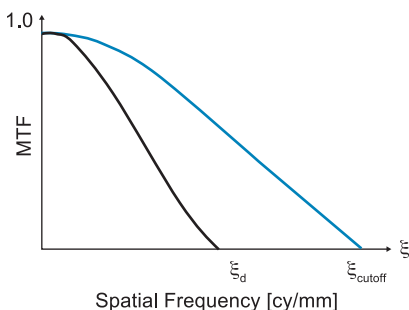
Two integral parts of modern infrared imaging systems are the electronic subsystems, which handle the signal and image processing functions, and the sensor(s) of the imaging system. Characterization of the electronic circuitry and components is well established by the temporal frequency in hertz. In order to cascade the electronic and optical subsystems, the temporal frequencies must be converted to spatial frequencies. This is achieved by dividing the temporal frequencies by the scan velocity of the imaging device. In contrast to the OTF, the electronic MTF is not necessarily maximized at the origin and can either amplify or attenuate the system MTF curve at certain spatial frequencies.

The **detector MTF** is expressed as

$$\text{MTF}_d(\xi, \eta) = \text{sinc}(d_h \xi) \text{sinc}(d_v \eta)$$

where  $d_h$  and  $d_v$  are the photosensitive detector sizes in the horizontal and vertical directions, respectively. Although the detector MTF is valid for all spatial frequencies, it is typically plotted up to its cutoff frequencies ( $\xi = 1/d_h$  and  $\eta = 1/d_v$ ). The spatial **Nyquist frequency**  $\xi_{Ny}$  of the detector array must be taken into consideration to prevent aliasing effects.

The combination of the optical and electronic responses produces the overall MTF of the system. For relatively large pixels ( $> 20 \mu\text{m}$ ), the detector MTF usually becomes the limiting factor of the electro-optical system (i.e.,  $\xi_d \ll \xi_{\text{cutoff}}$ ). As the pixels decrease in size, the detector MTF becomes less dominant.



The detector MTF is dependent solely on the detector size, while the optics MTF is dependent on the  $F/\#$  and  $\lambda$ .

### Parameter $\lambda(F/\#)/d$

Smaller detectors provide better resolution if the focal length is kept constant. However, an essential question that arises in the design of an infrared system is: What would be the smallest detector size that would still provide value in the system's performance? To answer this question, we consider the ratio of the detector sampling frequency to the optical passband limit:

$$\frac{1/d}{1/\lambda(F/\#)} = \frac{\lambda(F/\#)}{d}$$

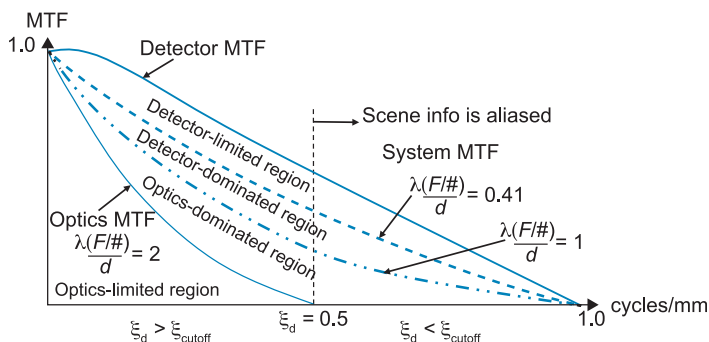
which measures the optical blur diameter relative to the detector size. There are two distinctive operational thresholds:

1. The optics-limited region occurs when

$$\frac{\lambda(F/\#)}{d} = 2 \Rightarrow d_{\text{diff}} = 4.88 \cdot d$$

2. The detector-limited region occurs when

$$\frac{\lambda(F/\#)}{d} = \frac{1}{2.44} = 0.41 \Rightarrow d_{\text{diff}} = d$$



**Example:** Find the smallest detector size for an  $F/1.2$  system operating at  $4 \mu\text{m}$  and  $10 \mu\text{m}$ , respectively.

$$d_{\text{MWIR}} = \frac{4 \cdot 1.2}{2} = 2.4 \mu\text{m} \Rightarrow d_{\text{diff}} = 11.7 \mu\text{m}$$

$$d_{\text{LWIR}} = \frac{10 \cdot 1.2}{2} = 6 \mu\text{m} \Rightarrow d_{\text{diff}} = 29.3 \mu\text{m}$$

## Motion MTF: Calculations

Motion degradation of an image can be much more severe than degradation from the optics and electronics. A quantitative characterization of **motion degradation** is essential in order to estimate the image-quality impact of these effects.

Consider a linear motion of velocity  $v$  given by the displacement function  $d = v\tau_e$ , where  $\tau_e$  is the exposure time. The MTF contribution along the linear motion is given by

$$\text{MTF}_{\text{linear}}(\xi) = |\text{sinc}(d\xi)|$$

Mechanical vibrations are a critical factor in dynamic imaging systems. A sinusoidal structural resonance can be designated as  $x = A \cdot \cos(2\pi\xi\tau_e)$ , where  $A$  is the amplitude of the oscillatory motion. The MTF degradation can be analytically described by

$$\text{MTF}_{\text{sin}}(\xi) = |J_0(2\pi A\xi)|$$

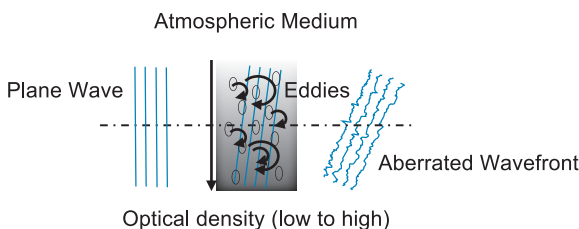
where  $J_0$  is the zero-order Bessel function.

Random motion at high temporal frequency is referred to as **jitter**, and the MTF equation associated with it is

$$\text{MTF}_{\text{random}}(\xi) = |e^{-2(\pi\sigma_a\xi)^2}|$$

where  $\sigma_a$  is the random amplitude of the jitter in milliradians. Jitter is often the limiting factor for high-resolution optics.

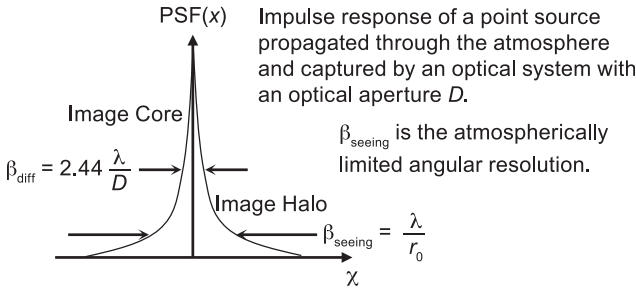
Turbulence motion results in image degradations due to random changes in the wind velocity (eddies) caused by fluctuations in the atmospheric refractive index. The cumulative effect produces angular beam deviations and creates optical distortions and aberrations.



## Atmospheric MTF: Calculations

The refractive index structure constant  $C_n^2$  is a measure of the turbulence strength. The larger the value of this constant the stronger the turbulence.  $C_n^2$  values on the order of  $\geq 10^{-13} \text{m}^{-2/3}$  produce strong turbulence, and values on the order of  $\leq 10^{-17} \text{m}^{-2/3}$  yield weak turbulence.

The **point spread function (PSF)** through the atmosphere exhibits a diffraction-limited central core and a halo.



The **Fried coherence length**  $r_0$  [cm] is defined as the diameter of a circular aperture over which the rms wavefront due to passage through the atmosphere equals one radian. Telescopes with apertures larger than  $r_0$  are limited by the atmospheric turbulence, thus preventing these optical devices from approaching diffraction-limited performance. For a plane wave,  $r_0$  can be expressed as a function of  $C_n^2$  along the path  $z$  by

$$r_0 = \left\{ 0.423 \cdot k^2 \sec(\Theta) \int_0^L C_n^2(z) dz \right\}^{-3/5}$$

where  $k = 2\pi/\lambda$  is the wave number, and  $\Theta$  is the zenith angle.

The turbulence MTF is then written as

$$\text{MTF}_{\text{tur}}(\xi) = e^{-3.44(\lambda\xi/r_0)^{5/3}}$$

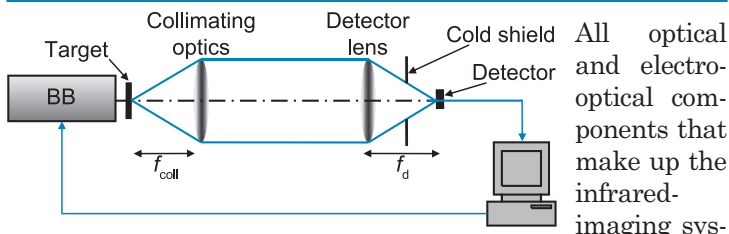
The conventional form of the aerosol MTF is given by

$$\text{MTF}_{\text{aer}}(\xi) = e^{-L[\sigma(\lambda\xi/a)^2]} \quad \text{for } \xi < a/\lambda$$

$$\text{MTF}_{\text{aer}}(\xi) = e^{-L(k\sigma)} \quad \text{for } \xi > a/\lambda$$

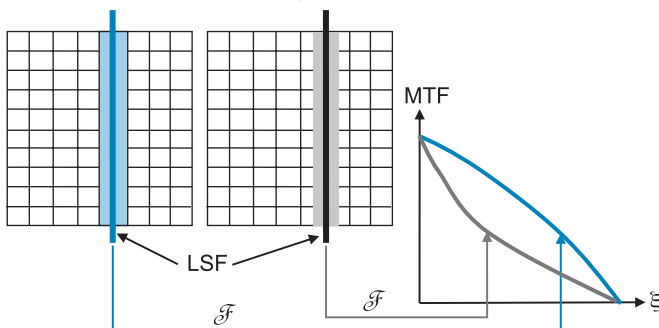
where  $\sigma$  is the **atmospheric extinction coefficient**,  $a$  denotes the size of the airborne particles ( $0.1 \text{ mm} < a < 1.0 \text{ mm}$ ), and  $L$  is the path length.

## MTF Measurement Setup and Sampling Effects



system should be placed on a vibration-isolated optical table. The aperture of the collimator should be large enough to overfill the aperture of the system under test. The optical axis of the infrared camera must be parallel to and centered on the optical axis of the collimator to ensure that its entrance pupil is perpendicular to the collimator optical axis. The display gain and brightness should be optimized prior to the start of the MTF measurement to assure that the display setting does not limit the performance of the detector array.

**Sampling effects** alter the MTF and affect the fidelity of the image. The discrete location of the detectors in the staring array creates the sampling lattice. **Phasing effects** between the sampling lattice and the location of the target introduce problems at nearly all spatial frequencies. **Digitization** alters signal amplitude and distorts the pulse shape. Sampling causes sensor systems like **focal plane arrays (FPAs)** to have a particular kind of shift variance (i.e., spatial phase effects), in which case, they depend on the position of the target relative to the sampling grid to measure the MTF of the system.



(LSF is line spread function; see next page.)

## MTF Measurement Techniques: Point Spread Function and Line Spread Function

---

Different measurement techniques can be used to assess the MTF of an infrared imaging system. These include the measurement of different types of responses such as point spread function, line spread function, edge spread function, sine-wave target response, square-wave target response, and noise-like target response. All targets, except for those that are random, should be placed in a micro-positioning mount containing three degrees of freedom ( $x$ ,  $y$ ,  $\theta$ ) to account for phasing effects.

The imaging of a point source  $\delta(x,y)$  of an optical system has an energy distribution called the **point spread function (PSF)**. The 2D Fourier transform of the PSF yields the complete 2D OTF( $\xi$ ,  $\eta$ ) of the system in a single measurement. The absolute value of the OTF gives the MTF of the system. The impulse response technique is practically implemented by placing a small pinhole at the focal point of the collimator. If the flux passing through the pinhole produces a SNR that is below a usable value, a slit target can be placed at the focal plane of the collimating optics; the output is called the **line spread function (LSF)**. The cross-section of the LSF is obtained by integrating the PSF parallel to the direction of the line source because the line image is simply the summation of an infinite number of points along its length. The LSF only yields information about a single profile of the 2D OTF. Therefore, the absolute value of the Fourier transform of the LSF yields the 1D MTF( $\xi$ ,  $\eta$ ) of the system.

To obtain other profiles of the MTF, the line target can be reoriented as desired. The slit angular subtense must be smaller than the IFOV with a value of 0.1 IFOV. The phasing effects are tested by scanning the line target relative to the sampling sensor grid until maximum and minimum signals are obtained at the sensor. The measurements are performed and recorded at different target positions, and averaging the output over all locations yields an average MTF. However, this average MTF is measured using a finite-slit aperture, so this undesirable component is removed by dividing out the Fourier transform of the finite slit, yielding a more accurate MTF.

## MTF Measurement Techniques: Edge Spread Function and Contrast Transfer Function

The MTF is also obtained from an **edge spread function (ESF)**, the response of the system under test (SUT) to an illuminated knife-edge target. There are two advantages to using this target over the line target: it is simpler to build than a narrow slit, and there is no MTF correction. The edge is differentiated to obtain the line spread function and is then Fourier transformed. However, the derivative operation accentuates the system noise presented in the data, which can corrupt the resulting MTF. The edge must be straight with no raggedness. To increase the SNR for both the line spread and edge spread techniques, the 1D Fourier transform is averaged over all rows of the image. In addition, reducing the system gain reduces noise, and the target signal can be increased if possible.

The MTF is also obtained by measuring the system's response to a series of sine-wave targets, where the image modulation depth is measured as a function of spatial frequency. Sinusoidal targets can be fabricated on photographic films or transparencies for the visible spectrum; however, they are not easy to fabricate for testing infrared systems due to materials limitations. A less expensive, more convenient target is the bar target, a pattern of alternating bright and dark bars of equal width. The square-wave response is called the **contrast transfer function (CTF)** and is a function of the **fundamental spatial frequency**  $\xi_t$  of the specific bar target under test. The CTF is measured on the peak-to-valley variation of the image irradiance and is defined as

$$\text{CTF}(\xi_t) = \frac{M_{\text{square-response}}(\xi_t)}{M_{\text{input-square-wave}}(\xi_t)}$$

The CTF is higher than the MTF at all spatial frequencies because of the contribution of the odd harmonics of the infinite-square-wave test pattern to the modulation depth in the image. The CTF is expressed as an infinite series of MTFs. A square wave can be expressed as a Fourier-cosine series. The output amplitude of the square wave at frequency  $\xi_t$  is an infinite sum of the input cosine amplitudes modified by the system's MTF:

## MTF Measurement Techniques: Edge Spread Function and Contrast Transfer Function (cont.)

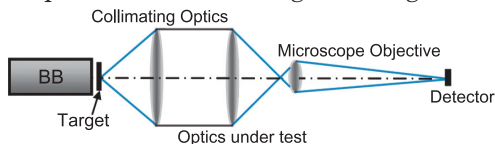
$$\text{CTF}(\xi_t) = \frac{4}{\pi} \left[ \text{MTF}(\xi_t) - \frac{1}{3} \text{MTF}(3\xi_t) + \frac{1}{5} \text{MTF}(5\xi_t) - \frac{1}{7} \text{MTF}(7\xi_t) + \dots \right]$$

Conversely, the MTF can be expressed as an infinite sum of CTFs as

$$\text{MTF}(\xi_t) = \frac{\pi}{4} \left[ \text{CTF}(\xi_t) + \frac{1}{3} \text{CTF}(3\xi_t) - \frac{1}{5} \text{CTF}(5\xi_t) + \frac{1}{7} \text{CTF}(7\xi_t) - \dots \right]$$

Optical systems are characterized with three- and four-bar targets and not by infinite square-wave cycles. Therefore, the CTF might be slightly higher than the CTF curve for an infinite square wave. For bar targets with a spatial frequency above one-third of the cutoff frequency, where the MTF approaches zero, the MTF equals  $\pi/4$  times the measured CTF. Electronic nonlinearity, digitization effects, and sampled-scene phase effects can make these MTF and CTF measurements difficult.

The MTF of optics is measured, without including the detector MTF, by placing a microscope objective in front of the detector FPA. The microscope objective is used as a relay lens to reimage the system's response formed by the optics under test onto the FPA with the appropriate magnification. Here, the detector is no longer the limiting component of the imaging system, since its MTF response becomes appreciably higher than the optical MTF curve. The microscope objective must be of high quality to reduce degradation of the measured response function and have a NA that is high enough to capture the entire image-forming cone angle.



Imaging systems containing a detector FPA are nonisoplanatic, and their responses depend on the location of the deterministic targets relative to the sampling grid, introducing problems at nearly all spatial frequencies. The use of random-target techniques for measuring the MTF of a digital imaging system tends to average out the phase effects.



## MTF Measurement Techniques: Noise-like Targets

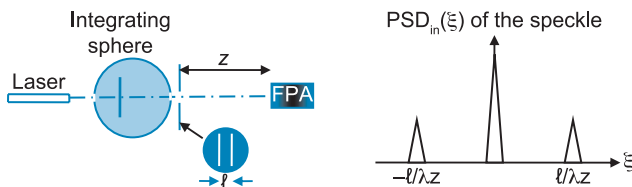
Using noise-like test targets of known spatial frequency content allows measurement of the shift-invariant MTF because the target information is positioned randomly with respect to the sampling sites of the digital imaging system. The MTF of the system is calculated because the input power density  $\text{PSD}_{\text{input}}(\xi)$  of the input random pattern is known, and an accurate estimate of the output power density  $\text{PSD}_{\text{output}}(\xi)$  is made from the FPA response. The MTF is then calculated from the following relationship:

$$\text{MTF}(\xi) = \sqrt{\frac{\text{PSD}_{\text{output}}(\xi)}{\text{PSD}_{\text{input}}(\xi)}}$$

This approach is commonly used to characterize time domain electrical networks, and its application to the MTF testing of digital imaging systems provides an average of the shift variation, which eases alignment tolerances and facilitates MTF measurements at spatial frequencies beyond the Nyquist frequency.

Two different techniques are used for the generation of random targets: laser speckle and transparency-based noise targets. The former is used to characterize the MTF of FPAs alone, while the latter is used to characterize the MTF of a complete imaging system (i.e., imaging optics together with the FPA).

A laser speckle pattern of known PSD is generated by the illustrated optical train.

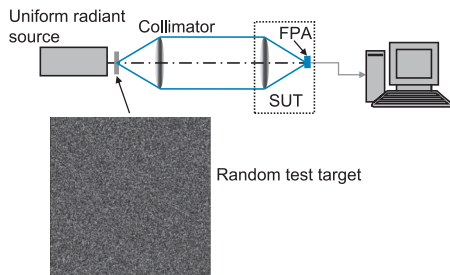


The integrating sphere produces a uniform irradiance with a spatially random phase. The aperture following the integrating sphere (typically, a double slit), determines the  $\text{PSD}_{\text{input}}(\xi)$  of the speckle pattern at the FPA, which is proportional to the aperture transmission function.

## MTF Measurement Techniques: Noise-like Targets (cont.)

The spatial frequency of the resulting narrowband speckle pattern can be tuned by changing the aperture-to-focal-plane distance  $z$ . The MTF is calculated from the relative strength of the sideband center of the  $\text{PSD}_{\text{output}}(\xi)$ .

To characterize a complete imaging system, a 2D uncorrelated random pattern with uniform band-limited white-noise distribution is created using a random generator computer algorithm. This random gray-level pattern is printed onto a transparency and placed in front of a uniform radiant extended source, producing a 2D radiance pattern with the desired input power spectrum  $\text{PSD}_{\text{input}}$ .



The output spectral density is estimated by imaging the target through the optical system onto the FPA. The output data is then captured by a frame grabber and processed to yield the output power spectrum  $\text{PSD}_{\text{output}}(\xi)$  as the absolute value squared of the Fourier transform of the output image data. The MTF is then calculated using the equation on the previous page.

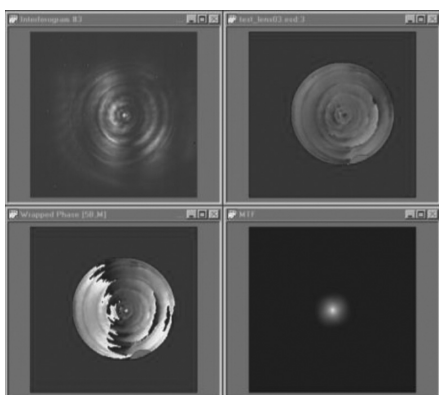
In the infrared region, the transparency must be replaced by a random thermoscene made of a chrome deposition on an infrared material substrate. Microlithographic processes enable production of square apertures of various sizes on a 2D matrix to achieve the desirable random pattern. To avoid diffraction-induced nonlinearities of transmittance, the minimum aperture size must be five times the wavelength.

## MTF Measurement Techniques: Interferometry

**Common-path interferometers** may be employed for measuring the transfer functions of optical systems. An interferogram of the wavefront exiting the system is reduced to find the phase map. The distribution of amplitude and phase across the exit pupil contains the necessary information for calculating the OTF by pupil autocorrelation.

The performance of a lens at specific conjugates can be measured by placing the optical element in one of the arms of an interferometer. The process begins by computing a single wrapped phase map from the resultant wavefront information or **optical path difference (OPD)** exiting the pupil of the system under test.

The wrapped phase map is represented in multiples of  $2\pi$  with phase values ranging from  $-\pi$  to  $\pi$ . Removal of the  $2\pi$  modulus is accomplished by using an unwrapping algorithm, thus producing an unwrapped phase map also known as the surface map. The PSF is obtained by multiplying the



conjugate Fourier transform of the surface map data (i.e., element-by-element multiplication of the amplitude complex function). The inverse Fourier transform of the PSF yields the complex OTF with the modulus that corresponds to the MTF of the optical system.

In summary, the MTF is a powerful tool used to characterize an imaging system's ability to reproduce signals as a function of spatial frequency. It is a fundamental parameter that determines (1) where the limitations of performance in optical and electro-optical systems occur, and (2) which crucial components must be enhanced to yield a better overall image quality. MTF guides system design and predicts system performance.

## Noise-Equivalent Temperature Difference (NETD)

**Noise-equivalent temperature difference (NETD)** is the target-to-background temperature difference that produces a peak signal-to-rms-noise ratio of unity. Its analytical formula is given by

$$\text{NETD} = \frac{[4(F/\#)^2 + 1]\sqrt{\Delta f}}{\pi\tau_{\text{atm}}\tau_{\text{opt}}D^*\sqrt{A_d}(\partial L/\partial T)}$$

where  $\Delta f$  is the electronic bandwidth,  $D^*$  and  $A_d$  are the normalized detectivity and the effective area of the detector, respectively, and the partial derivative of the radiance with respect to temperature is the radiance contrast. This equation applies strictly to detector-limited situations.

A smaller NETD indicates better thermal sensitivity. For the best NETD,  $D^*$  is peaked near the wavelength of maximum exitance contrast of the source. A smaller  $F/\#$  collects more flux, yielding a more accurate estimated NETD. A smaller electronic bandwidth yields a larger integration time, producing a smaller noise voltage and lowering the NETD. A larger detector area gives a larger IFOV, collecting more flux and resulting in a better NETD. The drawback of NETD as a system-level performance descriptor is that, while the thermal sensitivity improves for larger detectors, the image resolution deteriorates. Thus, although the NETD is a sufficient operational test, it cannot be applied as a design criterion.

When the system operates under BLIP conditions, the equation for NETD becomes

$$\text{NETD}_{\text{BLIP}} = \frac{2\sqrt{2}}{\pi\tau_{\text{atm}}\tau_{\text{opt}}} \frac{hc}{\lambda_{\text{cutoff}}} \frac{F/\#}{(\partial L/\partial T)} \sqrt{\frac{\Delta f \int_{\lambda_{\text{cutoff}}}^{\lambda_{\text{cutoff}}} L_{\text{p, bkg}} d\lambda}{\eta A_d}}$$

where  $\lambda$  is the wavelength,  $h$  is Planck's constant,  $c$  is the speed of light in vacuum,  $L_{\text{p, bkg}}$  is the background radiance, and  $\eta$  is the quantum efficiency of the detector. Notice that the NETD is inversely proportional to the square root of the quantum efficiency and proportional to the square root of the in-band background flux. Under BLIP conditions, the NETD has a linear dependence on the  $F/\#$  rather than a square dependence, as in the detector-limited condition case.

## NETD of Microbolometers

While infrared photon detectors are subject to BLIP conditions, **microbolometers** are limited by temperature and background fluctuations according to

$$\text{NETD}_{\text{TF}} = \frac{2T_d[4(F/\#)^2 + 1]\sqrt{kK\Delta f}}{\pi\tau_{\text{atm}}\tau_{\text{opt}}\epsilon A_d(\partial L/\partial T)}$$

$$\text{NETD}_{\text{BF}} = \frac{[4(F/\#)^2 + 1]\sqrt{8kK\Delta f(T_d^5 + T_{\text{bkg}}^5)}}{\pi\tau_{\text{atm}}\tau_{\text{opt}}\sqrt{\epsilon A_d}(\partial L/\partial T)}$$

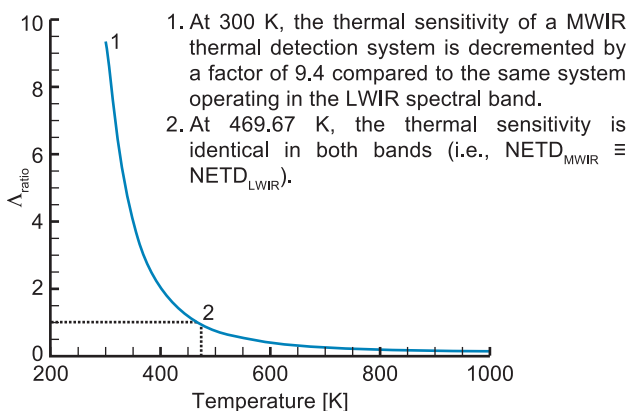
where  $k$  is Boltzmann's constant, and  $K$  is the thermal conductance in Joules/K.

**Example:** Compare the thermal sensitivity of a microbolometer when operating in the 3- to 5- $\mu\text{m}$  and 8- to 12- $\mu\text{m}$  spectral regions. The sensor is viewing a Lambertian source whose temperature ranges from 300 to 1000 K. Assume 100% transmittance.

In the case of a thermal detector, all of the parameters in the NETD equations (including  $D^*$ ) are independent of the spectral response except for  $\partial M/\partial T$ , in which case,

$$\Lambda_{\text{ratio}} = \frac{\text{NETD}_{\text{MWIR}}}{\text{NETD}_{\text{LWIR}}} = \frac{(\partial M/\partial T)_{\text{LWIR}}}{(\partial M/\partial T)_{\text{MWIR}}}$$

A plot of this ratio as a function of temperature is shown below.

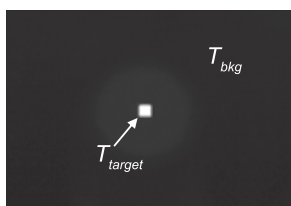


## NETD Measurement Technique

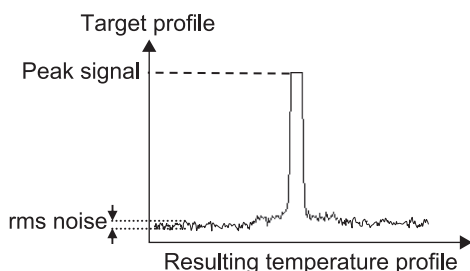
The NETD measurement is usually carried out using a square target. The size of the square must be several times the detector angular substance (i.e., several IFOVs) of the extended source to ensure that the spatial response of the system does not affect the measurement. This target is usually placed in front of an extended-area blackbody source, so that the temperature difference between the square target and the background is several times the expected NETD to ensure a response that is clearly above the system noise. The peak signal and rms noise data are obtained by capturing, averaging, and taking the standard deviation of several images. The NETD is then calculated from the experimental data as follows:

$$\text{NETD} = \frac{\Delta T}{\text{SNR}}$$

where  $\Delta T = T_{\text{target}} - T_{\text{bkg}}$ , and the SNR is the signal-to-noise ratio of the thermal system.



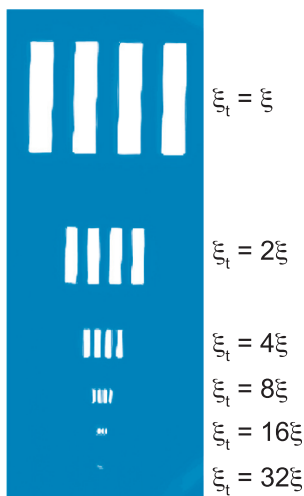
NETD test imaged pattern



Care must be taken to ensure that the system is operating linearly and that no noise sources are included. Because of the dependence of noise on bandwidth, and to obtain the proper integration time and bandwidth, the NETD must be measured with the system running at its full operational scan rate.

## Minimum Resolvable Temperature Difference (MRTD)

The **minimum resolvable temperature difference (MRTD)** simultaneously characterizes both the spatial resolution and the thermal sensitivity. It is a subjective measurement for which the SNR-limited thermal sensitivity



is outlined as a function of spatial frequency. Conceptually, the MRTD is the image SNR required for an observer to resolve four-bar targets at several **fundamental spatial frequencies**  $\xi_t$  so that the bars are just discernable by a trained observer with unlimited viewing time. The noise-limited rationale is essential in this case because an infrared imaging system displays its utmost sensitivity when the highest noise is visible to the observer (i.e., gain is increased to compensate for adverse atmospheric and/or scene conditions).

These tests depend on decisions made by the observer. The results vary with training, motivation, and visual capacity, as well as the environmental setting. Because of the considerable inter- and intra-observer variability, several observers are required. The underlying distribution of observer responses must be known, so that the individual responses can be appropriately averaged.

MRTD is a better system-performance descriptor than the MTF alone because the MTF measures the attenuation in modulation depth without regard for a noise level. MRTD is also a more complete measurement than the NETD because it accounts for both spatial resolution and noise level. Therefore, the MRTD is a useful overall analytical and design tool that is indicative of system performance.

## MRTD: Calculation

MRTD measures the ability to resolve detail in imagery and is directly proportional to the NETD and inversely proportional to the MTF:

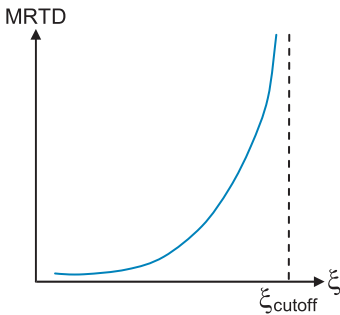
$$\text{MRTD} \propto \frac{\text{NETD} \xi_t \sqrt{\text{HIFOV} \cdot \text{VIFOV}}}{\text{MTF}(\xi_t) \sqrt{\tau_{\text{eye}} \cdot \tau_{\text{frame}}}}$$

where  $\xi_t$  is the spatial frequency of the target being observed,  $\tau_{\text{eye}}$  is the integration time of the human eye,  $\tau_{\text{frame}}$  is the frame time, MTF is the transfer function of the system at that particular target frequency, and HIFOV and VIFOV are the horizontal and vertical IFOVs of the system, respectively.

The derivation of an exact analytical expression for MRTD is complex because of the number of variables in the calculation; therefore, computer-aided performance models such as the Night Vision Integrated Performance Model (NVIPM) are used. Substituting the NETD equation into the MRTD equation yields

$$\text{MRTD} \propto \frac{\xi_t \sqrt{\text{HIFOV} \cdot \text{VIFOV}}}{\text{MTF}(\xi_t) \sqrt{\tau_{\text{eye}} \cdot \tau_{\text{frame}}}} \times \frac{(F/\#)^2 \sqrt{\Delta f}}{D^* \sqrt{A_d} \partial L / \partial T}$$

MRTD depends on the same variables as NETD (i.e.,  $F/\#$ ,  $\Delta f$ ,  $D^*$ , and radiance contrast). However, the thermal performance of the system cannot be increased by increasing the area of the detector or IFOV; the MTF decreases at higher frequencies. Therefore, the amount of  $\Delta T$  required for a four-bar target to be discernable increases as the size of the bars decreases. The MRTD increases when MTF decreases, but the MRTD

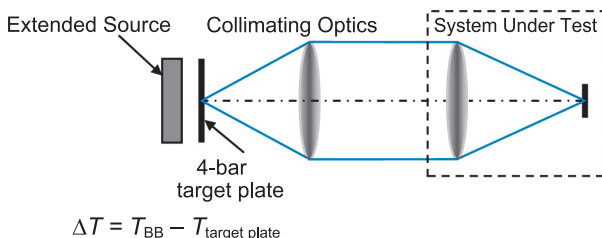


increases more rapidly due to the extra factor  $\xi_t$  in the numerator. The effect of the observer is included in the factor  $\tau_{\text{eye}} \tau_{\text{frame}}$ . Increasing the frame rate gives more observations within the temporal integration time of the human eye, and then the eye-brain system tends to average out some of the noise, leading to a lower MRTD.



## MRTD Measurement Technique

A generic MRTD test configuration is shown:



The four-bar target is located in front of the blackbody source at the focal plane of the collimator to collimate the radiation from each point of the surface of the target. To achieve high spatial frequency, the MRTD setup is mounted on a vibration-isolated optical table. Since the MRTD is a detection criterion for noisy imagery, the gain of the infrared imaging system must be set high enough that the image is noisy. Infrared imaging systems are subject to sampling effects. The MRTD does not have a unique value for each spatial frequency, but has a range of values depending on the location of the target with respect to the detector array. Therefore, the targets must be adjusted to achieve the best visibility. An observer must count the number of bars to ensure that all four are present and discernable. The targets should range from low spatial frequencies to just past the system cutoff, and should span the entire spatial frequency response.

Problems associated with MRTD measurements include the related distance between the display screen and the observer, background brightness, and strain. The contrast sensitivity increases with background radiance; however, during MRTD tests, the observer can adjust the system's gain and level, and monitor the brightness and contrast to optimize the image for detection criterion. Inconsistencies between the results obtained by different observers can occur, and over a long period of time, the human eye-brain sensitivity decreases, causing unreliability. The use of the MRTD is also somewhat limited because all of the field scenes are spectrally selective (i.e., emissivity is a function of wavelength), while most MRTD tests are performed with extended-area blackbodies.

## MRTD Measurement: Automatic Test

It is of practical interest to measure the MRTD without the need of a human observer. Automatic tests or objective tests are desirable because of an insufficient number of trained personnel and because the subjective test is time consuming. The MRTD equation can be written as

$$\text{MRTD} = \mathcal{K}(\xi_t) \frac{\text{NETD}}{\text{MTF}(\xi_t)}$$

where the constant of proportionality and any spatial-frequency-dependent terms, including the effect of the observer, are taken up into the function  $\mathcal{K}(\xi_t)$ . To characterize the average effects of the observer for a given display and viewing geometry, an MRTD curve is measured for a representative sample of the system under test. Along with the MRTD data, the NETD and MTF are measured and recorded for the system. From these data, the function  $\mathcal{K}(\xi_t)$  can be determined, and subsequent tests of similar systems can be performed without the observer.

A comprehensive automatic laboratory test station, which provides the means to measure the performance of an infrared imaging system, and a field-tester apparatus measuring the FLIR parameters of an Apache helicopter are shown below.



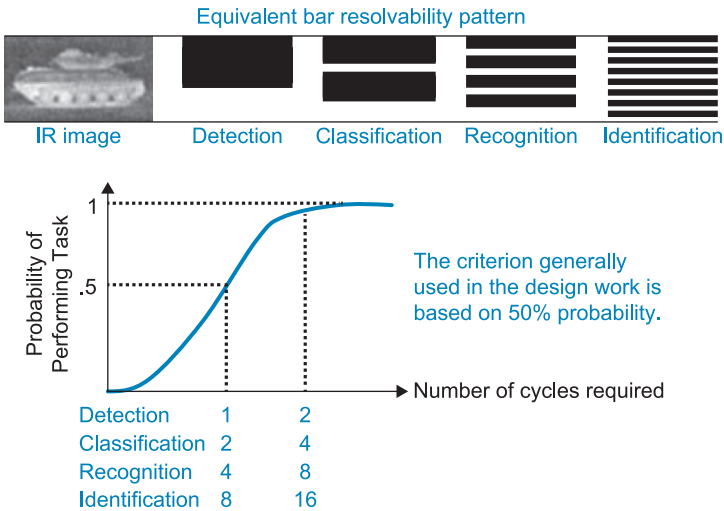
Photographs courtesy of CI Systems, Inc.

### Johnson Metric Methodology

The **Johnson metric** is a metric in a computer model that accounts for both the thermal sensitivity and the spatial resolution of a thermal imaging system. It provides a way to describe real targets in terms of simpler square-wave visual patterns.

Johnson placed sets of square-wave patterns with a selection of bar widths alongside eight military targets and a man. These square arrangements have the same apparent temperature difference  $\Delta T$  as the military targets and are viewed under the same conditions. When it was determined that a particular target could be detected, classified, recognized, or identified, the corresponding just-resolved bar target of the set was noted as well. Johnson concluded that it is possible to characterize the performance of an average observer for a particular decision task in terms of the number of just-resolved cycles that would fit across the minimum dimensions of the target.

Normalizing the number of cycles in the bar pattern by the minimum dimension of the target, it was found that the spatial resolution required for a particular decision task was approximately constant.

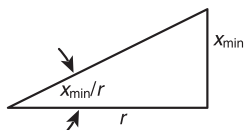


### Johnson Metric Methodology (cont.)

A more complex decision task requires a higher level of detail, and hence a finer image resolution is necessary. These resolutions are based on a 50% probability of correctly determining the level of discrimination.

Once the required numbers of cycles for a particular task are determined, the required angular spatial frequency in cycles/radian is calculated by

$$\xi = \frac{n_{\text{cycles}}}{x_{\text{min}}/r}$$



where  $n_{\text{cycles}}$  is the number of cycles,  $x_{\text{min}}$  is the minimum target dimension,  $r$  is the range, and, therefore,  $x_{\text{min}}/r$  is the angular subtense of the target.

To discriminate a target with 50% probability, two IFOVs are required per cycle of the highest spatial frequency (i.e., corresponding to one cycle on target). Therefore, we can write the IFOV in terms of the Johnson parameters:

$$\begin{aligned} \frac{1}{2 \times \text{IFOV}} &= \frac{n_{\text{cycles}}}{x_{\text{min}}/r} = \frac{f}{2\sqrt{A_d}} \\ \Rightarrow \frac{f}{\sqrt{A_d}} &= \frac{2r(N50)}{x_{\text{min}}} \end{aligned}$$

where  $f$  is the effective focal length of the optical system, and  $A_d$  is the area of the detector. Johnson determined that the N50 values needed to predict the discrimination of the target with 50% probability are 1, 4, and 8 cycles for detection, recognition, and identification, respectively. However, these values were never explicitly defined, and other values can be experimentally determined.

The Johnson methodology multiplies the resolving power of an imager [cycles/milliradian] by the target size [milliradian] to get the number of cycles (N50) on target. These values were established without removing the effect of chance.

## Johnson Criteria Flaws

---

In the Johnson methodology, sensor spatial frequency at a particular temperature characterizes the sensor for target acquisition purposes. The performance of the imager can be determined exclusively by the Johnson frequency  $\xi_J$  visible at the average target-to-background contrast. When the Johnson method works, it is because an increase in  $\xi_J$  represents an improvement in the contrast rendition at all spatial frequencies. However, with FPAs,  $\xi_J$  is more an indicator of sample rate than of image quality. In addition, the Johnson metric fails to accurately predict the effect of noise on task performance. The observer appears to require more sensor resolution when the resolution is noise limited as opposed to spatial-frequency-response limited. Also, because the Johnson metric is based on the system response at a single frequency, it cannot predict the effect of varying the image frequency spectrum through digital processing.

Due to Johnson methodology insensitivities to sampled imager characteristics in the vicinity of the limiting frequency, the Johnson metric is fundamentally flawed. These flaws make predictions for many modern imaging systems inaccurate.

The Night Vision and Electronic Sensors Directorate (NVESD) of the U.S. Army has developed a new target acquisition metric to better predict the performance of modern electro-optical imagers. The targeting task performance (TTP) metric provides better accuracy than the Johnson criteria. The TTP methodology extends the capabilities of the Johnson model to sampled imagers and digital image enhancement. For example, the TTP metric can be applied in circumstances where the sensor noise is not white (i.e., spectrally weighted). This means that, unlike the Johnson criteria, the TTP metric accurately predicts the performance of digital image enhancements such as high-frequency boost. The contrast limitation of vision is incorporated into the TTP metric model as well, thus allowing the modeling of image intensifiers, CCDs, CMOS, and thermal FPAs.

## Targeting Task Performance (TTP) Metric Methodology

---

The computer model presented in this section was developed by the Night Vision and Electronic Sensors Directorate (NVESD).

A scene consists of many luminance levels. The eye achieves an integrated view of objects connecting lines and surfaces. These lines and surfaces do not share particular brightness through their extent. Perspective is gained from converging lines that might vary in both sharpness and luminance with increasing range. Slight changes in hue or texture can provide hints as to the distance and orientation of an object, and possibly indicate the nature of the surface attributes. The discrimination of a target requires the ability to distinguish small differences in shades of gray, and not just the ability to identify black symbols on a white background (i.e., acute vision). A quantification of visual performance requires that the resolution be measured for all shades of gray in the image.

An imager provides advantages over human sight. The target can be magnified, and the imager allows the viewer to perceive radiation beyond the visible spectrum. However, aberrations and noise associated with the imager limit the viewer's performance. Also, human vision performance depends on display luminance and contrast.

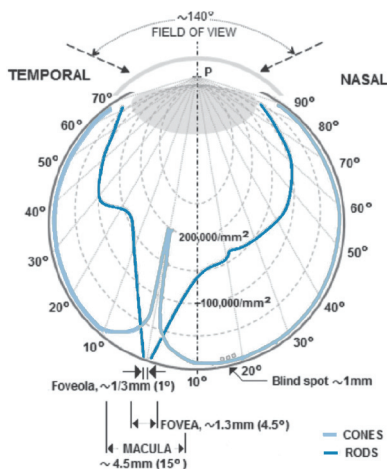
The TTP model takes into consideration hardware characteristics and human vision. These interactions establish how well the scene is perceived through the imager and how well the observer is able to discriminate targets. It predicts the effects of blur, noise, contrast, and display characteristics on target acquisition and range performance.

The Night Vision Integrated Performance Model (NV-IPM) is a TTP-based metric software code that provides widespread engineering analysis for the design and development of imaging systems. The NV-IPM combines all of the previous software versions of NVESD imager performance models into a single package.

## Human Vision: Distribution of Retinal Photoreceptors

The limitations of human vision are important when predicting the target performance of an electro-optical sensor. The three modes of eye function under different illuminance levels—**photopic** (bright light), **scotopic** (low light) and **mesopic** (intermediary light), result from the specific response of the eyes' two types of photoreceptor cells, **cones** and **rods**. The photoreceptor cells' activity is specific to the retinal illuminance level, which is determined by the brightness level of the object observed, as well as the brightness of the background and surroundings.

Rods cannot distinguish colors, but are responsible for scotopic monochrome (black-and-white) vision; they work well in dim light but saturate at illumination levels above 10 fL (footlamberts). Rods are distributed throughout the retina, except at the fovea and the blind spot. Rod density is greater in the peripheral retina than in the central retina. Cones are responsible for color vision and cease to be important below 0.01 fL. They are mostly concentrated in and near the fovea, and only a few are present at the sides of the retina. With adequate illumination, objects are seen most sharply when their images fall on or near the fovea, as in the case when one looks directly at an object. When rods and cones are stimulated by light, the nerves send off impulses to the brain.

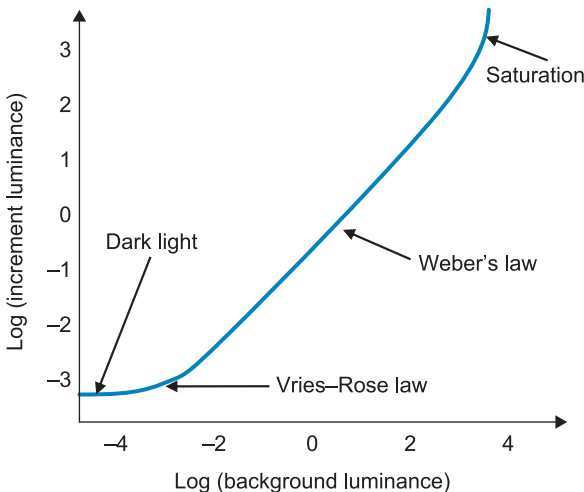


## Human Vision: Response and Sensitivity

Eye behavior changes significantly with luminance and with angular eccentricity from the fovea.

The sensitivity of the eye is measured by determining the absolute intensity threshold, (i.e., the increment luminance  $\Delta L$ ) of a small disk of light against a uniform background.

The eye response to signal luminous intensity is logarithmic for the most part according to **Weber's law**, which states that the ratio of the increment signal to the background signal at threshold is constant. The response changes for very high-level stimuli due to saturation and for very low-level stimuli due to the increased role of neural noise (dark light). At very low-brightness levels, rod response follows the square root law (de Vries–Rose law), which is limited by quanta fluctuation.



Sometimes display luminance is kept low because the operator chooses to maintain dark adaptation. For example, during night flight, military pilots flying without goggles set instrumentation displays to between 0.1 to 0.3 fL. This permits reasonable viewing of the instruments while maintaining dark adaptation in order to see outside the aircraft.

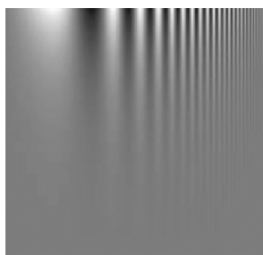


## Contrast Threshold Function (CTF)

While MRTD describes resolution and noise limitations of an imaging system, there are also limitations associated with human vision. Our ability to discern low-contrast patterns varies with the size of the pattern, or its spatial frequency. The **contrast threshold function (CTF)** is a measure of the minimum contrast needed to discern the presence of a sinusoidal pattern at a given spatial frequency.

Each individual has a different  $CTF_{eye}$  curve. Relatively speaking, higher amounts of minimum contrast are needed at extremely low and extremely high spatial frequencies.

$CTF_{eye}$  is similar to the MRTD function used to characterize infrared systems. The observer views sinusoidal patterns on an electronic display spanning different frequencies with constant illumination while the contrast is lowered until the observer is unable to discern the sine-wave patterns.



In this image, the spatial frequency increases from left to right, and contrast varies from 100% at the top to less than 1% at the bottom. Since human perception of contrast is frequency dependent, the alternating bars in the middle appear taller.

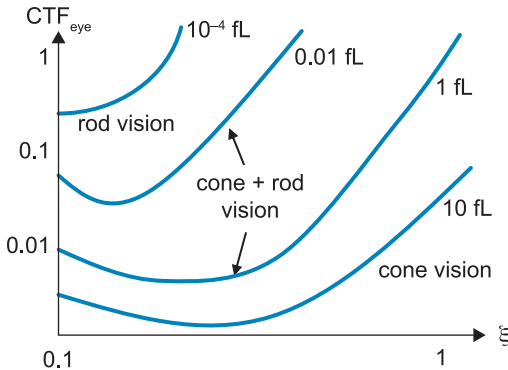
The contrast of an object or its representation in an image is found by comparing the maximum and minimum visual luminance  $L_v$  values:

$$\text{Contrast} = \frac{L_{v,\max} - L_{v,\min}}{L_{v,\max} + L_{v,\min}}$$

The denominator represents twice the average value of the luminance. This contrast ratio has a tremendous impact on the overall image quality. A higher contrast significantly increases the amount of image content conveyed to the human observer.

### Contrast Threshold Function (CTF) (cont.)

The  $CTF_{eye}$  curve provides the threshold contrast value at all spatial frequencies.



The limiting resolution is the spatial frequency  $\xi$  where the  $CTF_{eye}$  curve crosses unity contrast. It provides the smallest detail that will be visible at that light level, and this detail is only visible at the highest possible contrast. The eye loses the ability to see small contrast changes at high frequency as cone vision is lost. The  $CTF_{eye}$  curve rises as light level decreases, resulting in lower limiting resolution and loss of the ability to see small contrast differences at any spatial frequency. For luminance levels above 0.01 fL, people have better threshold vision at middle spatial frequencies than at low and high spatial frequencies.

The contrast threshold function in the presence of external noise ( $CTF_n$ ) is found empirically by

$$CTF_n^2 = \kappa(N^2 + N_{eye}^2)$$

where  $N$  and  $N_{eye}$  are sensor and eye noises, respectively, and  $\kappa$  is a calibration factor fitted to experimental data.

$CTF_n$  is the contrast threshold function of the sensor–eye system, assuming that the sensor has a MTF of one for all of the spatial frequencies that can be seen by the eye. As with naked-eye vision,  $CTF_n$  depends on the radiation level and spatial frequency.

### Contrast Threshold Function (CTF) (cont.)

Setting  $N = 0$ ,  $\text{CTF}_{\text{eye}}$  is obtained at each specific frequency and light level:

$$\text{CTF}_{\text{eye}}^2 = \kappa^2 N_{\text{eye}}^2 \quad \Rightarrow \quad \kappa^2 = \frac{\text{CTF}_{\text{eye}}^2}{N_{\text{eye}}^2}$$

$$\text{CTF}_n^2 = \kappa^2 N^2 + \text{CTF}_{\text{eye}}^2 = \text{CTF}_{\text{eye}}^2 \left( 1 + \frac{N^2}{N_{\text{eye}}^2} \right)$$

Since  $N$  and  $N_{\text{eye}}$  are both referenced to the same display luminance, the above equation can be written as

$$\text{CTF}_n^2 = \text{CTF}_{\text{eye}}^2 \left( 1 + \frac{\sigma_n^2}{\sigma_{\text{eye}}^2} \right)$$

where  $\sigma_n$  is the rms noise filtered by the display, and  $\sigma_{\text{eye}}$  is the rms visual noise expressed at the display. Both  $\sigma_n^2$  and  $\sigma_{\text{eye}}^2$  have units of  $\text{K}^2 \cdot \text{sec}$ .

$\sigma_{\text{eye}}$  is directly proportional to the average display scene contrast temperature  $\text{SCN}_{\text{tmp}}$  (i.e., Weber's law):

$$\sigma_{\text{eye}}^2 = \frac{\text{SCN}_{\text{tmp}}^2}{\alpha^2}$$

Therefore,  $\text{CTF}_n$  can be written as

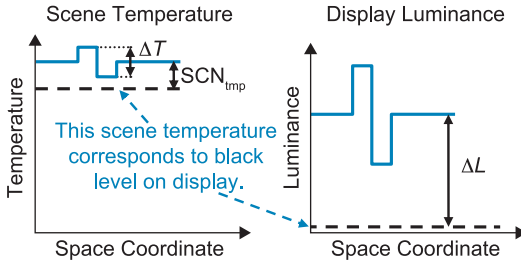
$$\text{CTF}_n = \text{CTF}_{\text{eye}} \left( 1 + \frac{\alpha^2 \sigma_n^2}{\text{SCN}_{\text{tmp}}^2} \right)^{1/2}$$

where  $\alpha = 169.6$  root-Hz is an empirically derived calibration factor relating eye noise to average scene temperature as seen on the display. This value is a constant regardless of the system or environment modeled.

The **scene contrast temperature**  $\text{SCN}_{\text{tmp}}$  [K] is the term used in thermal imagers to define the radiometric temperature in the scene needed to raise the display luminance from zero to the average displayed luminance. Zero luminance on the display corresponds to minimum visible scene radiant energy, not to zero radiant energy.

## Contrast Threshold Function (CTF) (cont.)

The value of  $SCN_{tmp}$  is determined by the settings of the sensor's gain and offset. Guidance regarding the appropriate value of this model parameter is given in the NVThermIP user's guide.



When using visible sensors, the term luminance or scene contrast illumination is used instead of radiance. In this case, the units of  $\sigma_n^2$  and  $\sigma_{eye}^2$  are footlamberts<sup>2</sup>·sec.

The  $CTF_{sys}$  of an imaging system is the naked-eye  $CTF_{eye}$  degraded by a wide variety of factors associated with the imaging system. It is important to realize that the signal is blurred by every component in the image-processing chain (optics, detector, electronics, display, and eye), while the noise is blurred by the components only subsequent to photodetection. This is because most of the system noise is introduced in the photodetector.  $CTF_{sys}$  is obtained by dividing  $CTF_n$  by the system's MTF to account for the variety of MTF losses associated with the sensor system:

$$CTF_{sys} = \frac{CTF_{eye}}{MTF_{sys}(\xi)} \left( 1 + \frac{\alpha^2 \sigma_n^2}{SCN_{tmp}^2} \right)^{1/2} = \frac{CTF_{eye}}{MTF_{sys}(\xi)} (1 + C^2)^{1/2}$$

$CTF_{sys}$  is a unitless figure-of-merit and specifies a system's performance under two main conditions:

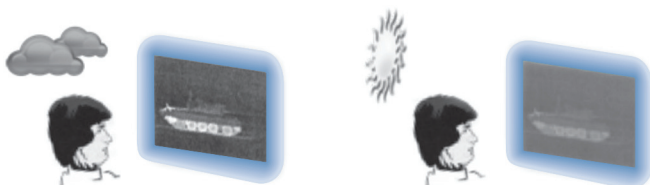
- $C^2 > 1$ : The noise is visible to the observer, such as in uncooled sensors and second-generation FLIRs.
- $C^2 < 1$ : The noise is not discernible to the observer, such as in cryogenic photon detectors operating with fast optics. In this case, the system performance is limited only by the  $CTF_{eye}$  and the image blur.

### Contrast Threshold Function (CTF) (cont.)

---

The  $CTF_{sys}$  equation is 1D. In the TTP model, imaging systems are analyzed separately in both the horizontal and vertical coordinates. Even though this approximation is seldom satisfied, the error associated with it is rather small, thus making this assumption valid in most cases.

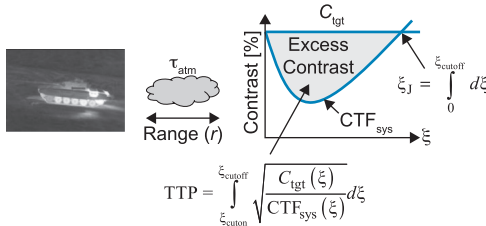
The effect of display glare affects targeting performance. For example, sunlight reflecting off of the display represents a reduction in modulation depth at all spatial frequencies, thus decreasing the system's MTF.



Electronic and digital processing can boost intermediate and high spatial frequencies, improving the displayed representation of scene detail and enhancing target acquisition performance. The sensor gain and offset are adjusted to obtain optimal acquisition performance, and these parameters determine the scene contrast temperature.

## Target Acquisition Performance

The procedure for predicting field range performance is shown below.



At the sensor, the target-to-background contrast is defined as

$$C_{tgt} = \tau_{atm} \frac{\sqrt{(\mu_{tgt} - \mu_{bkg})^2 + \sigma_{tgt}^2}}{2(SCN_{tmp})} = \tau_{atm} \frac{\Delta T_{RSS}}{2(SCN_{tmp})}$$

where  $\mu_{tgt}$  and  $\mu_{bkg}$  are the corresponding mean temperatures of the target and background, respectively,  $\sigma_{tgt}$  is the standard deviation of the target temperature, and  $\tau_{atm}$  is the atmospheric transmission. The numerator of  $C_{tgt}$  is an estimate of  $L_{v,max} - L_{v,min}$ , and  $2(SCN_{tmp})$  estimates  $L_{v,max} + L_{v,min}$  in the contrast equation.

$C_{tgt}$  establishes the signal available at each single spatial frequency, and that signal is compared to the observer's threshold at that particular frequency.  $C_{tgt}$  is measured close to the target so that sensor blur does not affect the accuracy of measuring the target variance. The model treats the "target" signal as having a uniform distribution of spatial frequencies (i.e., white noise). Remember that the model is predicting the ability to discriminate between targets, which means that all spatial frequencies are equally important in distinguishing individual targets from one another.

The Johnson methodology uses the limiting frequency  $\xi_J$  visible at the average target contrast to estimate acquisition performance. In the Johnson method,

$$\xi_J = \int_0^{\xi_{cutoff}} d\xi$$

where  $\xi_J$  is the frequency, for which  $C_{tgt} = CTF_{sys}$ .

### Target Acquisition Performance (cont.)

The TTP methodology generalizes the Johnson methodology. The TTP metric is calculated separately for both the horizontal and vertical dimensions by

$$\text{TTP}_H = \int_{\xi_{\text{cuton}}}^{\xi_{\text{cutoff}}} \sqrt{\frac{C_{\text{tgt}}}{\text{CTF}_{\text{sys}}(\xi)}} d\xi \quad \text{and}$$

$$\text{TTP}_V = \int_{\eta_{\text{cuton}}}^{\eta_{\text{cutoff}}} \sqrt{\frac{C_{\text{tgt}}}{\text{CTF}_{\text{sys}}(\eta)}} d\eta$$

where the limits of the integrals are determined by the intersection points of  $C_{\text{tgt}}$  with the  $\text{CTF}_{\text{sys}}$  curve. Here,  $\text{CTF}_{\text{sys}}(\xi)$  and  $\text{CTF}_{\text{sys}}(\eta)$  are the system contrast threshold functions in the horizontal and vertical directions, respectively. The TTP metric gives weight to the amount that the threshold is exceeded at each spatial frequency, making the TTP model sensitive to image qualities not quantified by the Johnson methodology. The geometric mean of  $\text{TTP}_H$  and  $\text{TTP}_V$  values is used to find the overall TTP value:

$$\text{TTP} = \sqrt{\text{TTP}_H \cdot \text{TTP}_V} \quad [\text{cycles/mrad}]$$

The number of cycles on target is then calculated by

$$V_{\text{resolved}} = \text{TTP} \cdot \frac{\sqrt{A_{\text{tgt}}}}{r}$$

When predicting the probability of accomplishing a task for a staring system at a certain range, sampling artifacts reduce the resolved cycles. A correction factor for the out-of-band spurious response (i.e., signal beyond the half-sampled frequency) is applied:

$$V_{\text{sampled}} = V_{\text{resolved}} \sqrt{1 - 0.58\text{SRR}_{H,\text{out}}} \sqrt{1 - 0.58\text{SRR}_{V,\text{out}}}$$

where the factor 0.58 comes from an empirical fit of perception data, and the amount of degradation or spurious response ratio (SRR) is given by

### Target Acquisition Performance (cont.)

$$\text{SRR}_{\text{H,out}} = \frac{\int_{v/2}^{\infty} \sqrt{\sum_{n \neq 0} \text{MTF}_{\text{H,pre}}^2(\xi - nv) \text{MTF}_{\text{H,post}}^2(\xi)} \cdot d\xi}{\int_0^{\infty} \text{MTF}_{\text{H,sys}}^2(\xi) \cdot d\xi}$$

$$\text{SRR}_{\text{V,out}} = \frac{\int_{\mu/2}^{\infty} \sqrt{\sum_{n \neq 0} \text{MTF}_{\text{V,pre}}^2(\eta - n\mu) \text{MTF}_{\text{V,post}}^2(\eta)} \cdot d\eta}{\int_0^{\infty} \text{MTF}_{\text{V,sys}}^2(\eta) \cdot d\eta}$$

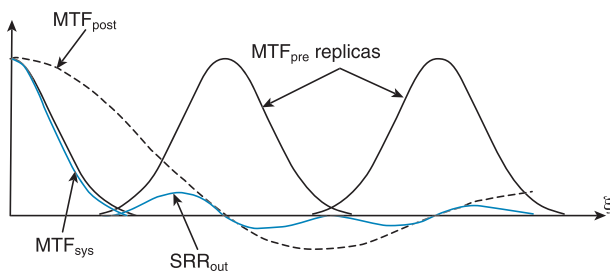
where

- $n$  is the summation index ( $\dots, -2, -1, 1, 2, \dots$ ),
- $\xi$  is the horizontal spatial frequency,
- $v$  is the horizontal sample frequency,
- $\text{MTF}_{\text{H,pre}}$  is the horizontal pre-sampled MTF (optics detector and line-of-sight jitter),
- $\text{MTF}_{\text{H,post}}$  is the horizontal post-sampled MTF (display, digital processing, and the eye-brain filter),
- $\text{MTF}_{\text{H,sys}}$  is the horizontal system MTF,
- $\eta$  is the vertical spatial frequency,
- $\mu$  is the vertical sample frequency,
- $\text{MTF}_{\text{V,pre}}$  is the vertical pre-sampled MTF,
- $\text{MTF}_{\text{V,post}}$  is the vertical post-sampled MTF,
- $\text{MTF}_{\text{V,sys}}$  is the vertical system MTF.
- Most imagers have different sampling spacings in the horizontal and vertical dimensions; for this reason,  $\text{SRR}_{\text{out}}$  is calculated in both coordinates independently.
- $\text{MTF}_{\text{pre}}$  is replicated at multiples of the sample frequency (i.e., the  $n \neq 0$  terms). The spurious response is the  $\text{MTF}_{\text{pre}}$  replicas filtered by  $\text{MTF}_{\text{post}}$ .



## Target Acquisition Performance (cont.)

A notional plot of the sampled imager response function is shown as follows:



In real imagers,  $MTF_{post}$  limits the upper frequency content visible to the observer to approximately 2.5 times the sample frequency. The replicas centered on spatial frequencies above twice the sample frequency are filtered out. In the  $MTF_{pre}$  aliased regions, the signals from different replicas are added in quadrature before integration.

## Probability of Targeting Task Performance

The probability that the observer can discriminate between targets depends on how alike the targets look. The discrimination task is quantified by specifying the number of V50 cycles in the TTP model, where V50 is the number of cycles needed for achieving a 50% probability of correct task accomplishment. The V50 values in the TTP model have the same units and are analogous to the N50 values used in the Johnson criteria, and they are determined in the field by experiment and experience. These N50 and V50 values are used to quantify task difficulty.

Johnson determined that the N50 values needed to predict the discrimination of a target with 50% probability are 1, 4, and 8 cycles for detection, recognition, and identification respectively. He used the critical dimension (minimum height- $x_{\min}$ ) of the target. However, in 1990 NVESD found that the square root of the area of the target ( $A_{\text{tgt}}^{1/2}$ ) was a better descriptor, and these standard sets of values evolved to 0.75 for detection, 3 for recognition, and 6 for identification. The reason for these modifications is that NVESD computer models predicted range performance of staring arrays (i.e., 2D systems) rather than the historical 1D first-generation FLIR systems.

An empirically derived **target transfer probability function (TTPF)** is an equation that converts the ratio of N to N50 or the ratio of V to V50 into probabilities of task performance.

TTPF<sub>J</sub> is associated with the Johnson criteria and is given by

$$\text{TTPF}_J = P = \frac{(N/N50)^{E_J}}{1 + (N/N50)^{E_J}}, \quad \text{where } E_J = 1.75 + 0.35(N/N50)$$

while TTPF<sub>TTP</sub> is associated with the TTP criteria and takes the form

$$\text{TTPF}_{\text{TTP}} = P = \frac{(V/V50)^{E_{\text{TTP}}}}{1 + (V/V50)^{E_{\text{TTP}}}},$$

where  $E_{\text{TTP}} = 1.51 + 0.24(V/V50)$

## Probability of Targeting Task Performance (cont.)

The ultimate goal of the TTP model is to predict how well an observer can discriminate targets. Measurements related to recognizing or identifying field targets are based on forced-choice experiments, typically 3 choices for recognition and 12 choices for identification. There are usually 10–20 well-trained observers, 3–4 ranges, and a good variety of targets and different aspect angles. The images of the targets are degraded by blurring, adding noise, or reducing contrast. The observers are then asked to discriminate the targets based on degraded images, and an ensemble probability as a function of measured range is obtained.

With modern staring arrays, N50 and V50 values are routinely compared, and they do not follow a particular pattern. Their ratio of cycles on target can vary as low as 0.75 and as high as 8, depending on the sampling frequency, MTF, rms noise, contrast, etc. Therefore, the best way to acquire the V50 values is directly from data field experimentation. However, when the N50 values are the only readily available data, an approximate ratio of 1:2.7 is used to relate the Johnson cycles to the TTP cycles on target. This number increases when the probability due to chance is removed. The N50 uncorrected data is rectified by the TTP model by removing the probability of chance before using experimental data to calibrate the model. The data corrected for chance is described by

$$P_{\text{corrected}} = \frac{P_{\text{measured}} - P_{\text{chance}}}{P_{\text{observer}} - P_{\text{chance}}}$$

where  $P_{\text{chance}}$  is the probability of correctly recognizing or identifying the target by chance alone, and  $P_{\text{measured}}$  is the field-measured probability as a function of range. Most of the military subjects used in these types of experiments are trained to a proficiency ( $P_{\text{observer}}$ ) between 90% and 95% probability. Experienced enlisted military subjects perform at 100% proficiency. Whether this base error rate should be included in the model is a matter of judgment. If the above formulae are followed, the TTP model accurately predicts observer performance.

### N50-to-V50 Conversion (Example)

The method for finding the equivalent V50 value from a 12-forced-choice identification experiment yielding  $N50_{ID} = 7.8$  is illustrated assuming a perfect observer (i.e.,  $P_{observer} = 1$ ).

The probability of chance is  $P_{chance} = \frac{1}{12} = 0.083$ .

This probability of chance is removed using

$$P_{corrected} = \frac{P_{measured} - P_{chance}}{1 - P_{chance}} = \frac{0.5 - 0.083}{1 - 0.083} = 0.455.$$

Using the empirical equation of the TTPF associated with the Johnson criteria,

$$0.445 = \frac{(N/7.8)^{E_J}}{1 + (N/7.8)^{E_J}}, \quad \text{where } E_J = 1.75 + 0.35(N/7.8)$$

$$\Rightarrow N = 7.15$$

The scale factor is  $\frac{7.8}{7.15} = 1.1$ , in which case,

$$V50_{ID} = 2.7 \times 1.1 \times N50_{ID} = 23.2$$

In the case of target detection, there is virtually no chance that an observer discovers a target by chance. Therefore,

$$V50_{det} = 2.7 \times N50_{det} = 2.7 \times 0.75 = 2.025$$

The conversion factors based on the number of choices in the experiment are listed in the table below. As the number of choices increases, the impact of using uncorrected data to establish N50 values decreases to one.

| Number of Choices | N50 multiplier |
|-------------------|----------------|
| 3                 | 1.79           |
| 4                 | 1.43           |
| 5                 | 1.30           |
| 6                 | 1.23           |
| 8                 | 1.16           |
| 10                | 1.12           |
| 12                | 1.10           |
| 20                | 1.05           |

## Acquisition Level Definitions

---

**Detection:** The determination that an object or location in the FOV may be of military interest such that the military observer takes an action to look closer, alters a search in progress, changes magnification, selects a different sensor, or cues a different sensor.

**Classification:** The object is discriminated by class, such as wheeled or tracked vehicles, rotary- or fixed-wing aircraft, and human being or other animal.

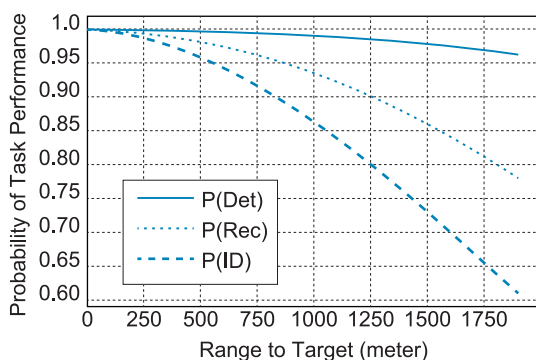
**Recognition:** 1. For vehicles and weapons platforms, the object can be distinguished by category within a class (e.g., tracked or wheeled air defenses or personnel carrier; artillery or tanks or utility vehicles; a dozer or an excavator). 2. For humans, individual elements (a combination, or a lack of, equipment, hand-held objects) and/or postures can be distinguished to the extent that the human is determined to be of special military interest (e.g., wearing head gear or carrying hand-held objects).

**Identification:** 1. For military vehicles and weapon systems, the object is discerned by model (e.g., M1A1 or T80). 2. For commercial vehicles, the object is discerned by model types (e.g., four-door utility vehicle or two-door pickup truck, a four-door sedan or a two-door coupe). 3. For humans, individual elements, such as clothing, equipment, hand-held objects, posture and/or gender can be distinguished to the extent that the human is determined to be armed or potentially combatant. Examples include rifle or shovel, uniformed infantry or non-uniformed civilian, armored head gear or construction helmet.

**Feature Identification:** 1. Commercial vehicles can be distinguished by make and model (e.g., Ford<sup>®</sup> Mustang GT or Toyota<sup>®</sup> Camry). 2. Individual elements of clothing, equipment, hand-held objects, and/or gender can be discriminated by name or country/region of origin (e.g., M16 or Kalachnikov, revolver or cell phone, facial recognition/ID).

## TTP Summary

The basics of a new target acquisition metric for predicting target performance was explained. This new computer model developed by NVESD and called “the targeting task performance (TTP) metric” addresses the shortcomings of the Johnson criteria. The TTP metric can be applied directly to sampled imagers, intensifiers, and imagers that exhibit colored noise due to frequency boost. It predicts the CTF of the system and uses this to calculate the target acquisition range performance. An example of a resultant range performance plot is illustrated below.



The NV-IPM additionally calculates the horizontal and vertical pre- and post-sample MTFs, as well as the system and turbulence MTFs. It also predicts the 2D MRTDs of the system.

There are still many remaining challenges associated with modeling and predicting target acquisition performance. A primary challenge is that, although the field performance and model predictions match well, a robust human/sensor visual acuity test for under-sampled imagers is still unavailable. Furthermore, sophisticated staring array sensors, multiband thermal imagers, and advanced signal processing driven by new applications, such as urban fighting and force protection/anti-terrorism (FP/AT), are not yet predicted by any of the current computer models.

## Equation Summary

---

### Power spectral density:

$$\text{PSD} = N(f) = \mathcal{F}\{c_n(\tau)\} = \int_{-\infty}^{\infty} c_n(\tau) e^{-j2\pi f\tau} d\tau$$

### Noise-equivalent bandwidth:

$$\text{NE}\Delta f \equiv \frac{1}{G^2(f_0)} \int_0^{\infty} |G(f)|^2 df$$

$$\text{NE}\Delta f \equiv \frac{1}{2\tau} \quad \text{square function}$$

$$\text{NE}\Delta f \equiv \frac{1}{4\tau} \quad \text{exponential function}$$

### Shot noise:

$$i_{n,\text{shot}} = \sqrt{2qi\Delta f}$$

### Generation-recombination noise:

$$i_{n,G/R} = 2qG\sqrt{\eta E_p A_d \Delta f + g_{\text{th}} \Delta f} \cong 2qG\sqrt{\eta E_p A_d \Delta f}$$

$$i_{n,G/R} = \sqrt{2}i_{n,\text{shot}}G$$

### Johnson noise:

$$v_{n,j} = \sqrt{4kTR} \quad i_{n,j} = \sqrt{\frac{4kT}{R}}$$

$$i_{n,j} = \sqrt{i_d^2 + i_L^2}$$

$$= \sqrt{4kT\Delta f \left( \frac{T_d}{R_d} + \frac{T_L}{R_L} \right)} \quad \text{for cryogenic detector conditions}$$

### 1/f noise:

$$i_{n,f} = \sqrt{\mathcal{K} \frac{i^{\alpha} \Delta f}{f^{\beta}}}$$

### Temperature noise:

$$\overline{\Delta T^2} = \frac{4kKT^2}{K^2 + (2\pi f)^2 C^2}$$

## Equation Summary

---

### Responsivity (frequency and spectral):

$$\mathcal{R} = \frac{\text{output signal}}{\text{input flux}}$$

$$|\mathcal{R}_{v,e}(f)| = \frac{\mathcal{R}_0}{\sqrt{1 + (2\pi f\tau)^2}} \quad \mathcal{R}_{v,e}(\lambda) = \mathcal{R}_{v,e}(\lambda_{\text{cutoff}}) \frac{\lambda}{\lambda_{\text{cutoff}}}$$

### Detector output voltage:

$$v_{\text{out,det}} = \int_0^{\lambda_{\text{cutoff}}} \phi_{\lambda}(\lambda) \mathcal{R}_v(\lambda) d\lambda$$

### Noise-equivalent power:

$$\text{NEP} = \frac{v_n}{\mathcal{R}_v} = \frac{v_n}{v_{\text{sig}}/\phi_{\text{sig}}} = \frac{\phi_{\text{sig}}}{\text{SNR}} \text{ [W]}$$

### Specific or normalized detectivity $D^*$ :

$$D^* = \frac{\sqrt{A_d \Delta f}}{\text{NEP}} = \frac{\sqrt{A_d \Delta f}}{\phi_d} \text{SNR} = \frac{\sqrt{A_d \Delta f}}{v_n} \mathcal{R}_v \text{ [cm}\sqrt{\text{Hz}}/\text{W]}$$

### Double-D star $D^{**}$ :

$$D^{**} = \sin \theta \cdot D^*$$

### Photodiodes under BLIP conditions:

$$\text{SNR}_{\text{PV}} = \frac{\phi_{e,\text{sig}} \eta q \frac{\lambda}{hc}}{\sqrt{2q^2 \phi_{e,\text{bkg}} \eta \frac{\lambda}{hc} \Delta f}}$$

$$\text{NEP}_{\text{PV,BLIP}}(\lambda) = \sqrt{\frac{hc}{\lambda} \frac{2\phi_{e,\text{bkg}} \Delta f}{\eta}}$$

$$\begin{aligned} D_{\text{PV,BLIP}}^*(\lambda_{\text{cutoff}}) \frac{\lambda_{\text{cutoff}}}{hc} &= \sqrt{\frac{\eta}{2 \int_{\lambda_{\text{cutoff}}}^{\lambda_{\text{cutoff}}} E_{p,\text{bkg}}(\lambda) d\lambda}} \\ &= (F/\#) \frac{\lambda_{\text{cutoff}}}{hc} \sqrt{\frac{\eta}{\pi \int_{\lambda_{\text{cutoff}}}^{\lambda_{\text{cutoff}}} L_{p,\text{bkg}}(\lambda) d\lambda}} \end{aligned}$$



## Equation Summary

### Photodiodes under JOLI conditions:

$$\text{SNR}_{\text{PV,JOLI}} = \frac{q\eta\phi_{\text{e,sig}} \frac{\lambda}{hc}}{4k\Delta f \left( \frac{T_d}{R_d} + \frac{T_L}{R_L} \right)} \cong \frac{q\eta\phi_{\text{e,sig}} \frac{\lambda}{hc}}{4k\Delta f \frac{T_d}{R_d}} \quad R_L \gg R_d$$

$$D_{\text{PV,JOLI}}^* \frac{\lambda q \eta}{2hc} = \sqrt{\frac{R_d A_d}{k T_d}}$$

### Photoconductive detectors under BLIP conditions:

$$\text{NEP}_{\text{PC,BLIP}} = \frac{2hc}{\lambda G} \sqrt{\frac{E_{\text{p,bkg}} A_d \Delta f}{\eta}} \quad D_{\text{PC,BLIP}}^* = \frac{\lambda}{2hc} G \sqrt{\frac{\eta}{E_{\text{p,bkg}}}}$$

### Photoconductive detectors under JOLI conditions:

$$\text{NEP}_{\text{PC,JOLI}} \equiv \frac{i_j}{\mathcal{R}_{\text{i,PC}}} = \frac{\sqrt{4k\Delta f T / R_{\text{eq}}}}{\frac{\lambda q \eta}{hc} G}$$

### Indium antimonite detectors:

$$\mathcal{E}_{\text{gap}}(x) = 0.233 - (6.498 \times 10^{-5})T - (5.0826 \times 10^{-7})T^2$$

$$i = i_0 [\exp(qv/kT) - 1] - i_{\text{ph}} + \frac{v}{R_s}$$

### Mercury cadmium telluride detectors:

$$\mathcal{E}_{\text{gap}}(x) = -0.302 + 1.93x + (5.35 \times 10^{-4})T(1 - 2x) - 0.801x^2 + 0.832x^3$$

$$\lambda_c = \frac{1}{-0.2435 + 1.5565x + (4.3145 \times 10^{-4})T(1 - 2x) - 0.646x^2 + 0.671x^3}$$

$$\frac{\partial \lambda_c}{\lambda_c^2} = [1.5565 - (8.629 \times 10^{-4})T - 1.292x + 2.013x^2] \partial x$$

## Equation Summary

---

### Quantum Well Infrared Photodetectors (QWIPs)

de Broglie wavelength:

$$\Lambda = \frac{h}{2\pi p}$$

Schrödinger equation:

$$-\frac{\hbar^2}{8\pi^2 m_e^*} \cdot \frac{d^2\psi}{dx^2} = \mathcal{E}\psi$$

Eigenfunctions:

$$\psi_i = \sqrt{\frac{2}{l_w}} \sin\left(\frac{\pi x}{l_w} i\right)$$

Discrete energy levels:

$$\mathcal{E}_i = \frac{\hbar^2}{8m_e^* l_w^2} i^2$$

Intersubband transition:

$$\Delta\mathcal{E} = \mathcal{E}_2 - \mathcal{E}_1 = \frac{3\hbar^2}{8m_e^* l_w^2}$$

### Pyroelectric detectors:

$$\mathcal{R}_i = \frac{i}{\phi_{e,o}} = \frac{\rho\omega\epsilon R_{th}A_d}{\sqrt{1 + (\omega\tau_{th})^2}}$$

$$\mathcal{R}_v = \frac{\rho\omega\epsilon R_{th}RA_d}{\sqrt{1 + (\omega\tau_{th})^2} \sqrt{1 + (\omega\tau_{RC})^2}}$$

$$D^* = \frac{\mathcal{R}_v \sqrt{A_d \Delta f}}{v_j} = \frac{\rho\omega\epsilon (R_{th}A_d) \sqrt{RA_d}}{\sqrt{4kT} \sqrt{1 + (\omega\tau_{th})^2} \sqrt{1 + (\omega\tau_{RC})^2}}$$

## Equation Summary

---

### Microbolometers:

$$\mathcal{R}_v = \frac{\alpha \varepsilon v_{\text{bias}}}{4K \sqrt{1 + \omega^2 \tau_{\text{th}}^2 - 2\varepsilon \phi_{\text{e,o}}}}$$

$$D_{\text{TF}}^* = \sqrt{\frac{\varepsilon A_{\text{d}}}{4kKT_{\text{d}}^2}} \text{ temperature fluctuation}$$

$$D_{\text{BF}}^* = \sqrt{\frac{\varepsilon}{8k\sigma(T_{\text{d}}^5 + T_{\text{bkg}}^5)}} \text{ background fluctuation}$$

### Thermoelectric detectors:

$$\mathcal{R}_v = \frac{\varepsilon \Theta N}{K \sqrt{1 + \omega^2 \tau_{\text{th}}^2}}$$

### Signal-to-noise ratio in scanning and staring systems:

$$\text{SNR} \propto \sqrt{\text{number of sensor elements}} = \sqrt{n_{\text{d}}}$$

### Range equation:

$$r = \sqrt{\frac{\pi D_{\text{opt}} \tau_{\text{opt}}}{4(F/\#)}} \sqrt{I \tau_{\text{atm}}} \sqrt{D^*} \sqrt{\frac{1}{\text{SNR} \sqrt{\Omega_{\text{d}} \Delta f}}}$$

$$r_{\text{BLIP}} = \sqrt{\frac{\pi D_{\text{opt}} \tau_{\text{opt}}}{4}} \sqrt{\tau_{\text{atm}} I} \sqrt{\frac{\lambda_{\text{cutoff}}}{hc}} \sqrt[4]{\frac{2\eta}{\pi \int_{\lambda_{\text{cutoff}}}^{\lambda_{\text{cutoff}}} L_{\text{p,bkg}} d\lambda}} \sqrt{\frac{1}{\text{SNR} \sqrt{\Delta f} \sqrt{\Omega_{\text{d}}}}}$$

### Noise-equivalent irradiance:

$$\text{NEI} = \frac{4(F/\#) \sqrt{\Omega_{\text{d}} \Delta f}}{\pi D_{\text{opt}} D^* \tau_{\text{opt}} \tau_{\text{atm}}}$$

$$\text{NEI}_{\text{BLIP}} = \frac{2hc}{\lambda_{\text{cutoff}} D_{\text{opt}} \tau_{\text{opt}} \tau_{\text{atm}}} \sqrt{\frac{2\Omega_{\text{d}} \Delta f \int_{\lambda_{\text{cutoff}}}^{\lambda_{\text{cutoff}}} L_{\text{p,bkg}} d\lambda}{\pi \eta}}$$

### Modulation depth:

$$M = \frac{A_{\text{max}} - A_{\text{min}}}{A_{\text{max}} + A_{\text{min}}}$$

## Equation Summary

---

### Modulation transfer function (MTF) definition:

$$\text{MTF}(\xi, \eta) = \frac{M_{\text{img}}(\xi, \eta)}{M_{\text{obj}}(\xi, \eta)}$$

### Strehl ratio:

$$\text{SR} = \frac{\iint \text{MTF}_{\text{actual}}(\xi, \eta) d\xi d\eta}{\iint \text{MTF}_{\text{diff-limited}}(\xi, \eta) d\xi d\eta}$$

### Detector MTF – calculation:

$$\text{MTF}_d(\xi, \eta) = \text{sinc}(d_h \xi) \text{sinc}(d_v \eta)$$

### Optics MTF – calculations:

Square exit pupils:

$$\text{MTF}(\xi) = 1 - \frac{\xi}{\xi_{\text{cutoff}}}$$

Circular exit pupils:

$$\text{MTF}(\xi) = \frac{2}{\pi} \begin{cases} \left\{ \cos^{-1}(\xi/\xi_{\text{cutoff}}) - \xi/\xi_{\text{cutoff}} \left[ 1 - (\xi/\xi_{\text{cutoff}})^2 \right]^{1/2} \right\} & \text{for } \xi \leq \xi_{\text{cutoff}} \\ 0 & \text{otherwise} \end{cases}$$

### Motion MTF

Linear:

$$\text{MTF}_{\text{linear}}(\xi) = |\text{sinc}(d\xi)|$$

Sinusoidal:

$$\text{MTF}_{\text{sin}}(\xi) = |J_0(2\pi A\xi)|$$

Random:

$$\text{MTF}_{\text{random}}(\xi) = |e^{-2(\pi\sigma_a\xi)^2}|$$

## Equation Summary

---

### Atmospheric MTF

Fried coherence length:

$$r_0 = \left\{ 0.423 \cdot k^2 \sec(\Theta) \int_0^L C_n^2(z) dz \right\}^{-3/5}$$

Turbulence MTF:

$$\text{MTF}_{\text{tur}}(\xi) = e^{-3.44(\lambda\xi/r_0)^{5/3}}$$

Aerosol MTF:

$$\text{MTF}_{\text{aer}}(\xi) = e^{-L[\sigma(\lambda\xi/a)^2]} \quad \text{for } \xi < a/\lambda$$

$$\text{MTF}_{\text{aer}}(\xi) = e^{-L(k\sigma)} \quad \text{for } \xi > a/\lambda$$

### MTF Measurement Techniques

Point spread function response:

$$\text{MTF}(\xi, \eta) = |\mathcal{F}\{\text{PSF}\}|$$

Line spread function response:

$$\text{MTF}(\xi, \eta) = |\mathcal{F}\{\text{LSF}\}|$$

Edge spread function response:

$$\text{MTF}(\xi, \eta) = \left| \mathcal{F} \left\{ \frac{d(\text{ESF})}{dx} \right\} \right| = |\mathcal{F}\{\text{LSF}\}|$$

Bar target response:

$$\text{CTF}(\xi_f) = \frac{M_{\text{square-response}}(\xi_f)}{M_{\text{input-square-wave}}(\xi_f)}$$

$$\text{CTF}(\xi_f) = \frac{4}{\pi} \left[ \text{MTF}(\xi_f) - \frac{1}{3} \text{MTF}(3\xi_f) + \frac{1}{5} \text{MTF}(5\xi_f) - \frac{1}{7} \text{MTF}(7\xi_f) + \dots \right]$$

$$\text{MTF}(\xi_f) = \frac{4}{\pi} \left[ \text{CTF}(\xi_f) + \frac{1}{3} \text{CTF}(3\xi_f) - \frac{1}{5} \text{CTF}(5\xi_f) + \frac{1}{7} \text{CTF}(7\xi_f) - \dots \right]$$

## Equation Summary

---

Random noise target response:

$$\text{MTF}(\xi) = \sqrt{\frac{\text{PSD}_{\text{output}}(\xi)}{\text{PSD}_{\text{input}}(\xi)}}$$

**Noise-equivalent temperature difference (NETD):**

$$\text{NETD} = \frac{[4(F/\#)^2 + 1]\sqrt{\Delta f}}{\pi\tau_{\text{atm}}\tau_{\text{opt}}D^*\sqrt{A_d}(\partial L/\partial T)}$$

$$\text{NETD}_{\text{BLIP}} = \frac{2\sqrt{2}}{\pi\tau_{\text{atm}}\tau_{\text{opt}}} \frac{hc}{\lambda_{\text{cutoff}}} \frac{F/\#}{(\partial L/\partial T)} \sqrt{\frac{\Delta f \int_{\lambda_{\text{cutoff}}}^{\lambda_{\text{cutoff}}} L_{\text{p, bkg}} d\lambda}{\eta A_d}}$$

**NETD of microbolometers:**

$$\text{NETD}_{\text{TF}} = \frac{2T_d[4(F/\#)^2 + 1]\sqrt{kK\Delta f}}{\pi\tau_{\text{atm}}\tau_{\text{opt}}\varepsilon A_d(\partial L/\partial T)}$$

$$\text{NETD}_{\text{BF}} = \frac{[4(F/\#)^2 + 1]\sqrt{8kK\Delta f(T_d^5 + T_{\text{bkg}}^5)}}{\pi\tau_{\text{atm}}\tau_{\text{opt}}\sqrt{\varepsilon A_d}(\partial L/\partial T)}$$

**Minimum resolvable temperature difference (MRTD):**

$$\text{MRTD} \propto \frac{\xi_t \sqrt{\text{HIFOV} \cdot \text{VIFOV}}}{\text{MTF}(\xi_t) \sqrt{\tau_{\text{eye}} \cdot \tau_{\text{frame}}}} \times \frac{(F/\#)^2 \sqrt{\Delta f}}{D^* \sqrt{A_d} \partial L/\partial T}$$

**MRTD measurement – automatic test:**

$$\text{MRTD} = \mathcal{K}(\xi_t) \frac{\text{NETD}}{\text{MTF}(\xi_t)}$$

**Johnson Criteria**

Number of Johnson cycles on target:

$$N_{\text{resolved}} = \frac{f \cdot x_{\text{min}}}{2r\sqrt{A_d}}$$

## Equation Summary

---

Limiting frequency visible at the average target contrast:

$$\xi_J = \int_0^{\xi_{\text{cutoff}}} d\xi$$

Johnson target transfer probability function (TTPF<sub>J</sub>):

$$\text{TTPF}_J = P = \frac{(N/N50)^{E_J}}{1 + (N/N50)^{E_J}} \text{ where } E_J = 1.75 + 0.35(N/N50)$$

**Contrast:**

$$\text{Contrast} = \frac{L_{v,\text{max}} - L_{v,\text{min}}}{L_{v,\text{max}} + L_{v,\text{min}}}$$

Contrast threshold function (CTF):

$$\text{CTF}_{\text{sys}} = \frac{\text{CTF}_{\text{eye}}}{\text{MTF}_{\text{sys}}(\xi)} \left( 1 + \frac{\alpha^2 \sigma_n^2}{\text{SCN}_{\text{tmp}}^2} \right)^{1/2}$$

Target-to-background contrast:

$$\text{CTF}_{\text{tgt}} = \tau_{\text{atm}} \frac{\sqrt{(\mu_{\text{tgt}} - \mu_{\text{bkg}})^2 + \sigma_{\text{tgt}}^2}}{2(\text{SCN}_{\text{tmp}})} = \tau_{\text{atm}} \frac{\Delta T_{\text{RSS}}}{\text{SCN}_{\text{tmp}}^2}$$

## Targeting Task Performance (TTP) Metric Model

TTP target acquisition performance:

$$\text{TTP}_H = \int_{\xi_{\text{cuton}}}^{\xi_{\text{cutoff}}} \sqrt{\frac{C_{\text{tgt}}}{\text{CTF}_{\text{sys}}(\xi)}} d\xi \text{ and } \text{TTP}_V = \int_{\xi_{\text{cuton}}}^{\xi_{\text{cutoff}}} \sqrt{\frac{C_{\text{tgt}}}{\text{CTF}_{\text{sys}}(\eta)}} d\eta$$

$$\text{TTP} = \sqrt{\text{TTP}_H \cdot \text{TTP}_V} \quad [\text{cycles/mrad}]$$

Number of cycles on target:

$$V_{\text{resolved}} = \text{TTP} \cdot \frac{\sqrt{A_{\text{tgt}}}}{r}$$

## Equation Summary

---

Number of cycles on target corrected for sampling:

$$V_{\text{sampled}} = V_{\text{resolved}} \sqrt{1 - 0.58\text{SRR}_{\text{H,out}}} \sqrt{1 - 0.58\text{SRR}_{\text{V,out}}}$$

Amount of degradation or spurious response ratio (SRR):

$$\text{SRR}_{\text{H,out}} = \frac{\int_{v/2}^{\infty} \sqrt{\sum_{n \neq 0} \text{MTF}_{\text{H,pre}}^2(\xi - nv) \text{MTF}_{\text{H,post}}^2(\xi)} \cdot d\xi}{\int_0^{\infty} \text{MTF}_{\text{H,post}}^2(\xi) \cdot d\xi}$$

$$\text{SRR}_{\text{V,out}} = \frac{\int_{\mu/2}^{\infty} \sqrt{\sum_{n \neq 0} \text{MTF}_{\text{V,pre}}^2(\eta - n\mu) \text{MTF}_{\text{V,post}}^2(\eta)} \cdot d\eta}{\int_0^{\infty} \text{MTF}_{\text{V,sys}}^2(\eta) \cdot d\eta}$$

TTP target transfer probability function:

$$\text{TTPF}_{\text{TTP}} = P = \frac{(V/V50)^{E_{\text{TTP}}}}{1 + (V/V50)^{E_{\text{TTP}}}} \quad \text{where } E_{\text{TTP}} = 1.51 + 0.24(V/V50)$$



## Bibliography

---

Bass, M., *Handbook of Optics*, Vols. I & II, McGraw-Hill, New York (1995).

Beck, J., C. Wan, M. Kinch, J. Robinson, P. Mitra, R. Critchfield, F. Ma, and J. Campbell, "The HgCdTe electron avalanche photodiode," *J. Electronic Materials*, **35**(6), 1166–1173 (2006).

Boreman, G. D., *Fundamentals of Electro-Optics for Electrical Engineers*, SPIE Press, Bellingham, WA (1998) [doi: 10.1117/3.294180].

Boreman, G. D., *Modulation Transfer Function in Optical and Electro-Optical Systems*, SPIE Press, Bellingham, WA (2001) [doi: 10.1117/3.419857].

Boreman, G. D. and A. Daniels, "Use of spatial noise targets in image quality assessment," *Proc. International Congress of Photographic Science*, 448–451 (1994).

Boreman, G. D., Y. Sun, and A. B. James, "Generation of laser speckle with an integrating sphere," *Opt. Eng.* **29**(4), 339–342 (1990) [doi: 10.1117/12.55601].

Born, M. and E. Wolf, *Principles of Optics*, Pergamon Press, New York (1986).

Boyd, R. W., *Radiometry and the Detection of Optical Radiation*, Wiley, New York (1983).

Caulfield, J., J. Curzan, J. Lewis, and N. Dhar, "Small pixel oversampled IR focal plane arrays," *Proc. SPIE* **9451**, 94512F (2015) [doi: 10.1117/12.2180385].

Daniels, A., *Encyclopedia of Optical Engineering*, Marcel Dekker, New York (2003).

Daniels, A., *Field Guide to Infrared Systems, Detectors, and FPAs*, Second Edition, SPIE Press, Bellingham, WA (2010) [doi: 10.1117/3.853623].

Daniels, A., *Nondestructive Testing Handbook*, ASNT, Columbus, OH (2001).

## Bibliography

---

Daniels, A. and G. D. Boreman, "Diffraction effects of infrared halftone transparencies," *Infrared Phys. Technol.* **36**(2), 623–637 (1995).

Daniels, A., G. D. Boreman, A. D. Ducharme, and E. Sapir, "Random transparency targets for MTF measurements in the visible and infrared," *Opt. Eng.* **34**(3), 860–868 (1995) [doi: 10.1117/12.190433].

Dereniak, E. L. and G. D. Boreman, *Infrared Detectors and Systems*, John Wiley & Sons, New York (1996).

Dhar, N. K. and R. Dat, "Advanced imaging research and development at DARPA," *Proc. SPIE* **8353**, 835302 (2012) [doi: 10.1117/12.923682].

Dhar, N. K., R. Dat, and A. K. Sood, "Advances in Infrared Detector Array Technology," Chapter 7 in *Optoelectronics: Advanced Materials and Devices*, S. Pyshkin, Ed., InTechOpen Ltd., London (2013).

Driggers, R. G., E. L. Jacobs, R. H. Vollmerhausen, B. O'Kane, M. Self, S. Moyer, J. G. Hixon, G. Page, K. Krapels, and D. Dixon, "Current infrared target acquisition approach for military sensor design and wargaming," *Proc. SPIE* **6207**, 620709 (2006) [doi: 10.1117/12.660963].

Driggers, R. G., R. H. Vollmerhausen, J. P. Reynolds, J. D. Fanning, and G. C. Holst, "Infrared detector size: How low should you go?" *Opt. Eng.* **51**(6), 063202 (2012) [doi: 10.1117/1.OE.51.6.063202].

Driggers, R. G., C. M. Webb, S. J. Pruchnic, C. E. Halford, and E. Burroughs, "Laboratory measurement of sampled infrared imaging system performance," *Opt. Eng.* **38**(5), 602249 (1999) [doi: 10.1117/1.602249].

Ducharme, A. D. and G. D. Boreman, "Holographic elements for modulation transfer function testing of detector arrays," *Opt. Eng.* **34**(8), 2455–2458 (1995) [doi: 10.1117/12.207144].

## Bibliography

---

Fiete, R. D., "Image quality and  $\lambda$ FN/p for remote sensing systems," *Opt. Eng.* **38**(7), 1229–1240 (1999) [doi: 10.1117/1.602169].

Friedman, M. H., D. M. Tomkinson, L. B. Scott, B. L. O'Kane, and J. A. D'Agostino, "Standard night vision thermal modeling parameters," *Proc SPIE* **1689**, 204–212 (1992) [doi: 10.1117/12.137951].

Gaskill, J. D., *Linear Systems, Fourier Transforms, and Optics*, Wiley, New York (1978).

Goodman, J. W., *Introduction to Fourier Optics*, McGraw-Hill, New York (1968).

Greivenkamp, J. E., *Field Guide to Geometrical Optics*, SPIE Press, Bellingham, WA (2004) [doi: 10.1117/3.547461].

Guellec, F., M. Tchagaspanian, E. de Borniol, P. Castelein, A. Perez, and J. Rothman, "Advanced pixel design for infrared 3D LADAR imaging," *Proc. SPIE* **6940**, 69402M (2008) [doi: 10.1117/12.779284].

Gunning, W., "Adaptive focal plane array: a compact spectral imaging sensor," Teledyne Technologies Co. presentation at DARPA's Microsystem Technology Symposium, San Jose, Mar. 5–7, 2007, <http://www.dtic.mil/dtic/tr/fulltext/u2/a503724.pdf>.

Gunning, W. J., J. DeNatale, P. Stupar, R. Borwick, R. Dannenberg, R. Sczupak, and P. O. Pettersson, "Adaptive focal plane array: an example of MEMS, photonics, and electronics integration," *Proc. SPIE* **5783**, 366–375 (2005) [doi: 10.1117/12.606983].

Gunning, W. J., J. DeNatale, P. Stupar, R. Borwick, S. Lauxterman, P. Kobrin, and J. Auyeung, "Dual band adaptive focal plane array: an example of the challenge and potential of intelligent integrated microsystems," *Proc. SPIE* **6232**, 62320F (2006) [doi: 10.1117/12.669724].

Hecht, E. and A. Zajac, *Optics*, Addison-Wesley, Boston (1974).

## Bibliography

---

Hixson, J. G., E. Jacobs, and R. H. Vollmerhausen, "Target detection cycle criteria when using the targeting task performance metric," *Proc. SPIE* **5612**, 275–283 (2004) [doi: 10.1117/12.577830].

Holst, G. C., *Common Sense Approach to Thermal Imaging Systems*, JCD Publishing, Winter Park, FL and SPIE Press, Bellingham, WA (2000).

Holst, G. C., "Imaging system performance based upon F<sub>W</sub>/d," *Opt. Eng.* **46**(10), 103204 (2007) [doi: 10.1117/1.2790066].

Holst, G. C., *Testing and Evaluation of Infrared Imaging Systems*, Third Edition, JCD Publishing, Winter Park, FL and SPIE Press, Bellingham, WA (1993).

Holst, G. C. and R. G. Driggers, "Small detectors in infrared system design," *Opt. Eng.* **51**(9), 096401 (2012) [doi: 10.1117/1.OE.51.9.096401].

Hudson, R. D., *Infrared System Engineering*, Wiley, New York (1969).

Jenkins, F. A. and H. E. White, *Fundamentals of Optics*, McGraw-Hill, New York (1981).

Keyes, R. J., *Optical and Infrared Detectors, Topics in Applied Physics* **19**, Springer-Verlag, New York (1980).

Kingston, R. H., *Detection of Optical and Infrared Radiation*, Springer-Verlag, New York (1979).

Klipstein, P., "XB<sub>n</sub> barrier photodetectors for high sensitivity and high operating temperature infrared sensors," *Proc. SPIE* **6940**, 69402U (2008) [doi: 10.1117/12.778848].

Lane, R. and J. Health, "Innovations in IR scene simulators design," *Proc. SPIE* **3368**, 78–87 (1998) [doi: 10.1117/12.316358].

Lilley, S. J., J. N. Vizgaitis, J. Everett, and R. Spinazzola, "Multifield of view see-spot optics," *Opt. Eng.* **52**(6) 061303, (2013) [doi: 10.1117/1.OE.52.6.061303].

## Bibliography

---

Lloyd, J. M., *Thermal Imaging Systems*, Plenum, New York (1975).

Logeeswaran, V. J., J. Oh, A. P. Nayak, A. M. Katzenmeyer, K. H. Gilchrist, S. Grego, N. P. Kobayashi, S. Y. Wang, A. A. Talin, N. K. Dhar, and M. Saif Islam, "A perspective on nanowire photodetectors: current status, future challenges, and opportunities," *IEEE Journal of Selected Topics in Quantum Electronics*, **17**(4), 1102–1032 (2011).

Lohrmann, D., R. T. Littleton, C. E. Reese, D. Murphy, and J. N. Vizgaitis, "Uncooled long-wave infrared small pixel focal plane array and system challenges," *Opt. Eng.* **52**(6), 061305 (2013) [doi: 10.1117/1.OE.52.6.061305].

Martiniuk, P., M. Kopytko, and A. Rogalski, "Barrier infrared detectors," *Opto-Electronics Review* **22**(2), 127–146 (2014).

Martiniuk, P., J. Wrobel, E. Plis, P. Madejczyk, W. Gawron, A. Kowalewski, S. Krishna, and A. Rogalski, "Modeling of midwavelength infrared InAs/GaSb type II superlattice detectors," *Opt. Eng.* **52**(6), 061307 (2013) [doi: 10.1117/1.OE.52.6.061307].

Meyers, S. A., A. Khoshakhagh, J. Mailfert, P. Wanninkhof, E. Plis, M. N. Kutty, H. S. Kim, N. Gautam, B. Klein, E. P. G. Smith, and S. Krishna, "Performance of InAsSb-based infrared detectors with nBn design," *Proc. SPIE* **7808**, 780805 (2010) [doi: 10.1117/12.862295].

Nagaraja, N. S., "Effect of luminance noise on contrast thresholds," *J. Opt. Soc. Am.* **54**(7), 950–955 (1964).

Nugent, P. W., J. A. Shaw, and N. J. Pust, "Correcting for focal-plane-array temperature dependence in microbolometer infrared cameras lacking thermal stabilization," *Opt. Eng.* **52**(6), 061304 (2013) [doi: 10.1117/1.OE.52.6.061304].

## Bibliography

---

NVESD, *Night Vision Thermal and Image Processing Model User Manual* (Rev. 9) (2006).

O'Shea, P. and S. Sousk, "Practical issues with 3D noise measurements and applications to modern infrared sensors," *Proc. SPIE* **5784**, 262–271 (2005) [doi: 10.1117/12.604588].

Park, S. K., R. Schwengerdt, and M. Kaczynski, "MTF for sampled imaging systems," *Applied Optics* **23**, 2572–2582 (1984).

Perrais, G., J. Rothman, G. Destefanis, and J. Chamonal, "Impulse response time measurements in  $\text{Hg}_{0.7}\text{Cd}_{0.3}\text{Te}$  MWIR avalanche photodiodes," *J. Electronic Materials*, **37**(9), 1261–1273 (2008).

Raghavan, M., "Sources of Visual Noise," Ph.D. Dissertation, Syracuse Univ., Syracuse, New York, 1989.

Reinchenbach, S. E., S. K. Park, and R. Narayanswamy, "Characterizing digital image acquisition devices," *Opt. Eng.* **30**(2), 170–177 (1991) [doi: 10.1117/12.55783].

Rogalski, A., *Selected Papers on Infrared Detectors: Developments*, SPIE Press, Bellingham, WA (2004).

Rothman, J., G. Perrais, E. de Borniol, P. Castelein, N. Baier, F. Guellec, M. Tchagaspanian, P. Ballet, L. Mollard, and S. Gout, "HgCdTe APD: Focal plane array development at CEA Leti-Minatec," *Proc. SPIE* **6940**, 69402N (2008) [doi: 10.1117/12.780447].

Schneider, H. and H. C. Liu, *Quantum Well Infrared Photo-detectors*, Springer, New York (2007).

Sensiper, M., G. D. Boreman, and A. D. Ducharme, "MTF testing of detector arrays using narrow-band laser speckle," *Opt. Eng.* **32**(2), 395–400 (1993).

Smith, W. J., *Modern Optical Engineering*, McGraw-Hill, New York (2000).

## Bibliography

---

Sood, A. K., E. J. Egerton, Y. R. Puri, G. Fernandes, J. Xu, A. Akturk, N. Goldsman, N. K. Dhar, M. Dubey, P. S. Wijewarnasuriya, and B. I. Lineberry, "Design and development of carbon nanotube-based microbolometer for IR imaging applications," *Proc. SPIE* **8353**, 83533A (2012) [doi: 10.1117/12.923020].

Sood, A. K., R. A. Richwine, Y. R. Puri, T. Manzur, N. K. Dhar, D. L. Polla, P. S. Wijewarnasuriya, Y. Wei, J. Zhou, C. Li, Z. L. Wang, G. Fernandes, and J. M. J. Xu, "Next generation nanostructure based EO/IR focal plane arrays for unattended ground sensor applications," *Proc. SPIE* **7693**, 76930C (2010) [doi: 10.1117/12.852192].

Sundaram, M., A. Reisinger, R. Dennis, K. Patnaude, D. Burrows, J. Bundas, K. Beech, and R. Faska, "SLS technology: the FPA perspective," *Proc. SPIE* **7660**, 76601P (2010) [doi: 10.1117/12.853662].

Sundaram, M., A. Reisinger, R. Dennis, K. Patnaude, D. Burrows, J. Bundas, K. Beech, and R. Faska, "Infrared imaging with quantum wells and strained layer superlattices," *Proc. SPIE* **8268**, 82682L (2012) [doi: 10.1117/12.913965].

Sundaram, M., A. Reisinger, R. Dennis, K. Patnaude, D. Burrows, J. Bundas, K. Beech, R. Faska, and D. Manidakos, "1024 × 1024 LWIR SLS FPAs: status and characterization," *Proc. SPIE* **8353**, 83530W (2012) [doi: 10.1117/12.923442].

Temple, D. S., E. P. Vick, M. R. Lueck, D. Malta, M. R. Skokan, C. J. Masterjohn, and M. M. Muzilla, "Enabling more capability within smaller pixels: advanced wafer-level process technologies for integration of focal plane arrays with readout electronics," *Proc. SPIE* **9100**, 91000L (2014) [doi: 10.1117/12.2054106].

Temple, D. S., E. P. Vick, D. Malta, M. R. Lueck, M. R. Skokan, C. M. Masterjohn, and M. S. Muzilla, "Advances in three-dimensional integration technologies in support of infrared focal plane arrays," *Proc. SPIE* **9370**, 93701L (2015) [doi: 10.1117/12.2082877].

## Bibliography

---

Velicu, S., C. Buurma, J. D. Bergeson, T. S. Kim, J. Kubby, and N. Gupta, "Miniaturized imaging spectrometer based on Fabry-Perot MOEMS filters and HgCdTe infrared focal plane arrays," *Proc. SPIE* **9100**, 91000F (2014) [doi: 10.1117/12.2053902].

Vizgaltis, J. N. and A. R. Hastings, "Dual-band infrared picture-in-picture systems," *Opt. Eng.* **52**(6), 061306 (2013) [doi: 10.1117/1.OE.52.6.061306].

Vollmerhausen, R. H., "Incorporating display limitations into night vision performance models," *IRIS Passive Sensors* **2**, 11–31 (1995).

Vollmerhausen, R. H., E. L. Jacobs, and R. G. Driggers, "New metric for predicting target acquisition performance," *Opt. Eng.* **43**(11), 2806–2818 (2004) [doi: 10.1117/1.1799111].

Vollmerhausen, R. H., E. L. Jacobs, J. G. Hixson, and M. Friedman, "The targeting task performance (TTP) metric," *Technical Report AMSEL-NV-TR-230* (2006).

Vollmerhausen, R. H. and R. G. Driggers, *Analysis of Sampled Imaging Systems*, SPIE Press, Bellingham, WA (2000) [doi: 10.1117/3.3553257].

Vollmerhausen, R. H., D. A. Reago, and R. G. Driggers, *Analysis and Evaluation of Sampled Imaging Systems*, SPIE Press, Bellingham, WA (2010) [doi: 10.1117/3.853462].

Wittenstain, W., J. C. Fontanella, A. R. Newbery, and J. Baars, "The definition of OTF and the measurement of aliasing for sampled imaging systems," *Optica Acta* **29**, 41–50 (1982).

Wolfe, W. L., *Introduction to Infrared Systems Design*, SPIE Press, Bellingham, WA (1996) [doi: 10.1117/3.226006].

Wolfe, W. L. and G. J. Zissis, *The Infrared Handbook*, Infrared Information Analysis (IRIA) Center, Ann Arbor, MI (1989).



## Index

---

- 1/f noise, 4, 6, 13, 22, 129
- 2D periodic gratings, 53
- 3D integration, 58
  
- $\Delta f$ , 6–7, 9, 12
  
- absorption, 26, 54, 62
- absorption coefficient, *xiv*, 36, 74
- adaptive focal plane array (AFPA), 59
- AlGaAs, 44
- alloy composition, 26, 35–36
- amorphous silicon, 66
- Arrhenius plot, 33
- atmospheric extinction coefficient, 95
- autocorrelation, 5, 87, 89, 101
  
- background-limited
  - infrared photodetector (BLIP), *x*, 10, 22–23, 25, 82–83, 102–103, 130, 131, 133
- barium strontium titanate (BST), 63
- barrier photodetectors, 32
- blackbody (BB), 17, 20, 37
- blackbody responsivity, 17–18
- blur spot, 90
- bolometer, 1, 3
- bound-to-bound (B-B), 47
- bound-to-continuum (B-C), 47
- bound-to-quasi-bound (B-QB), 48
- carbon nanotube (CNT), 74
- central-ordinate theorem, 5, 90
- charge well capacity, 28
- chemical vapor deposition (CVD), 44, 74
- classification, 127
- cold-stop efficiency, 82
- common-path
  - interferometers, 101
- cones, 113, 116
- contrast, 115–116, 137
- contrast threshold
  - function, *x*, 115–119, 121, 137
- contrast transfer function, 97–98
- converging-beam
  - scanner, 75
- cooled detectors, 27
- corrugated QWIP (CQWIP), 54
- cryogenic temperatures, 12, 22
- Curie temperature, *xiv*, 62–63
- current responsivity, *xiv*, 14, 65
  
- $D^{**}$ , *x*, 23, 130
- $D^{*}_{PV, BLIP}$ , 23, 130
- dark current, 28
- de Broglie wavelength, 45, 49, 132
- depletion region (barrier), 32
- detection, 82, 110, 124, 127

## Index

---

- detection systems, 1, 19, 80–82
- detectivity, 3
- detector MTF calculation, 91
- detector output voltage, 17, 130
- dewar, 29, 31, 37
- diameter, 81, 82, 89, 94
- diffraction, 53–54, 89, 90, 100
- diffraction-limited system, 89, 94
- diffraction-limited expressions, 90
- digitization, 95, 98
- distributed Bragg reflector (DBR), 60
- double-layer heterostructure junction (DLHJ), 38
- dwell time, *xv*, 75–76, 78–79
- dynamic scene simulator (DSS), 72
- edge spread function (ESF), 96–98, 135
- effective focal length, 81, 110
- electron-injected avalanche photodiode (EAPD), 41
- emissivity, *xv*, 57, 64, 82
- energy intersubbands, 45
- exit pupil, 134
- exitance, *xii*, 37, 102
- Fabry–Pérot filter, 59
- feature identification, 57, 127
- finesse, 60
- flux, *xvi*, 3, 10, 12, 14
- focal plane array (FPA), 1, 71, 95
- footprint, 75
- frequency range, 5
- Fried coherence length, 94
- fundamental spatial frequency, 97, 105
- generation–recombination (G/R) centers, 32
- generation–recombination (G/R) noise, 4, 6, 11, 25, 129
- go–no-go systems, 80
- Golay cells, 3,
- high-density vertically integrated photodiode (HDVIP), 40–41
- high operating temperature (HOT), 27, 34
- human vision, 112–115
- identification, 28, 57, 59, 110, 127
- image irradiance, 97
- image quality, 84–86, 90, 93
- impulse response, *xi*, 6, 8, 85–88
- index of refraction, *xiii*, 43, 66, 93–94, 122

## Index

---

- indium antimonite (InSb)
  - photodiodes, 30–31
- infrared detectors, 1
- infrared focal plane array (IRFPA), 2, 27–28, 39
- infrared imaging systems, 1, 72, 84, 91, 95–96
- instantaneous field of view (IFOV), 75–76, 110
- integrated dewar cooler assembly (IDCA), 29, 31, 34
- integration time, 6, 28
- intensity, 80, 90, 114
- irradiance, 1, 15, 19, 83
- isoplanatism, 86
  
- jitter, 93
- Johnson criteria, 111, 124, 126, 128, 136
- Johnson-limited (JOLI)
  - noise performance, 23, 25, 131
- Johnson metric, 84, 109–111
- Johnson noise, 6, 12, 22, 23, 25, 65, 129
  
- light coupler, 52
- line spread function (LSF), 96–97, 135
- linearity, 14, 86,
- liquid phase epitaxy (LPE), 41
- longwave infrared (LWIR), 18, 36, 39, 50–51, 57
  
- magnification, 57, 98, 127
- mean, 4, 9
- mean square (variance), 4
- mercury cadmium telluride (HgCdTe), 35
- mesopic light, 113
- micro-electro-mechanical system (MEMS), 59, 66
- microbolometers, 13, 29, 66–71, 103, 133, 136
- midwave infrared (MWIR), 18, 31, 33–34,
- minimum resolvable temperature difference (MRTD), 84, 105–108, 136
- modulation depth, 88, 97, 105, 119, 133
- modulation transfer function (MTF), 84–88
- molar fraction, 35, 36
- molecular beam epitaxy (MBE), 38, 44
- motion degradation, 93
- MTF measurement techniques, 96–101
- multiple quantum well (MQW), 44, 51
  
- N50 values, 110, 124–126, 137
- nBn heterostructure, 33
- nCBn (compound barrier), 34
- noise-equivalent
  - bandwidth, *xiii*, 6–8, 20, 76, 129
- noise-equivalent irradiance (NEI), 83, 133

## Index

---

- noise-equivalent power (NEP), 3, 19–20, 22–23, 130, 131
- noise-equivalent temperature difference (NETD), 27, 84, 102–104, 136
- non-uniformity correction (NUC), 28, 30
- normalized detectivity,  $x$ , 20, 65, 130
- numerical aperture (NA), 98
- Nyquist frequency, 91, 99
  
- open circuit, 21, 24, 73
- optical axis, 95
- optical path difference (OPD), 101
- optical transfer function (OTF), 87, 89–90
- optics MTF calculations, 89–90
- out-of-band spurious response, *xiv*, 121–122, 138
  
- parallel-beam scanner, 75
- parallel scanning, 75, 78–79
- phase transfer function (PTF), 87–88
- phasing effects, 95–96
- photoconductive (PC) detector, 21, 24–25
- photoconductive detector under BLIP conditions, 131
- photoconductive detector under JOLI conditions, 131
- photoconductor, 24–25
- photodiode, 21–22, 32
- photon detector, 3, 16–18
- photons, 3, 10, 16, 36
- photopic light, 113
- photovoltaic (PV) detectors, 3, 9, 13, 21–22
- Planck's constant, *xi*, 45, 102
- point source, 80, 85, 96
- point spread function (PSF), 94, 96, 101, 135
- power spectral density (PSD), 5–6, 12, 99–100, 129
- probability of targeting task performance, 124–125
- pyroelectric coefficient, *xiii*, 62
- pyroelectric detector, 3, 61–65, 132
  
- quantum well, 44
- quantum well infrared photodetector (QWIP), 44–48, 49–52, 132
  
- radiance, 84, 100, 102
- radiation detection systems, 1
- random reflectors, 52–53
- range equation, 80–82, 133

## Index

---

- read-in integrated circuit (RIIC), 72
- read-out integrated circuit (ROIC), 27–29, 58
- recognition, 110, 124, 127
- refractive index, *xiii*, 43, 66, 93–94, 122
- responsive time
  - constant, 15
- responsivity (frequency, spectral, blackbody, and *K*-factor), *xiv*, 3, 14–15, 130
- reverse bias, 21, 32, 41
- rods, 113
  
- sampling effects, 95, 107
- scanning and staring
  - systems, 1, 76, 79, 121, 133
- scene contrast temperature, *xiv*, 117, 119
- Schrödinger equation, 46, 132
- scotopic light, 113
- search systems, 80–82
- Seebeck coefficient, *xv*, 73
- semiconductors, 11, 26
- shift invariance, 86
- serial scanning, 77
- Shockley–Read–Hall (SRH), 31–33
- short circuit, 21, 51
- shot noise, 6, 9–10, 22–25, 129
- signal-to-noise ratio (SNR), 10, 12, 19–20, 80–83, 133
- size, weight, power and cost (SWaP+C), 27
- spatial frequency, 85, 87–88, 90
- spatial resolution, 29, 53, 84, 105, 109
- specific detectivity, *x*, 20–21, 65, 130
- spectral responsivity, *xiv*, 3, 16–17
- standard deviation, 4, 104, 120
- staring systems, 79, 121, 133
- Stefan–Boltzmann law, 18
- steradians, 82
- Strehl ratio (SR), 90, 134
- superconductors, 3
  
- target acquisition
  - performance, 119–123
- target transfer probability
  - function (TTPF), 124, 137, 138
- targeting task
  - performance (TTP)
    - metric, 84, 111–112, 121, 128, 134, 137
- temperature noise, 13, 129
- thermal conductivity, 29, 73
- thermal detector, 3, 13, 42, 103
- thermal imaging system (TIS), 84
- thermal noise, 12
- thermal resistance
  - coefficient (TRC), 67, 69, 71

## Index

---

- thermal sensitivity, 28, 84, 102–103, 105
- thermistor, 1, 66
- thermocouple, 1, 73
- thermoelectric detector, 73, 133
- thermopile, 1, 3, 73
- through-silicon via (TSV), 58
- time delay and integration (TDI), 77–78
- total internal reflection (TIR), 53–54
- transfer function, 14, 70, 85–87
- transport length, 47
- triple-layer
  - heterostructure
  - junction (TLHJ), 37, 39
- type II strained-layer superlattice (T2SLS), 55–56
- umbrella structure, 29, 67
- uniformity, 28
- V50 values, 124–126, 138
- vanadium oxide (VO<sub>x</sub>), 66–67
- variance (mean square), 4
- voltage responsivity, *xiv*, 14, 65, 70
- warning systems, 80
- Weber's law, 114, 117
- white noise, 5–7
- yttrium barium copper oxide, 66





**Arnold Daniels** is a senior lead engineer with extensive experience in the conceptual definition of advanced infrared (IR), optical, and electro-optical (EO) systems. His background consists of technical contributions to applications for direct energy weapon systems, infrared search & track, thermal imaging, as well as ISR systems. His other areas of technical expertise include infrared radiometry, performance specification of thermal imaging systems, thermographic nondestructive testing, stray light analysis, optical design, precision optical alignment, adaptive optics, Fourier analysis, image processing, and data acquisition systems. He received a B.S. in Electro-Mechanical Engineering from the National Autonomous University of Mexico and a B.S. in Electrical Engineering from the Israel Institute of Technology (Technion). He earned an M.S. in Electrical Engineering from the University of Tel-Aviv and received a doctoral degree in Electro-Optics from the school of Optics (CREOL) at the University of Central Florida. In 1995, he received the Rudolf Kingslake medal and prize for the most noteworthy original paper to appear in SPIE's *Journal of Optical Engineering*. He currently develops electro-optical and infrared sensor systems for aerospace and defense applications.



# Infrared Systems, Detectors, and FPAs, Third Edition

**Arnold Daniels**

This third edition of the *Field Guide to Infrared Systems, Detectors, and FPAs* is devoted to fundamental background issues for optical detection processes. It compares the characteristics of cooled and uncooled detectors with an emphasis on spectral and blackbody responsivity, detectivity, and the noise mechanisms related to optical detection. The Field Guide introduces the concepts of barrier infrared detector technologies and encompasses the capabilities and challenges of third-generation infrared focal plane arrays as well as the advantages of using dual-band technology. It combines numerous engineering disciplines necessary for the development of an infrared system. It also considers the development of search infrared systems and specifies the main descriptors used to characterize thermal imaging systems. Furthermore, this guide clarifies, identifies, and evaluates the engineering tradeoffs in the design of an infrared system. It serves as a companion to the *Field Guide to Infrared Optics, Materials, and Radiometry*.

## SPIE Field Guides

The aim of each SPIE Field Guide is to distill a major field of optical science or technology into a handy desk or briefcase reference that provides basic, essential information about optical principles, techniques, or phenomena.

Written for you—the practicing engineer or scientist—each field guide includes the key definitions, equations, illustrations, application examples, design considerations, methods, and tips that you need in the lab and in the field.

John E. Greivenkamp  
Series Editor

**SPIE.**

P.O. Box 10  
Bellingham, WA 98227-0010  
ISBN: 9781510618640  
SPIE Vol. No.: FG40

ISBN 978-1-5106-1864-0



9 781510 618640

9 0 0 0 0



[www.spie.org/press/fieldguides](http://www.spie.org/press/fieldguides)